**TRIBHUVAN UNIVERSITY**

**INSTITUTE OF ENGINEERING**

**PULCHOWK CAMPUS**

**THESIS NO : M-75-MSMDE-2021-2023**

**Design and Setup of Z-Type Schlieren Imaging System for Flow Visualization**

**BY**

**SALIM MAHARJAN**

A THESIS SUBMITTED TO THE DEPARTMENT OF MECHANICAL AND AEROSPACE ENGINEERING IN PARTIAL FULFILLMENT OF THE REQUIREMENTS FOR THE DEGREE OF MASTERS OF SCIENCE IN MECHANICAL SYSTEMS DESIGN AND ENGINEERING

DEPARTMENT OF MECHANICAL AND AEROSPACE ENGINEERING
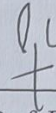
LALITPUR, NEPAL

NOVEMBER, 2023

**TRIBHUVAN UNIVERSITY**

**INSTITUTE OF ENGINEERING**

**PULCHOWK CAMPUS**

**DEPARTMENT OF MECHANICAL AND AEROSPACE ENGINEERING**
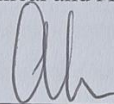
The undersigned certify that they have read, and recommended to the Institute of Engineering for acceptance, a thesis entitled "**Design and Setup of Z-type Schlieren Imaging System for Flow Visualization**" submitted by **Salim Maharjan (078/MSMDE/013)** in partial fulfillment of the requirements for the degree of Master in Mechanical Systems Design and Engineering.

_____
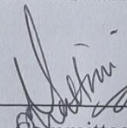
Prof. Dr. Laxman Poudel,

Supervisor,

Department of Mechanical and Aerospace Engineering

_____

Asst. Prof. Kamal Darlami,

Supervisor,

Department of Mechanical and Aerospace Engineering

_____

Dr. Abhas Maskey,

External Examiner,

Antarikchya Pratisthan Nepal (APN)

_____

Committee Chairperson,

Asst. Prof. Dr. Sudip Bhattrai,

Head of the Department,

Department of Mechanical and Aerospace Engineering

Date: 2023/11/26

iii

# ABSTRACT

Amid the research works in the field of aerodynamics and flow physics, visual experiments become a key aspect to understand the physics behind the phenomenon at work. Owing to the sensitivity of phenomenon involved in those fields, non-intrusive techniques hold greater preference over intrusive techniques. Schlieren photography is one such example of non-intrusive technique, used for the qualitative and quantitative analysis of different fluid-flow phenomena involving density gradients. In this study, a portable experimental setup of the z-type schlieren technique sitting in a bench-top of size 90 cm × 90 cm, consisting of two reflecting telescope parabolic mirrors of 76 mm diameter and 400 mm focal length is fabricated. With this setup, the qualitative and quantitative analysis of different fluid flow phenomena was performed. Negatively-Buoyant Plumes in water and Under-expanded jet from a converging-diverging nozzle are the flow-phenomena visualized. The visualized phenomena range from subsonic characteristic to supersonic characteristic. The cold dense water forming in the lower surface of the floating ice cascading into the less dense lukewarm water was considered as the experimental case for the study of Negatively-Buoyant Plumes. The z-type schlieren setup was able to capture the intricate flow structures like the formation of round topped bubbles with circular cross-section (mushroom cap shaped structure) called Rayleigh-Taylor Instability and the round topped bubbles curling back on itself called Kelvin-Helmholtz Instability. Likewise in the study of under expanded jet from a converging-diverging nozzle designed for exit Mach-number of 1.4, the regular shock-diamond structures were observed with clarity. This thesis concludes that the flow images obtained via the z-type schlieren system is good and sensitive enough to capture the flow intricacies of flow-phenomena ranging from subsonic to supersonic characteristic. Few quantitative results were also obtained for the first regular shock-diamond distance, Mach-number distribution along the under-expanded jet centerline, and simple flow deviation of the under-expanded jet from the converging-diverging nozzle.

**Keywords:** Schlieren photography, Z-type schlieren technique, Aerodynamics, Under-expanded jet, Negatively-Buoyant Plumes, Regular shock-diamond structure.

# ACKNOWLEDGEMENT

# TABLE OF CONTENTS

# LIST OF FIGURES

# LIST OF TABLES

## LIST OF SYMBOLS

$c$ :　　　　　　　speed of light in the medium *(m/s)*

$c_0$ :　　　　　　speed of light in the vacuum = *$3 \times 10^8$ m/s*

$n$ :　　　　　　　refractive index of a medium

$\rho$ :　　　　　　density of a medium *(kg/m³)*

$k$ :　　　　　　　Gladstone-Dale constant *(m³/kg)*

$M$ :　　　　　　　Mach-Number

$\varepsilon$ :　　　　　　Deflection angle *(radian)*

$f$ :　　　　　　　Focal length of the mirror *(mm)*

$\Delta f$ :　　　　　　Astigmatism severity *(mm)*

$d$ :　　　　　　　Diameter of the schlieren mirror *(mm)*

$\theta$ :　　　　　　Tilt-angle of the first or second schlieren mirror *(radian)*

$p_r$ :　　　　　　Stagnation pressure inside the reservoir *(Pascal)*

$p$ :　　　　　　　Static pressure inside the nozzle *(Pascal)*

$x$ :　　　　　　　Distance along the nozzle *(m)*

$A_t$ :　　　　　　Area of the throat of nozzle *(m²)*

$p_e$ :　　　　　　Static pressure at the exit plane of the nozzle *(Pascal)*

$A_e$ :　　　　　　Area of nozzle at the exit plane *(m²)*

$p_b$ :　　　　　　Background (back) pressure that nozzle exhausts into *(Pascal)*

$p^*$ :　　　　　　Static pressure at the nozzle throat at choked flow *(Pascal)*

$\left(\dfrac{p_b}{p_r}\right)_{NS}$ :      Back pressure to reservoir pressure ratio for Normal shock formation inside the nozzle

$\left(\dfrac{p_b}{p_r}\right)_{NSE}$ :      Back pressure to reservoir pressure ratio for Normal shock formation at the exit plane of the nozzle

$M_t$ :      Mach number at the nozzle throat

$\gamma$ :      Ratio of specific heat capacity of air at constant pressure to its specific heat capacity at constant volume = *1.4*

# LIST OF ABBREVIATIONS

CD Nozzle  =  Converging -Diverging Nozzle

CFD  =  Computational Fluid Dynamics

NPR  =  Nozzle Pressure Ratio

MOC  =  Method of Characteristic

IOE  =  Institute of Engineering

IIEC  =  Incubation, Innovation, and Entrepreneurship Center

$f$/number  =  Schlieren Mirror focal-number

CMOS  =  Complementary Metal Oxide Semiconductor

ABS  =  Acrylonitrile Butadiene Styrene

fps  =  frames per second

CAD  =  Computer Aided Design

LED  =  Light Emitting Diode

psi  =  Pound force per square inch

MP  =  Megapixel

HD  =  High Definition

# CHAPTER ONE: INTRODUCTION

This chapter establishes the work conducted for this thesis and sheds light on the statement of problem, objectives, research question, and limitations of the research study.

## 1.1 Background of Study

The innate inquisitive nature of humans has long pondered over the nature of fluid flows. The experimental and theoretical works carried out by the generation of different scientists in the quest for understanding the panoply of fluid-flow phenomena laid the early foundation of fluid-dynamic research. In many of these researches, visualization of the flow that are being studied is crucial. This is because most of the fluids present around us are transparent in nature, and this presents difficulty in predicting the nature of the fluid flow and their underlying patterns just by looking at them. There is requirement of a technique which would allow for the clear visualization of the hidden intricate patterns of the fluid-flow. These techniques form the basis of the flow visualization. There are in general three methods of flow visualization: light scattering from tracer particles, optical methods relying on refractive index changes in the fluid, and interaction processes of the fluid flow with a solid surface (Merzkirch, 2011). The optical methods do not introduce any particles/ tracers into the fluid, and is the most suited technique to study the inner intricacies of the flow field. One example of this could be the study of shock-waves. In the visualization of shock-waves, if one were to add particles/ tracers in the fluid, it might either disturb the flow or not follow the flow characteristics, resulting in a false representation of the fluid-flow.

The use of optical methods as flow visualization tool implies the strong connection between the field of optics and flow visualization. This strong connection has been mentioned by Milton Van Dyke in his seminal 1982 book (Dyke, 1982): "We who work in fluid mechanics are fortunate, as are our colleagues in a few other fields such as optics, that our subjects are easily visualized". The examples of optical methods of flow visualization includes Schlieren photography, Shadowgraphy, Moiré Deflectometry, Speckle Photography, Interferometry, etc. The late Eighties of the last century saw the advent of powerful computers and corresponding numerical calculation techniques applicable in solving fluid-flow problems. The supporters of the computational domain

went so far as to predict that the optical methods of flow visualization would be obsolete by the year 2000. Today the year 2023 is upon us and the computational development in fluid dynamic studies has taken an exponential rise. Amidst all this development, the computational advent has not removed the experimental optical flow visualization methods and those accompanying predictions have been long forgotten. In today's computational dominant era, the ever increasing new computational and numerical methods of solving the fluid-flow problems require a validation counterpart which is generally done by the experimental visualization technique like the optical flow visualization. In retrospect, there has been a symbiotic relationship between the improvement of optical flow visualization methods and development in the field of aerospace vehicles and high-speed physics. The optical flow visualization methods provide information on the nature of the fluid-flow and their underlying patterns by using the light and the changes incorporated in that light once it gets transmitted through the flow-field of interest as shown in Figure 1.1. There is a relation called the Clausius-Mosotti equation, which gives us the inter-relationship between the two parameters: refractive index $n$ and the fluid density $\rho$. For gases, this equation reduces to a simpler and elegant form shown in Eq. 1.1:

$$n - 1 = k\rho \qquad\qquad \text{Eq. 1.1}$$

where, $\rho$ is the gas density and $k$ is called the Gladstone-Dale constant which has units of $1/\rho$. The value of Gladstone-Dale constant is different for different gases, and its value is also affected by the wavelength of the light. If one were to consider the flow-visualization of a compressible ideal gas where the density of flow ($\rho$) depends on the Mach number ($M$), it would be plausible to find the Mach number or the corresponding velocity of the flow with the information gathered with the optical flow visualization techniques.
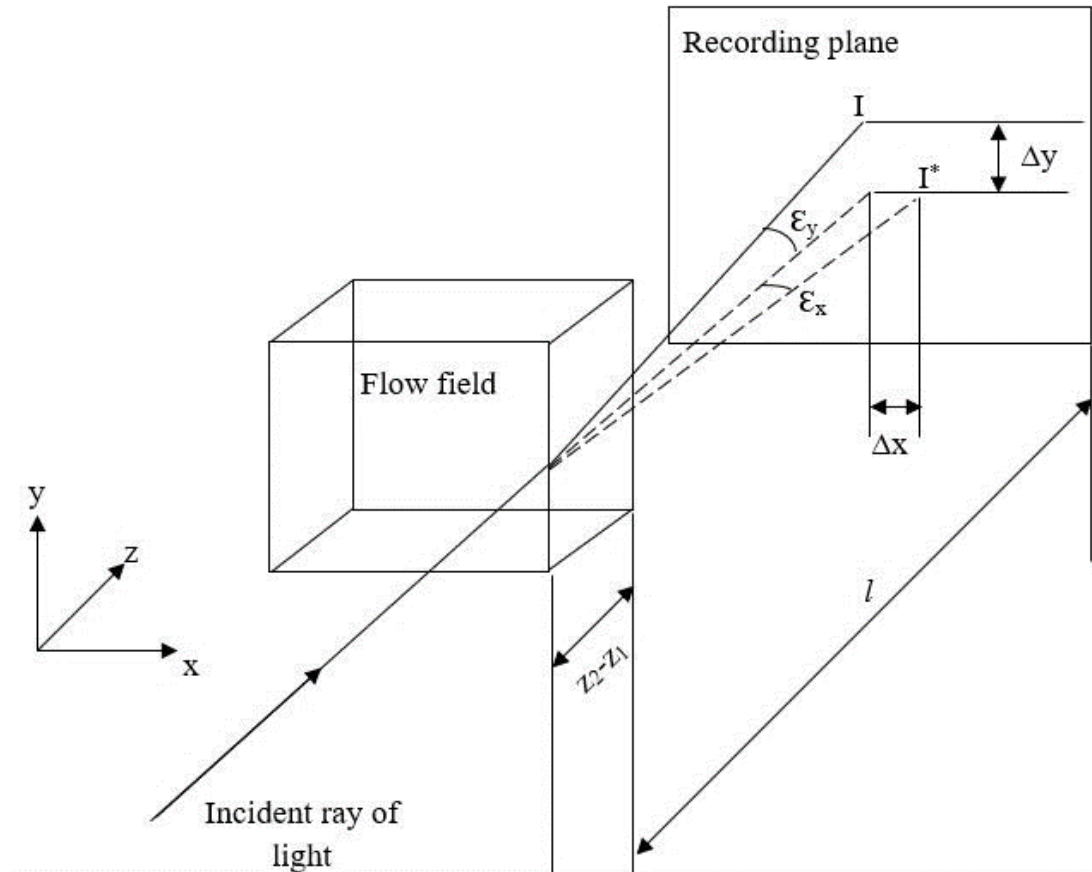
Figure 1.1: Deflection of a ray of light passing through a flow-field of varying density
(caused by refraction of light)

The propagation of a light wave or a ray of light through an inhomogeneous flow-field as shown in Figure 1.1, i.e., a region of variable fluid density, is governed by the Fermat's principle. The variation in density, and hence the refractive index (following Eq. 1.1) causes the ray of light to be deflected from its original rectilinear path. The light undergoing this deflection reaches the recording plane including the displacement with two components $\Delta x$ and $\Delta y$. The corresponding deflection angle would be $\varepsilon_x$ and $\varepsilon_y$ respectively, with z being the direction along which the incident light ray propagates. Along with the deflection of light, the optical phase of the light would also undergo change. These differences in the optical path and optical phase of light are transformed into a visible signal in the recording plane (a plane white background, photographic or electronic camera). With this analysis, one could correlate the variations in the density/ refractive index of the flow under study with the subsequent variations in the signal observed in the recording plane (Tropea, Yarin, & Foss, 2007). Depending on the nature of the signal forms such as displacement ($\Delta$), deflection angle ($\varepsilon$), and optical phase

3

difference, different optical flow visualization techniques are categorized. They are shown in Table 1.1.

Table 1.1: Methods of optical flow visualization

| Method | Signal form | Sensitive to changes of |
|---|---|---|
| Shadowgraph | Displacement, $\Delta$ | $\dfrac{\partial^2 \rho}{\partial x^2}, \dfrac{\partial^2 \rho}{\partial y^2}$ |
| Schlieren, moiré | Deflection angle, $\varepsilon$ | $\dfrac{\partial \rho}{\partial x}, \dfrac{\partial \rho}{\partial y}$ |
| Speckle photography | Deflection angle, $\varepsilon$ | $\dfrac{\partial \rho}{\partial x}, \dfrac{\partial \rho}{\partial y}$ |
| Shearing interferometry | Phase difference | $\dfrac{\partial \rho}{\partial x}, \dfrac{\partial \rho}{\partial y}$ |
| Reference beam interferometry | Phase difference | $\rho$ |

The optical flow visualization technique that is of focus in this research work is the schlieren imaging, more specifically, z-type schlieren imaging. This research is focused on the setup of z-type schlieren system, which translates phase speed differences in light which are invisible to our eyes into corresponding changes in intensity which is perceived by our eyes as regions of light and dark. The research continues with the visualization of Negatively-Buoyant Plumes and Under-expanded jet from a CD-nozzle using the fabricated schlieren setup.

**1.2 Statement of Problem**

Schlieren visualization is a time-honored technique that has been around, in its simple forms, since the $17^{th}$ century with the works of Robert Hooke and his contemporaries. While the most basic forms of schlieren imaging is not used today nor are some of the

old applications relevant nowadays, there are more advanced systems that are always been developed to match the needs/necessities of the present generation. This has resulted in new panoply of applications of schlieren imaging technique-most of which are centered around the engineering, high-speed physics, and aerospace industries with a particular focus on applications involving air and transparent media flow. This research aims at designing and setting up z-type schlieren imaging system to visualize different fluid-flow phenomena involving density gradients. This includes the visualization of thermal plume from a human hand and a burning candle and visualization of warm air near the periphery of a soldering iron rod for checking the sensitivity of the fabricated setup. It would then be followed with the qualitative and quantitative (to some extent) study of the Negatively-Buoyant Plumes in water, Under-expanded jet through a CD-nozzle (exit Mach number of 1.4) and flow deflection study for the same CD-nozzle.

## 1.3 Objectives of Research

**Main objective**

- Experimental setup of a z-type schlieren imaging system for visualization of different fluid-flow phenomena.

**Specific objectives**

- To create a portable and compact schlieren system allowing for easier fluid flow measurements and lab experimentation.
- To perform a study on the sensitivity and reliability of the schlieren images.
- To perform an experimental study on the Negatively Buoyant Plumes in water, Under-expanded jet from a converging-diverging nozzle, and flow deflection of the Under-expanded jet.

## 1.4 Research Question

The following research question would be addressed:

- Is the fabricated z-type schlieren imaging setup sensitive enough to capture intricate density-gradient details of subsonic and supersonic fluid-flow phenomena.

## 1.5 Limitations

Following were the limitations of the research study:

- The z-type schlieren system's sensitivity is limited because of the use of mirrors with $f$-number less than 6 against what is recommended in (Settles, 2001) and use of a 5-mm LED light as point source which is an incoherent light source.
- In the study of regular shock-diamond pattern from a CD-nozzle, the compressor used was able to supply a pressure up to 7.5 atm (110.22 psi). This limited the freedom of choosing the design parameter (exit Mach Number) of CD-nozzle to a value of $< 1.5$. Choice of nozzle with higher exit Mach number resulted in less sensitive schlieren images of shock-diamond structure.
- In the simulation study of under-expanded jet through a CD-nozzle, ideal gas is assumed (thermally and calorically ideal). This assumption leads to the deviation of the obtained simulation result from the experimental result.

# CHAPTER TWO: LITERATURE REVIEW

This chapter introduces the theoretical foundation of schlieren imaging with key insights on z-type schlieren system. Brief analysis on previous research works on Negatively Buoyant Plumes, Under-expanded jet from a CD-nozzle, and Fluidic-thrust vectoring using schlieren setup is also presented.

## 2.1 Schlieren Imaging

### 2.1.1 History

Schlieren techniques were first brought into public attention by Robert Hooke during the latter half of the 17$^{th}$ century. Hooke used a simple system consisting of only one lens and the iris of the spectator's eye as filter as shown in Figure 2.1. This system was developed to observe the flows of hot air in candle plumes which Hooke demonstrated to the Royal Society of London in 1672. Unfortunately, his method was not clear enough for more detailed studies, and was not reviewed for almost 200 years.
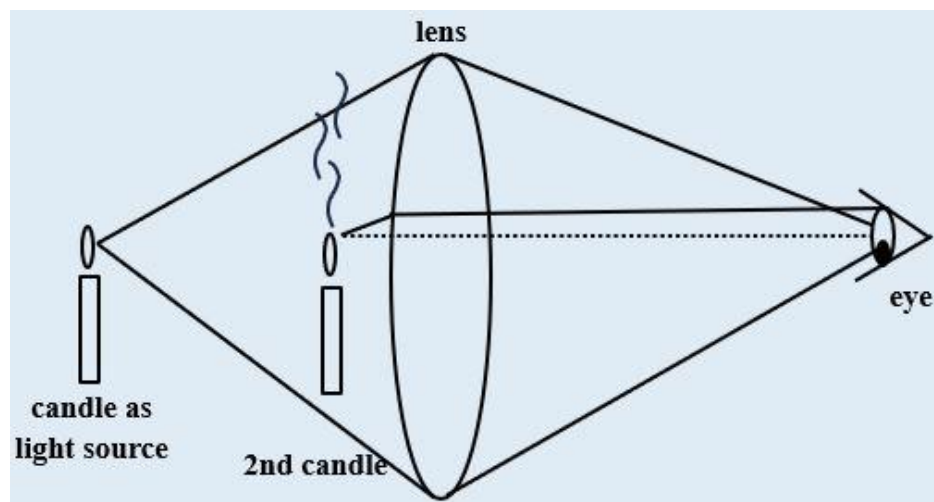


Figure 2.1: Schematic of Hooke's schlieren system

The next contribution in the field of schlieren flow visualization was made in 1859 by Leon Foucault when he introduced the knife-edge cutoff in the plane of image. This insight came into attention during the work done by Foucault in perfecting the existing telescopes of his time. However, the credit for first using schlieren technique as a scientific tool in visualizing density gradients and in upgrading the system from the time of his predecessors is given to German chemist and physicist August Toepler,

which is outlined in the literatures of (Schardin H. , 1970) and (Settles, 2001), and the method is named after him: Toepler schlieren method. The schematic diagram of the Toepler schlieren setup is shown in Figure 2.2. He used this technique to look at glasses and found out that the window glasses and optical glasses were full of streaks and striations, in German called schlieren, and that is how the technique got its name. Toepler had to deal with unfair accusations for stealing and rebranding Foucault's work, to which he responded that the thrust of his work was to develop schlieren technique in line with the methods of scientific study as dictated by the period of enlightenment, while Foucault was only concerned with the use of schlieren technique for perfecting telescope glasses and mirrors. Toepler continuously worked in further refining his schlieren setup for almost a decade, and during that time simultaneously performed many flow-visualization studies. If one were to remove the veil and looked into the history of schlieren technique, Toepler would stand as the most prominent figure.
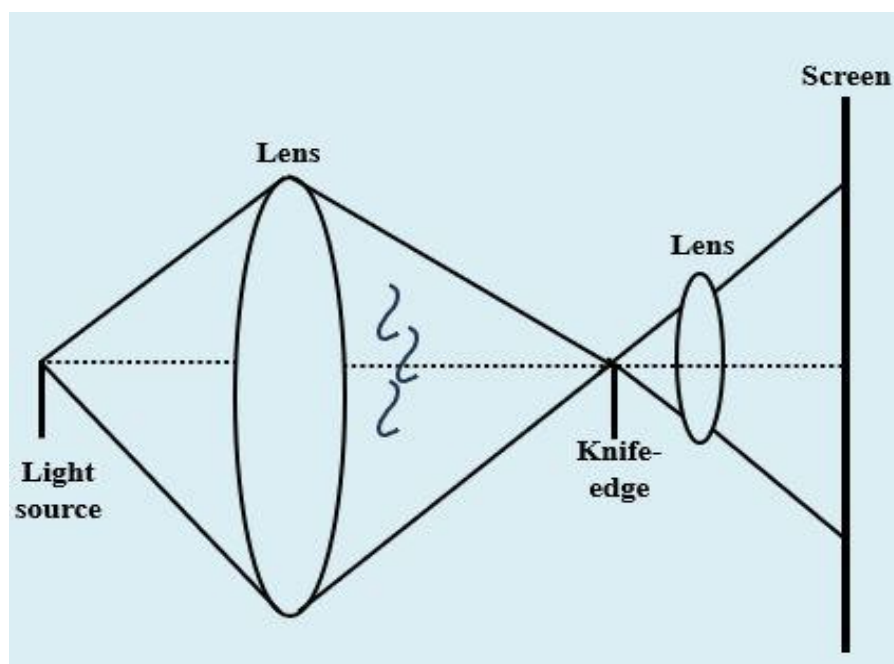


Figure 2.2: Schematic of Toepler's single-field-lens schlieren setup

The development of the schlieren technique during the $20^{th}$ century revolves mostly around the works done by Hubert Schardin. In his 1934 Ph.D. thesis "The Toepler Schlieren Technique-Principles for its Application and Quantitative Evaluation (Schardin H. , 1934)", Schardin provided a theoretical framework for the underlying physics of schlieren which was the first of its kind. In the later part of the $20^{th}$ century, many improvements were introduced in schlieren methods by various scientists, and

engineers. Amid the new developments, color schlieren and monochromatic schlieren methods remain an important optical visualization technique in glimpsing the intricacies of different fluid-flow phenomena, especially those involving density gradients.

In retrospect, schlieren method has provided the critical visualization in learning important phenomena in the field of physics and engineering. One of such phenomena is the shock wave. Figure 2.3 taken by Austrian physicist Ernst Mach and his colleague Peter Salcher using a schlieren setup is one of the most famous photographs in the history of experimental physics. It is the first experimental verification of the existence of the swept bow shock at the front tip of the bullet, tail shock, and turbulent region/ wake of the bullet. Around 50 years prior to this experiment, German mathematician Bernhard Riemann had written a paper where he had developed a way to solve the equations of motion for the acoustic waves. In that paper, Riemann had made a speculation that there could be a possibility of existence of waves that are stronger than sound waves and travel faster than the speed of sound. It took the experimental works from Ernst Mach and Peter Salcher using a schlieren technique to prove the theoretical speculation made by Riemann. Schlieren pictures, thus, are critical in showing the visualization of physics that is hidden in a flow-phenomena.



(a)                                                        (b)
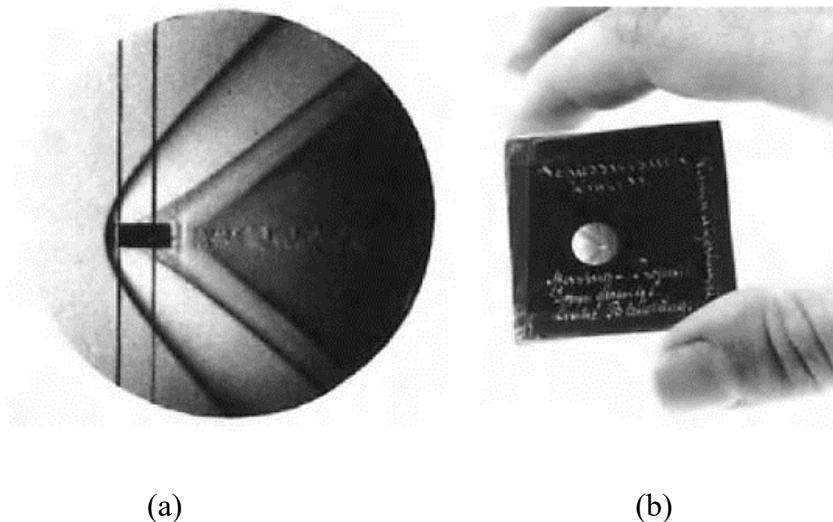
Figure 2.3: (a) Schlieren photograph taken by Ernst Mach and Peter Salcher of a brass bullet undergoing supersonic speed, (b) Original negative plate containing 5-mm-diameter image of the supersonic flow pattern (Mach & Salcher, 1887)

## 2.1.2 Mathematical basis

The mathematical basis of the schlieren imaging is built following Fermat's principle which states, "light travels between two points along the path that requires the least time, as compared to other nearby paths." If one considers a ray of light passing through a schlieren object, i.e., a region of inhomogeneities in density/refractive index, Fermat's principle naturally reduces to Snell's law, usually called the law of refraction. The ray of light upon interacting with the region of variable density become bent. The refractive index of a transparent medium which is given by the relation $n=c_0/c$ indicates this change, where $c$ is the light speed in the medium and $c_0$ is the light speed in the vacuum, $3\times10^8$ m/s. The mathematical model for schlieren imaging could be systematically built following Figure 2.4. It is assumed that there is a parallel illumination of a two-dimensional planar schlieren object, assumed along x- and y- direction, and there is no variation along the optical axis/ principal direction, z. It is further assumed that there is a negative vertical refractive-index gradient $\partial n/\partial y < 0$, and no gradient in the x- or z-direction. If there is no disturbance, light ray (an electromagnetic wave) propagates in such a way that the wavefront maintains a perpendicular direction to the direction of propagation. Thus, the planar wavefront would be initially vertical upon passing through $z_1$, and perpendicular to the horizontal optical centerline $z$.
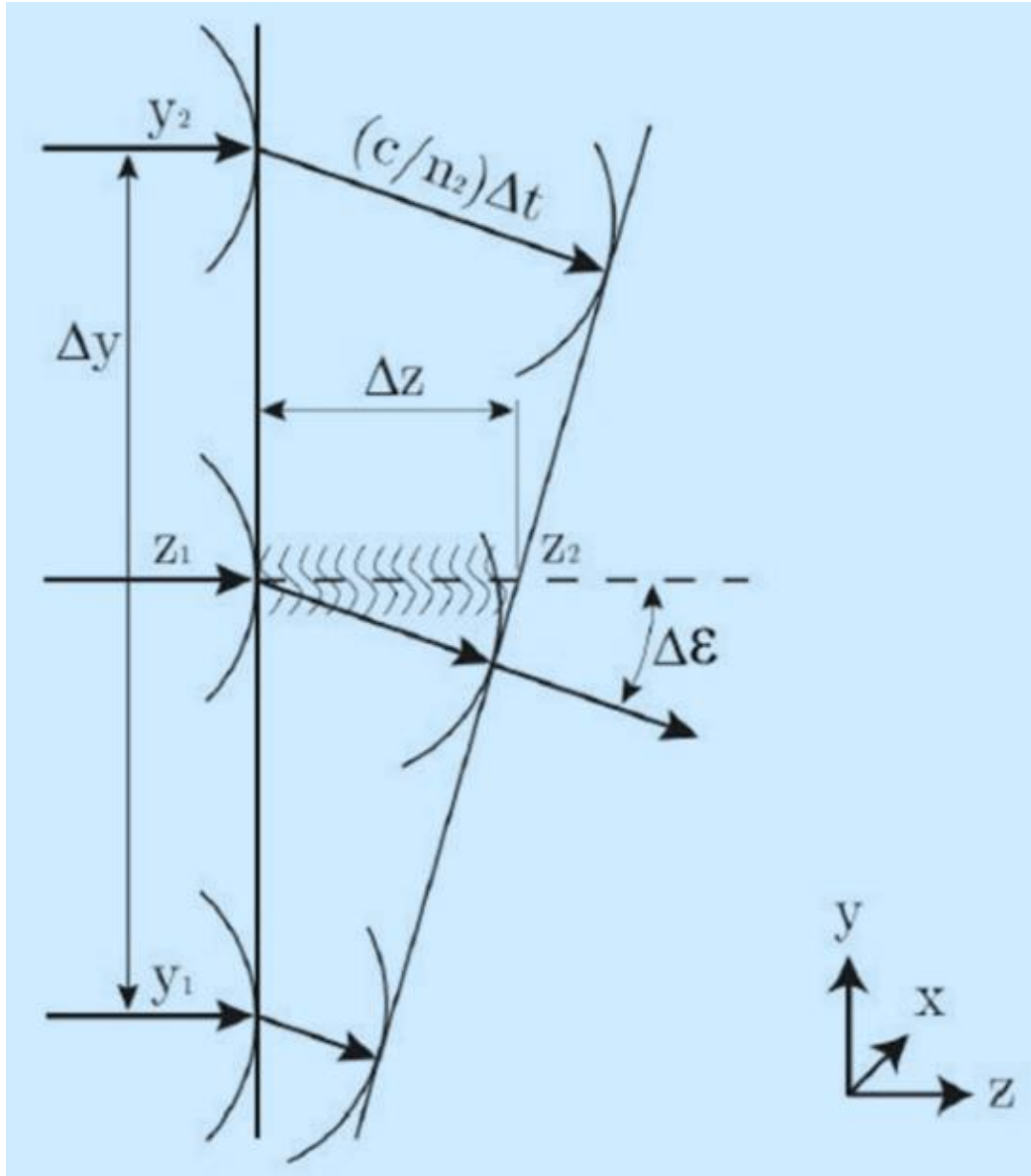
Figure 2.4: Diagram of elemental light ray refraction by a gradient in refractive index
*δn/dy*

Once this planar wavefront passes through the schlieren object via $z_1$ to $z_2$, it would cover a differential distance ($\Delta z$) in the differential time $\Delta t$. In the meantime, because of the presence of the density-gradient, the wavefront would undergo refraction and is deflected from its actual path by angle of $\Delta \varepsilon$. This deflection angle ($\Delta \varepsilon$) is given by,

$$\tan \Delta \varepsilon \sim \Delta \varepsilon = \frac{\left(\frac{c_0}{n_2} - \frac{c_0}{n_1}\right) . \Delta t}{\Delta y} \qquad \text{Eq. 2.1}$$

The differential time $\Delta t$ is given by,

$$\Delta t = \Delta z . \frac{n}{c_0} \qquad\qquad \text{Eq. 2.2}$$

Combining Eq. 2.1 and Eq. 2.2,

$$\Delta\varepsilon \approx \frac{c_0}{\Delta y} . \left(\frac{n_1 - n_2}{n_1 n_2}\right) . \Delta z . \frac{n}{c_0} \qquad\qquad \text{Eq. 2.3}$$

$$\Delta\varepsilon \approx \frac{n}{n_1 n_2} . \left(\frac{n_1 - n_2}{\Delta y}\right) . \Delta z \qquad\qquad \text{Eq. 2.4}$$

$$\frac{\Delta\varepsilon}{\Delta z} = \frac{n}{n_1 n_2} . \left(\frac{n_1 - n_2}{\Delta y}\right) \qquad\qquad \text{Eq. 2.5}$$

If all the finite difference tends to zero,

$$\lim_{\Delta z \to 0} \frac{\Delta\varepsilon}{\Delta z} \approx \left(\frac{n}{n_1 n_2}\right) . \left(\lim_{\Delta y \to 0} \frac{n_1 - n_2}{\Delta y}\right) \qquad\qquad \text{Eq. 2.6}$$

$$\frac{d\varepsilon}{dz} = \left(\frac{n}{n^2}\right) . \frac{dn}{dy} \qquad\qquad \text{Eq. 2.7}$$

$$\frac{d\varepsilon}{dz} = \frac{1}{n} . \frac{dn}{dy} \qquad\qquad \text{Eq. 2.8}$$

For small angle approximation:

$$\varepsilon \sim \frac{dy}{dz} \qquad\qquad \text{Eq. 2.9}$$

Implementing Eq. 2.9 into Eq. 2.8 and representing total derivatives as partial derivates which would allow one to get a general case where all refractive-index gradients would be present:

$$\frac{\partial^2 y}{\partial z^2} = \frac{1}{n} . \frac{\partial n}{\partial y} \qquad\qquad \text{Eq. 2.10}$$

Similarly,

$$\frac{\partial^2 x}{\partial z^2} = \frac{1}{n} . \frac{\partial n}{\partial x} \qquad\qquad \text{Eq. 2.11}$$

Eq. 2.10 and Eq. 2.11 relates refracted light ray's curvature to the magnitude of its corresponding refractive-index gradient. Integrating once, the angular ray deflection's component in the x- and y-directions are obtained:

$$\varepsilon_x = \frac{1}{n} \int \frac{\partial n}{\partial x} \partial z \qquad \text{Eq. 2.12}$$

$$\varepsilon_y = \frac{1}{n} \int \frac{\partial n}{\partial y} \partial z \qquad \text{Eq. 2.13}$$

Considering a two-dimensional schlieren of extent L along the principal direction, Eq. 2.12 and 2.13 reduces to the form:

$$\varepsilon_x = \frac{L}{n_0} \frac{\partial n}{\partial x} \qquad \text{Eq. 2.14}$$

$$\varepsilon_y = \frac{L}{n_0} \frac{\partial n}{\partial y} \qquad \text{Eq. 2.15}$$

where $n_0$ is the refractive index of the surrounding medium. Eq. 2.10-2.15 provide the mathematical basis for the schlieren system. Eq. 2.10 and 2.11 indicates that it is not the refractive index $n$ causing ray deflection, but the gradient $\frac{\partial n}{\partial x}$ or $\frac{\partial n}{\partial y}$ of the refractive index. Additionally, Eq. 2.14 and 2.15 show that light ray deflections bend towards the region of higher refractive index. The illuminance level in a schlieren image as presented in Table 1.1 responds to the first spatial derivative of the refractive index in the schliere, e.g., $\frac{\partial n}{\partial x}$ and the schlieren image displays the deflection angle $\varepsilon$ (Settles, 2001).

### 2.1.3 Z-Type Two-Mirror Schlieren Imaging Setup

It is a subset of the schlieren imaging system consisting of two telescope parabolic/ spherical mirrors which are oppositely tilted to each other. It is the most popular schlieren system and its schematic diagram is shown in Figure 2.5. The combination of a diverging light beam from coherent point light source, an opposite converging analyzer beam, and a parallel beam between the two mirrors mimics the letter $z$, hence the name z-type schlieren is given to this setup. In this setup, the light from a bright

coherent point light source is initially directed towards the first schlieren mirror. The light source is placed at one focal length distance away from the mirror inclined at a certain angle from the optical centerline. The first mirror collimates the light beam which produces parallel rays of light in the test region. This parallel beam of light ultimately falls upon the second schlieren mirror. The second mirror then focuses the collimated light towards the external cut-off (knife-edge or color-filter) and camera. When the parallel beam of light passes through the test section, it gets bent due to the varying indices of refraction and causes a schliere. This effect produces a varying shade of light (monochromatic or color) allowing one to visualize the changes in density of a fluid (Kaessinger & Kors, 2014). The distance between the two schlieren mirrors is usually kept about $2f$, where $f$ is the mirror focal length (both mirrors have the same specifications). There is no restriction for maintaining longer distances than $2f$ and it is usually favorable when visualizing flow of a large fluid domain.
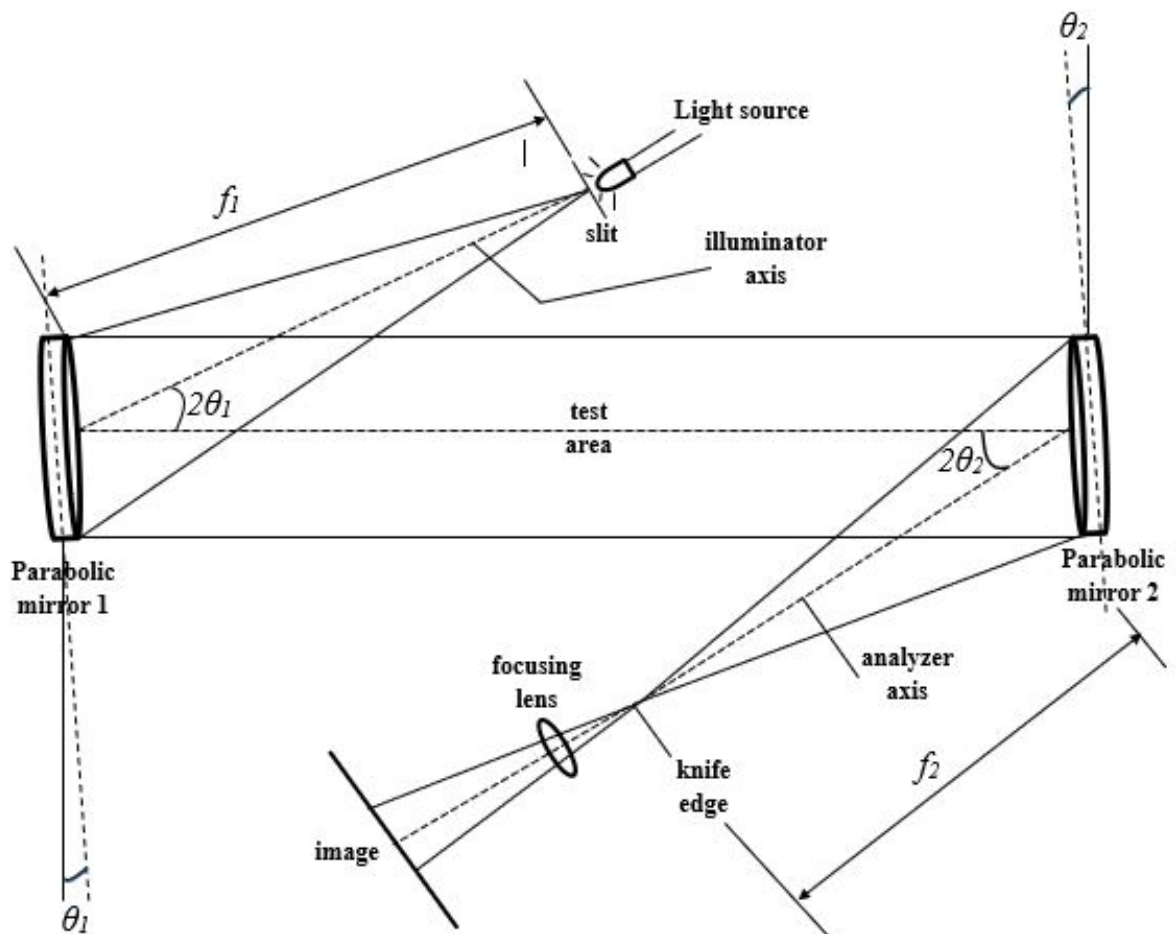


Figure 2.5: Schematic diagram of z-type schlieren imaging setup

## 2.1.4 Schlieren Imaging Issues

In spite of the proper alignment and good quality of optical equipment used for setting up a schlieren system, few issues are always encountered. These include scratches or imperfections in mirror surfaces, imperfections in illumination because of incoherent light source, mirror alignment, etc. These in some instances could diminish the quality of the schlieren images. Most of these issues could be mitigated or reduced by maintaining better alignment, cleaning of mirrors/ lenses, and improvement on quality of optical equipment. However, there are two other issues which require more technical knowledge to mitigate or reduce.

### (i) Coma

Coma also called comatic aberration, is an optical aberration, which occurs when the direction maintained by the reflected light is a function of the point of refection in the mirror. This is caused because of tilting the schlieren mirrors from their optical axes (Settles, 2001). A schlieren system infused with coma would spread the focus initially a point into a line. The name "coma" was actually inspired by the aberration's appearance because it resembles a comet's tail as it emanates from the focus point (Tkaczyk, 2010).

The severity of comatic aberration increases if one were to increase the offset angles $\theta_1$ and $\theta_2$ as shown in Figure 2.6, and to the inverse square of mirror focal-number for a specified $\theta$. The severity could thus be minimized by maintaining the value of $\theta$ as small as possible and using mirrors with long focal length. There is an interesting point about the impact of coma in the z-type schlieren setup. Since, coma is generated in off-axis mirrors, and z-type schlieren setup includes two such mirrors tilted in opposite axis to each other, the combined coma effect of the setup could be kept zero. For this, one has to maintain angles $\theta_1$ and $\theta_2$ in opposite directions from the central optical axis.
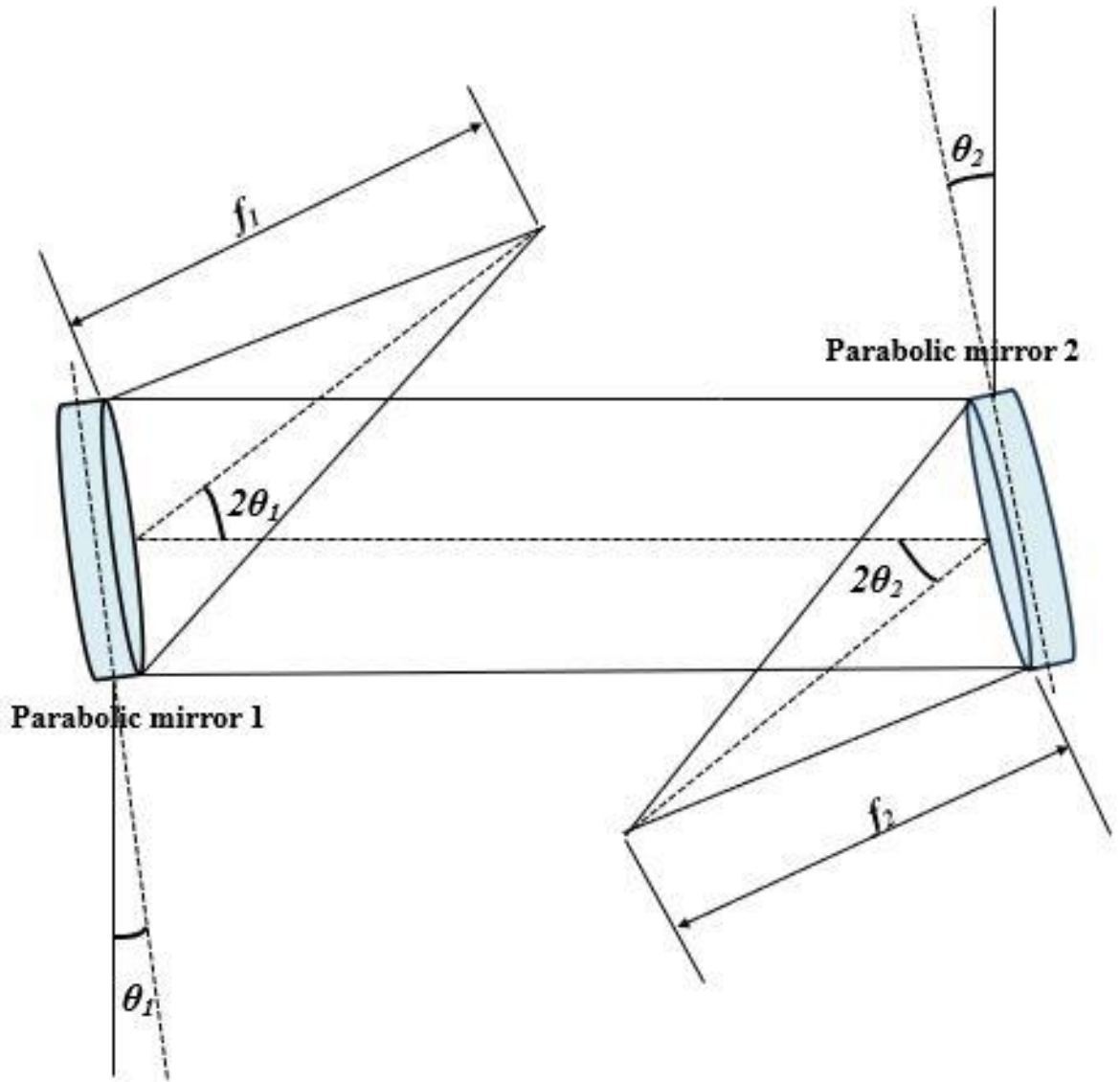
Figure 2.6: Top view of the z-type schlieren setup illustrating the comatic aberration. Mirrors are counter-rotated about their mean axis at equal angles ($\theta_1 = \theta_2$), canceling out the coma effect.

**(ii) Astigmatism**

Astigmatism comes from the combination of Greek words, meaning "without" and "mark" or "spot", in literal terms meaning "non-point like", or "failure to focus a point to a point" (Settles, 2001). It is a much bigger problem compared to coma and it would always be present in an off-axis optical system irrespective of how hard one tries to mitigate it, either by minimizing the off-axis angles or using larger focal length mirrors. The reason for the existence of astigmatism is because of the off-axis rotation of the two mirrors, giving a difference in path length along the optical centerline and mirror periphery. Due to finite off-axis angles $\theta_1$ and $\theta_2$, a point light source is imaged as two short lines at right angles to one another and spaced apart a small distance $\Delta f$ along the optical axis (Weinberg, 1963). This difference as shown in Figure 2.7 is usually the parameter indicating the severity of astigmatism present in the off-axis optical setups. It is given by the geometric formula (Speak & Walters, 1950), (Shafer, 1949):

$$\Delta f = f.\frac{\sin^2\theta}{\cos\theta} \qquad \text{Eq. 2.16}$$

where $\theta$ is the mirror (optical) offset angle. If the offset angle is small ($\ll 1°$), Eq. 2.16 gets simplified to:

$$\Delta f = \frac{d^2}{4f} \qquad \text{Eq. 2.17}$$

where $d$ is the diameter of the schlieren mirror. The use of small offset angle ($\theta$) and long focal length ($f$) mirrors could reduce the astigmatism severity by a great extent, but not completely eliminate it. As suggested in literature of (Settles, 2001), it is a good practice to minimize the severity of both astigmatism and coma by reducing the offset angle $\theta$ and using mirrors with greater $f$-number (usually in the range of $6 \leq f$-number $\leq 12$).
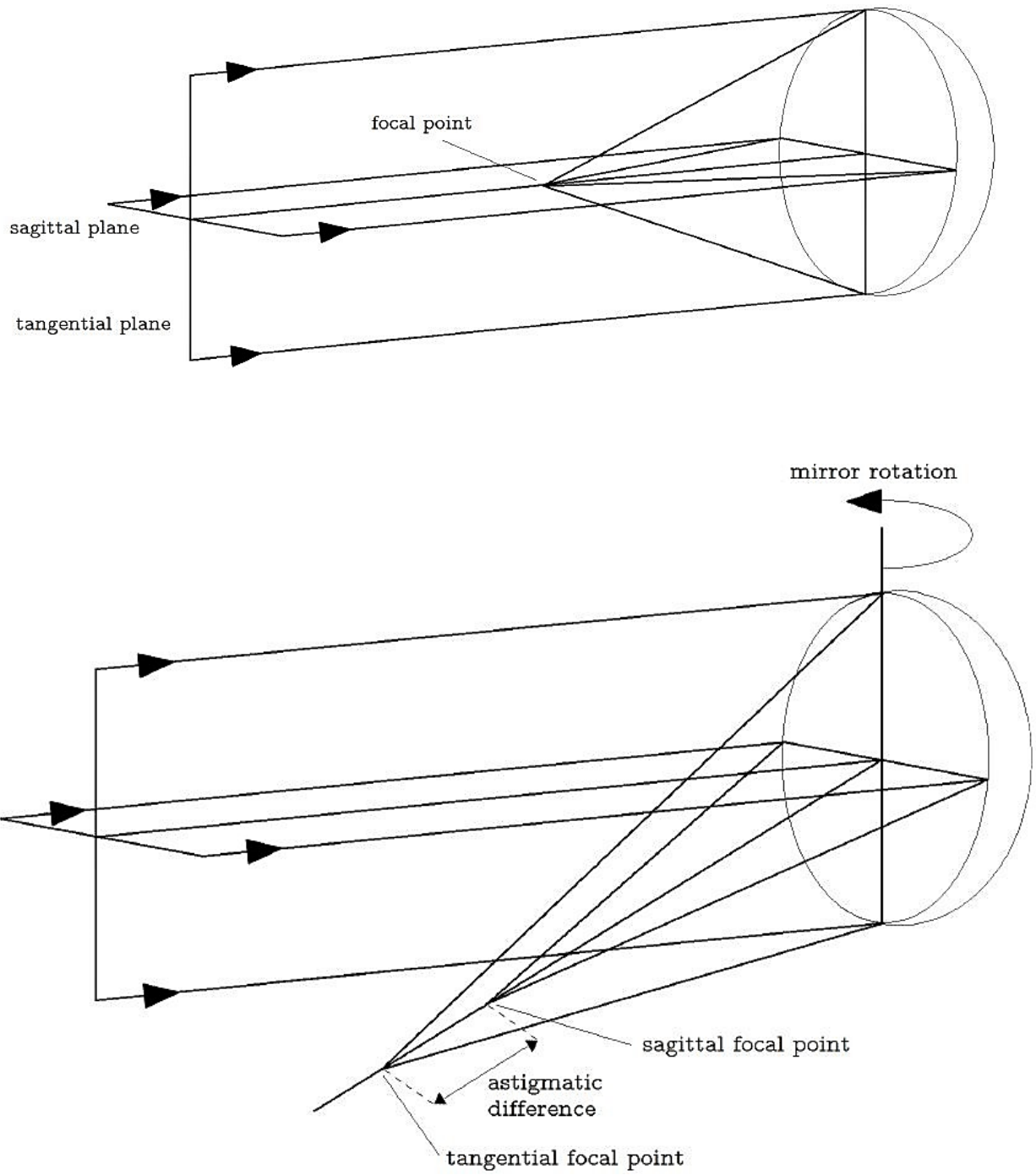
Figure 2.7: Schematic diagram of astigmatism occurrence due to mirror rotation
(Nordberg, 2015)

## 2.2 De-Laval Nozzle Flow

De Laval nozzle (also called the converging-diverging nozzle) whose simple schematic diagram is shown in Figure 2.8 incorporates a variation in the interior flow to transform a subsonic flow to a supersonic flow. The nozzle comprises of a converging section, a throat, and a diverging section. If the nozzle is designed correctly, the flow via de Laval nozzle begins as subsonic in the converging section, transitions between subsonic and supersonic at the throat, and supersonic in the diverging section (Robinson, 2016). The flow through the de Laval nozzle is driven by the pressure gradient along the nozzle.
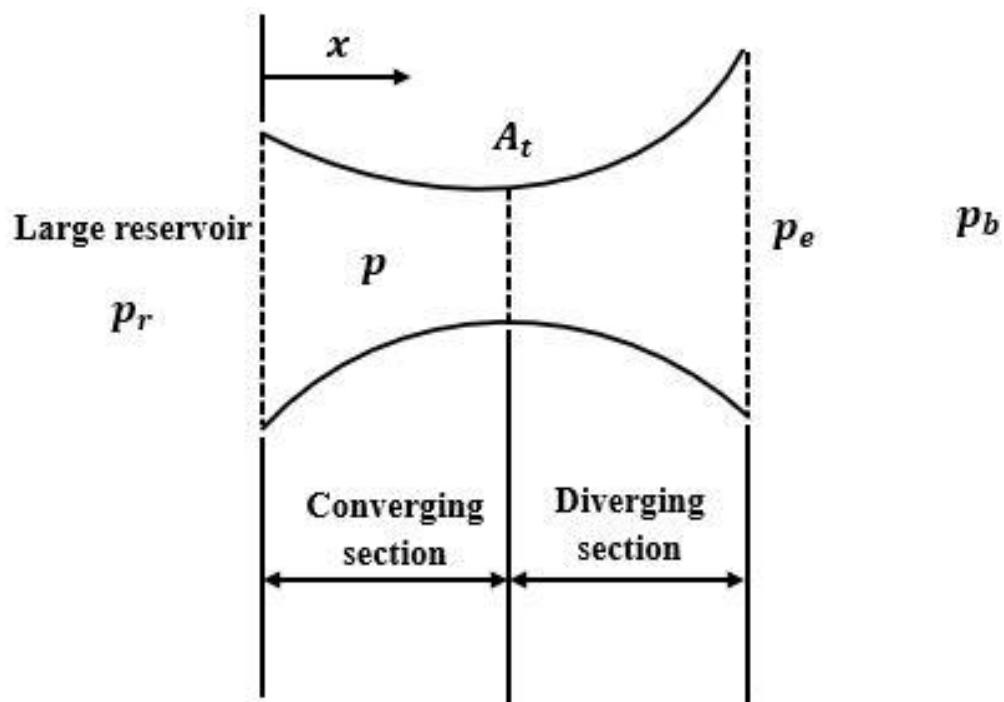


Figure 2.8: Schematic of a simplified de-Laval nozzle (converging-diverging nozzle)

The parameters shown in Figure 2.8 are mentioned below:

- $p_r$ : stagnation pressure inside the reservoir
- $p$ : static pressure in nozzle
- $x$ : distance along the nozzle
- $A_t$: throat area
- $P_e$: static pressure at the nozzle exit
- $A_e$: area of exit plane of the nozzle
- $p_b$: Background (back) pressure that nozzle exhausts into

## 2.2.1 No flow conditions

Let us consider a simple de Laval nozzle whose converging section (left starting portion) is connected to a large hypothetical 'still air' reservoir having total pressure and enthalpy of $p_r$ and $h_r$. It is further considered that variations could be made to the back pressure $p_b$. If the value of exit static pressure is varied such that $p_e = p_r$, there would be zero pressure gradient which implies no driving force to produce flow inside the nozzle. This condition is shown in Figure 2.9.
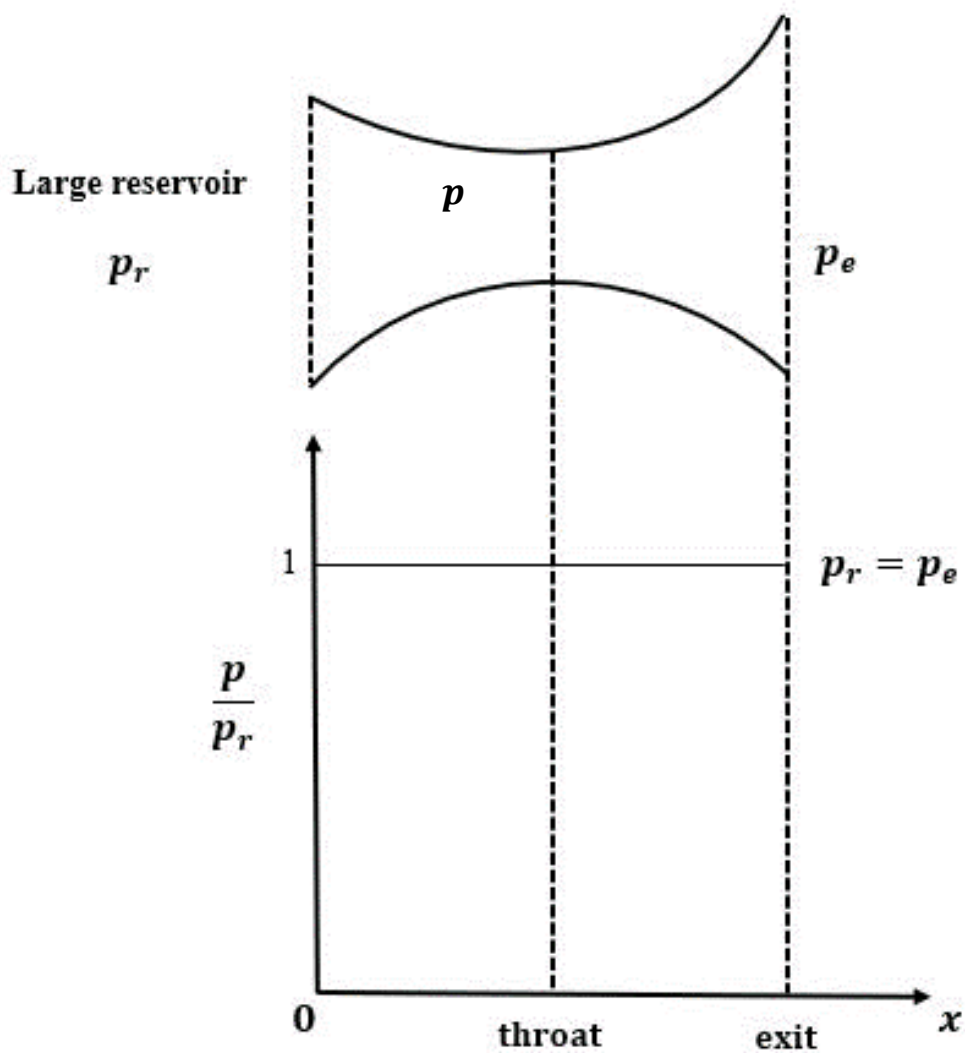


Figure 2.9: No flow condition inside the de Laval nozzle

## 2.2.2 Isentropic subsonic flow throughout the nozzle

If $p_b$ is reduced to a value lower than $p_r$, the negative pressure gradient will induce the flow of air inside the nozzle. Since the flow is subsonic in the converging section of the nozzle, the velocity of the flow would increase (pressure decreases) and reaches its maximum value at the throat. Beyond the throat the velocity of the flow decreases (pressure increases) because of the diverging section. The pressure increases up to the point where at the exit, it equals the back pressure $p_b$. There would be an infinite number of solutions to this flow situation depending upon the input parameters chosen. This flow condition is shown in Figure 2.10.
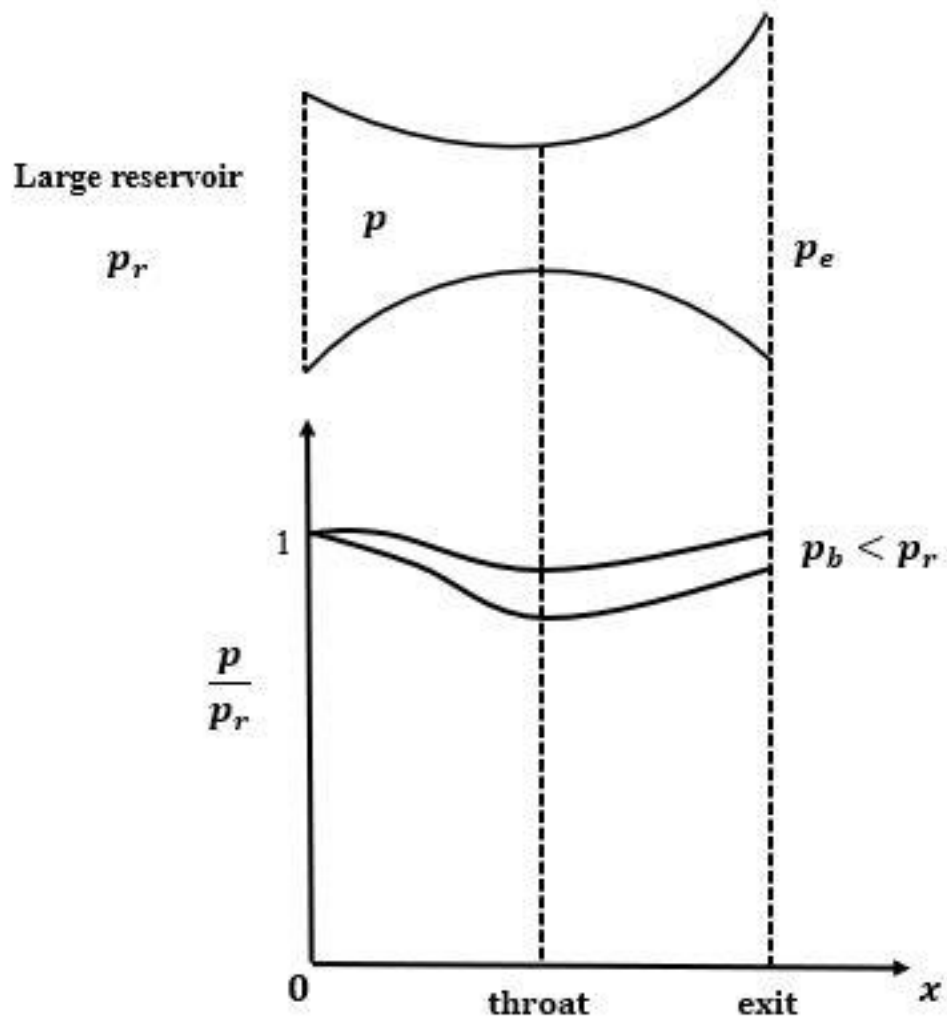


Figure 2.10: Isentropic subsonic flow inside the de Laval nozzle

## 2.2.3 Choked Isentropic Subsonic and Supersonic flow

If the value of $p_b$ is further reduced, the condition of choked flow (Mach number = 1) is achieved at the throat of the nozzle. The value obtained for the pressure ratio $p^*/p_r$ dictates the occurrence of the choked flow at the nozzle throat, which is calculated as:

$$\frac{p^*}{p_r} = \left(1 + \frac{\gamma - 1}{2} \times M_t{}^2\right)^{\frac{-\gamma}{\gamma - 1}}$$  Eq. 2.18

where,

$p^*$: static pressure at the nozzle throat during choked flow

$M_t$: Mach number at the nozzle throat

$\gamma$: Ratio of specific heat capacity of air at constant pressure to its specific heat at constant volume

For $\gamma = 1.4$, the pressure ratio is found to be 0.5283. Following from the Area-Mach Number relation shown in Eq. 2.19, the flow in the converging section is subsonic leading to the increment in velocity and subsequent decrement in pressure. Since the flow is choked, the velocity at the nozzle throat reaches a value which corresponds to Mach Number equals to 1. This path taken by the pressure ratio $p/p_r$ up until the throat of the nozzle as shown in Figure 2.11 would not change irrespective of any variation in the back pressure $p_b$. The nature of the flow in the diverging section depends on the pressure ratio $p_b/p_r$ as shown in Table 2.1. If this ratio falls under the subsonic regime, the subsequent flow in the diverging section would be subsonic in nature and vice-versa. It is to be noted that for all the cases discussed in Table 2.1, the flow is isentropic throughout the nozzle, i.e., $p_b = p_e$.

$$\frac{A}{A^*} = \left(\frac{\gamma + 1}{2}\right)^{\frac{-(\gamma+1)}{2(\gamma-1)}} \times \frac{\left(1 + \frac{\gamma-1}{2}M^2\right)^{\frac{\gamma+1}{2(\gamma-1)}}}{M}$$  Eq. 2.19
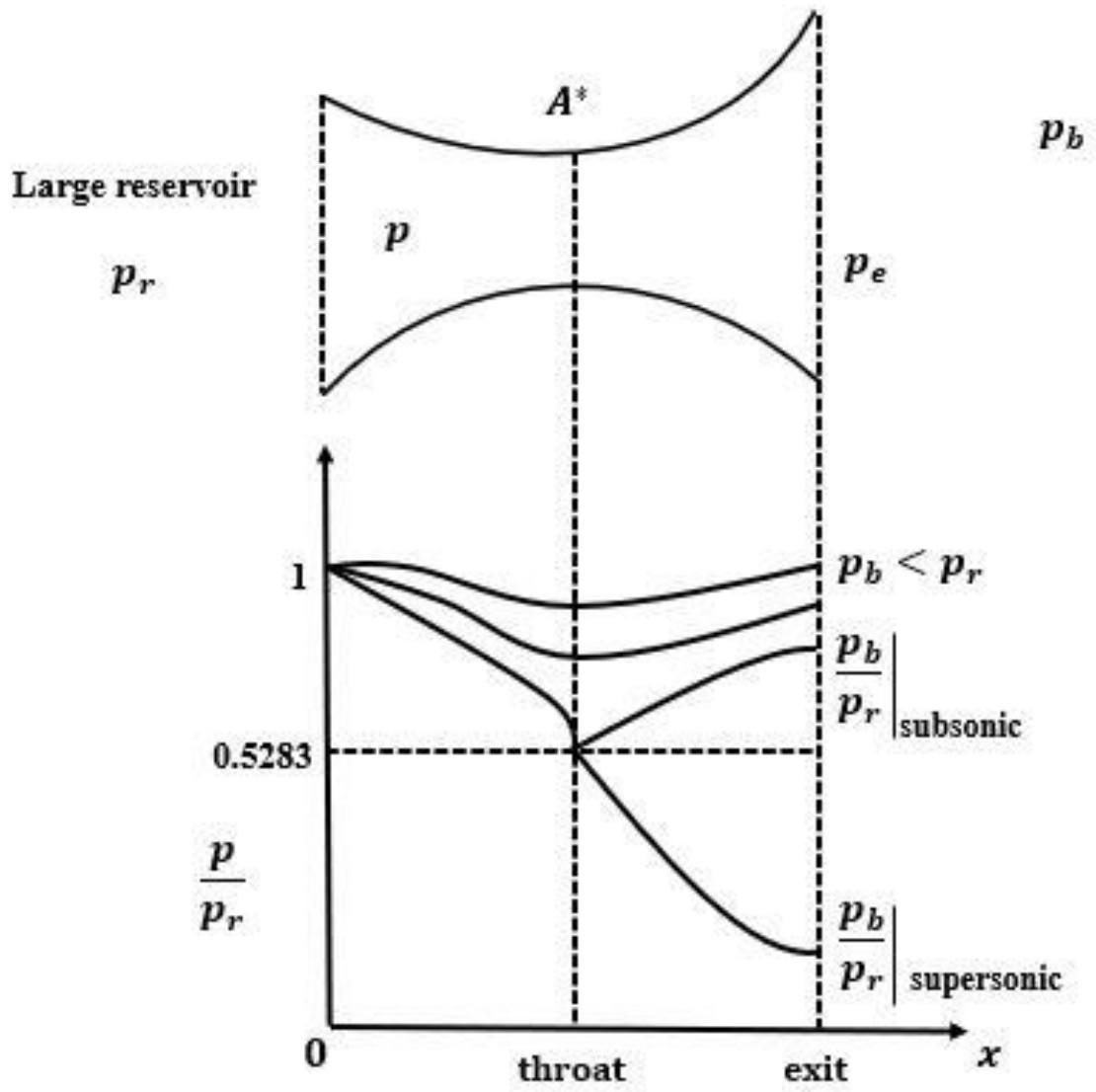
Figure 2.11: Choked isentropic subsonic and supersonic flow criteria inside the de Laval nozzle

Table 2.1: Different flow conditions existing inside the nozzle for corresponding pressure ratio values

| Case-1 | $\dfrac{p_b}{p_r} > \left(\dfrac{p_b}{p_r}\right)_{\text{subsonic}}$ | Subsonic flow throughout the nozzle |
|---|---|---|
| Case-2 | $\dfrac{p_b}{p_r} = \left(\dfrac{p_b}{p_r}\right)_{\text{subsonic}}$ | Subsonic flow throughout the nozzle except at the throat where $M_t = 1$ |
| Case-3 | $\dfrac{p_b}{p_r} = \left(\dfrac{p_b}{p_r}\right)_{\text{supersonic}}$ | Subsonic flow in the converging section, sonic flow at the throat, and supersonic flow in the diverging section |

## 2.2.4 Normal Shock Formation inside the Nozzle

If the pressure ratio $p_b/p_r$ is decreased further,

$$\frac{p_b}{p_r} < \left(\frac{p_b}{p_r}\right)_{\text{subsonic}}$$

the nozzle will try to fulfill its objective of getting the pressure at the exit plane of the nozzle ($p_e$) to be equal to the back pressure ($p_b$). However, in this situation the back pressure is too low for the occurrence of usual subsonic flow in the diverging section. So, there is formation of a normal shock in the diverging section of the nozzle. This formation of normal shock results in the increment of pressure across it, and a subsequent subsonic flow afterwards. The location of the normal shock inside the nozzle depends on the pressure ratio $p_b/p_r$. The normal shock formation is not an isentropic process. This flow condition is shown in Figure 2.12.
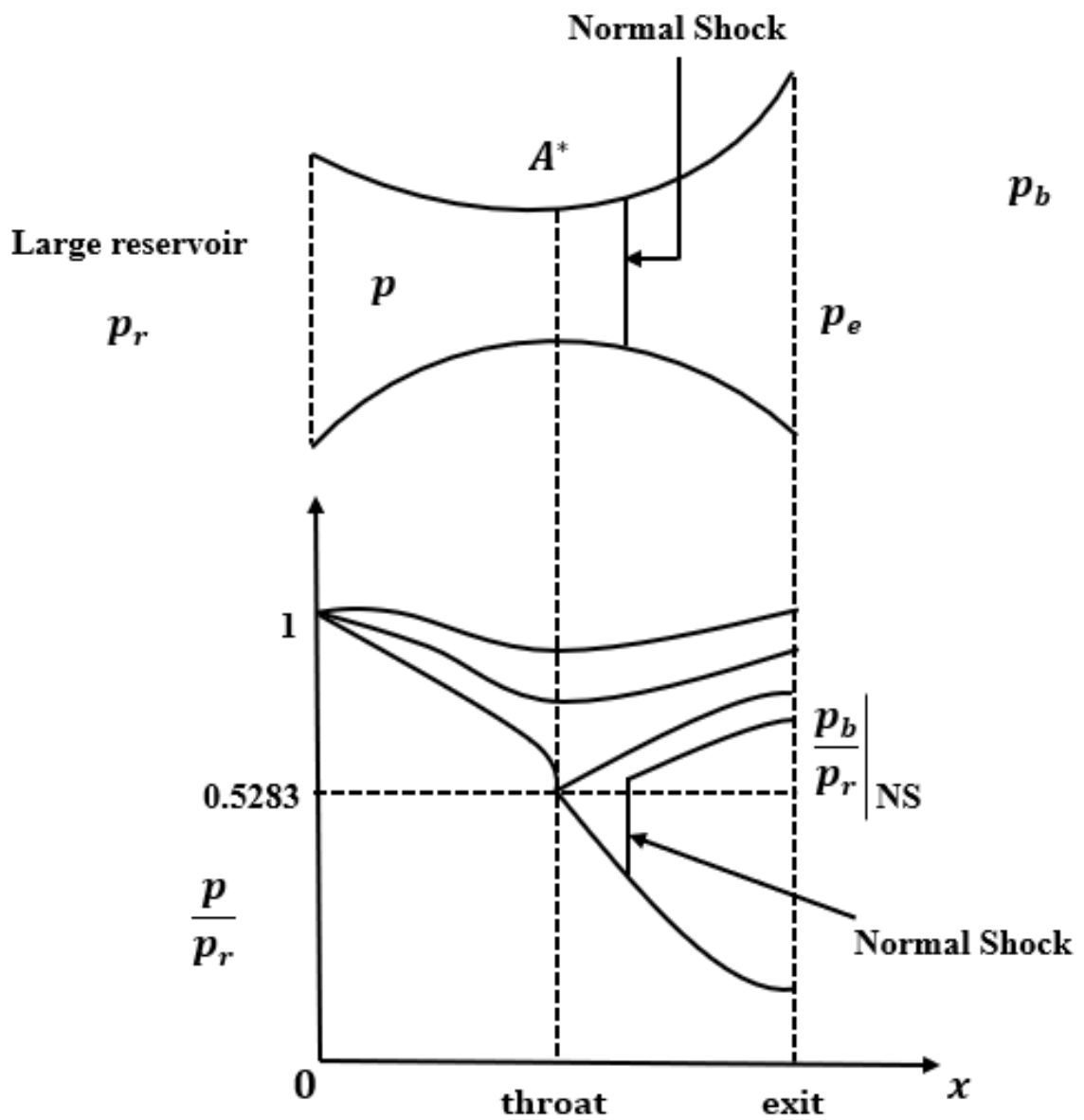
Figure 2.12: Formation of normal shock inside the nozzle

## 2.2.5 Normal shock at the Nozzle exit

This flow condition is met when the back pressure $(p_b)$ is decreased to a point such that the normal shock would exist at the exit plane of the nozzle. This is the limiting case of the formation of normal shock inside the nozzle and also the last flow condition that would cause changes inside the nozzle. From this flow condition onwards, changes would only occur outside the nozzle, among which the 'under-expanded flow' and its visualization is the gist of this research work. The flow condition resulting in the formation of normal shock at the nozzle exit plane is shown in Figure 2.13.
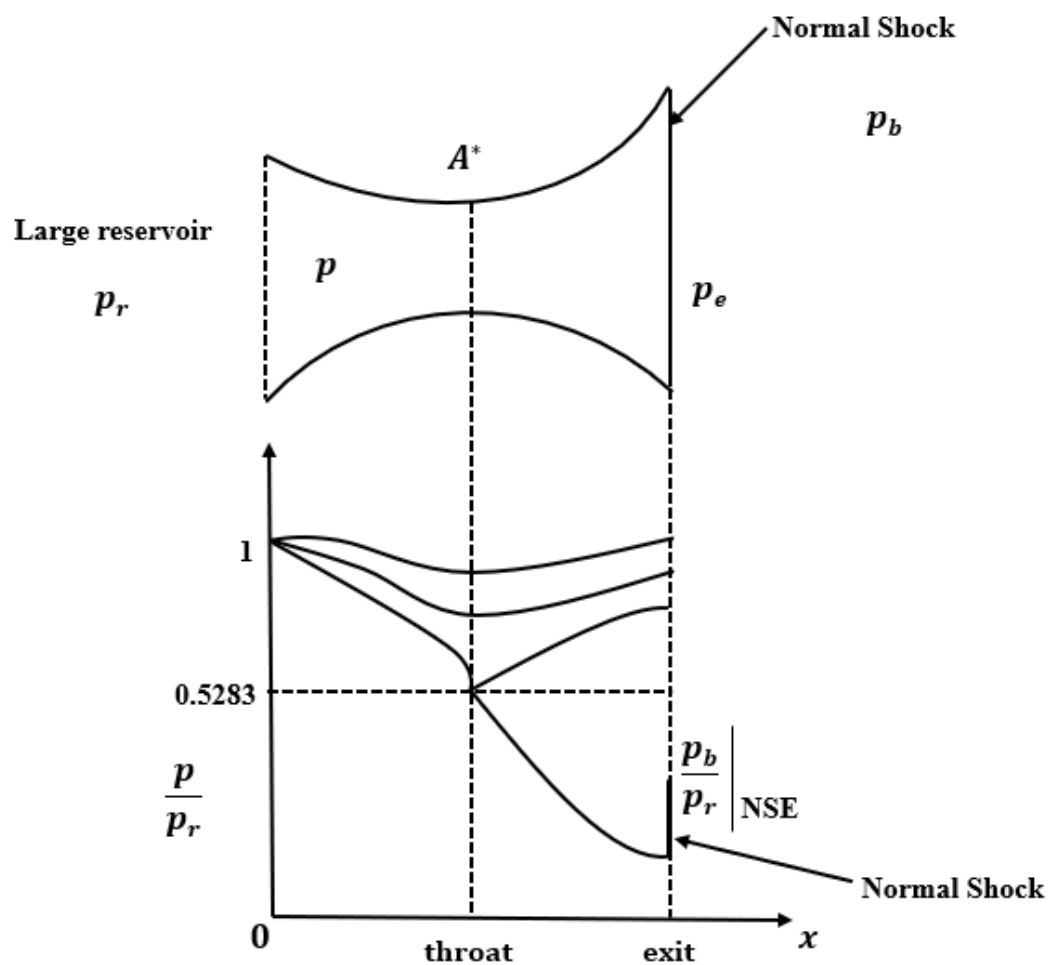


Figure 2.13: Formation of normal shock at the exit plane of the nozzle

## 2.2.6 Over-expanded flow

The over-expanded flow is met when the back pressure $(p_b)$ is decreased further from the normal shock at the exit plane case, but such that it is still greater than the $p_b/p_r$ for supersonic isentropic flow throughout the nozzle, i.e.,

$$\left(\frac{p_b}{p_r}\right)_{NSE} > \frac{p_b}{p_r} > \left(\frac{p_b}{p_r}\right)_{supersonic}$$

The normal shock in this case would be too strong, i.e., it would increase the pressure past the back pressure that had been set. So, the pressure is increased by a weaker oblique shock outside the nozzle. The flow is called overexpanded because the nozzle in this flow condition expands the flow too much such that the exit pressure $(p_e)$ gets lower than the back pressure $(p_b)$. In this flow condition, a series of oblique shock waves and expansion fans are produced so that the nozzle ultimately fulfills its objective, i.e., equating $p_e$ and $p_b$. The flow condition is shown in Figure 2.14.
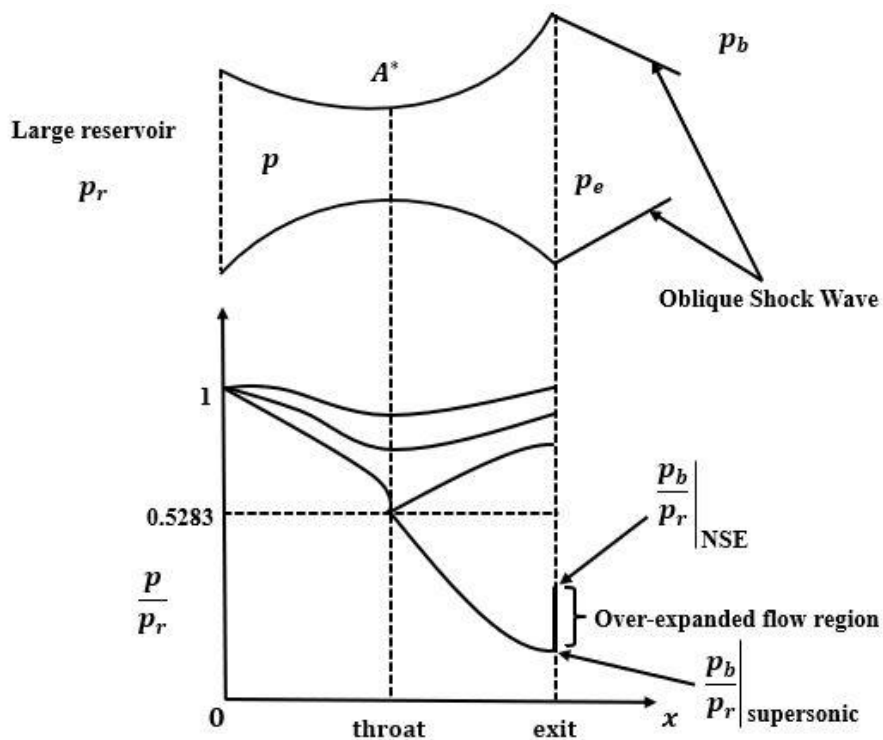


Figure 2.14: Over-expanded flow condition

## 2.2.7 Under-expanded flow

The under-expanded flow condition is met when the back pressure is decreased further than over-expanded condition such that

$$\frac{p_b}{p_r} < \left(\frac{p_b}{p_r}\right)_{supersonic}$$

The flow is called under-expanded because the nozzle cannot expand the gas/ air enough resulting in the exit pressure being higher than the back pressure ($p_e > p_b$). The nozzle uses expansion fans as means to decrease the pressure. The process through the expansion fans is isentropic in nature. In this flow condition, a series of expansion waves and oblique shock waves are formed so that the nozzle could fulfill its objective of equalizing the exit pressure ($p_e$) to the back pressure ($p_b$). The flow condition is shown in Figure 2.15.
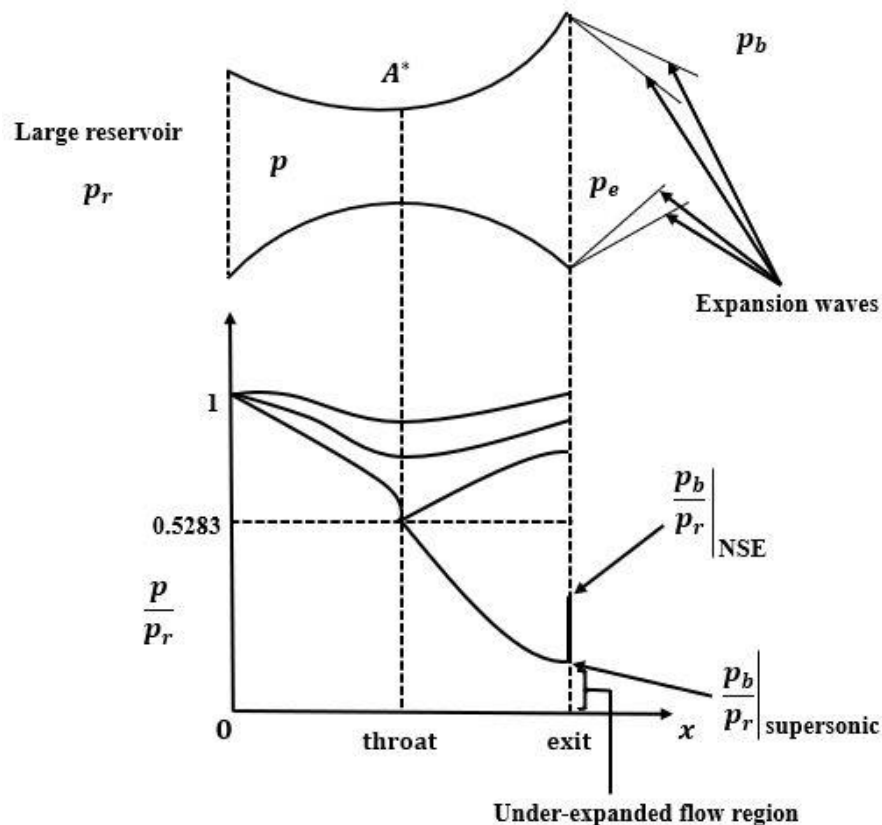


Figure 2.15: Under-expanded flow condition

## 2.3 Previous Works

### 2.3.1 Study on Negatively Buoyant Plumes using Schlieren Imaging

(Strutevant, 1990) in the research program investigated the initiation of non-linear processes due to shock-wave interaction with gas-gas interaction in the resulting plume. The research mainly placed its focus on the non-linear stages, namely the Rayleigh-Taylor instability and the resulting secondary instabilities (Kelvin-Helmholtz instability). Schlieren imaging was used to capture the visible thickness of the interface.

(Travers, 2012) in the study performed a setup of z-type color schlieren system to visualize the plumes of cold water falling from ice onto warm water beneath. With the interpretation of color (gradual tone fluctuations) in the resulting schlieren image based on the color filter used, the author was able to derive information about the temperature and corresponding density changes in the descending plume.

### 2.3.2 Study on Supersonic flow from a CD-Nozzle using Schlieren Imaging

(Mitchell, Honnery, & Soria, 2007) in the study performed an experimental investigation of under-expanded jets. The authors used a high frame-rate shadowgraph technique to access shock position and stability. The resulting shadowgraph images showed highly unstable shock structures present at lower pressures, resulting in periodic oscillations in angle and position.

(Kamalasekaran, 2020) in the project dealt with the optimization of CD-nozzle used in the process of fraction of powder produced by gas atomization suitable for different manufacturing processes. A CFD model of the CD-nozzle was created and the numerical results were validated using the images obtained through the shadowgraph technique (which is a technique similar to schlieren imaging). The author through this study found that the results of the CFD-model and the experiment followed similar trend but the absolute scale of gas jets did not match.

(Faheen, et al., 2021) in the study performed schlieren flow visualization of the under-expanded jet from a Mach 2.0 nozzle and from the schlieren images achieved reasonable estimates of Mach number along the jet centerline upon comparison with

the numerical study. The experimental tests were performed in the supersonic jet facility of the Indian Institute of Technology, Kanpur.

(ANL, Sundararaj, & Khan, 2022) in the study used a z-type schlieren setup to visualize the supersonic flow through a CD-nozzle designed for Mach 2.5 in high altitude test (HAT) facility of Karunya University, India. The inlet pressure for the nozzle in the study was varied from 4.5 to 10 bar. The HAT test facility was characterized for various NPR and the authors through all those tests concluded that the optimum flow for the designed CD-nozzle was at 14 NPR for 33 s for the inlet pressure of 4.5 bar.

### 2.3.3 Study on Supersonic flow from a CD-Nozzle using Schlieren Imaging in Institute of Engineering, Pulchowk Campus

The present research work is influenced in particular by two works that has laid foundation for the schlieren flow visualization technique in Institute of Engineering, Pulchowk Campus. This work takes inspiration and with a sincere gratitude is an attempt to help continue the development in the field of optical-flow-visualization started by the following works.

(Ranabhat, 2022) in the study focused on the exhaust flow from a CD-nozzle. The study was proceeded with the design of CD-nozzle considering exit-Mach-number to be 2. CFD analysis was carried out for NPR varying from 1.9 to 15. For the validation of CFD results, an optical single-mirror schlieren imaging system was established and monochrome schlieren image of the exhaust flow was captured.

(Gautam, Budhathoki, & Sitoula, 2023) in the study presented the design-procedures of the supersonic CD-nozzle along with visualization of the supersonic compressible flow using the optical methods (shadowgraph and single-mirror schlieren technique). The authors designed an experimental support system for visualization of supersonic flow through the CD-nozzle such that the thrust generated against the nozzle during its operation did not interfere with the flow visualization process. The resulting shadowgraph and schlieren images showed high gradient in pressure, temperature, and density.

### 2.3.4 Study on Fluidic Thrust Vectoring using Schlieren Imaging

(Pelt, Neely, & Young, 2015) in their study performed analytical and numerical analysis on shock vector control (SVC), where a fluid is injected into the supersonic part of the nozzle to generate side force. The study aimed at validating different analytical relations for predicting side force, against modern CFD techniques and finally preparing for experimental validation (carried out using schlieren technique).

(Shakouchi & Fukushima, 2022) in their study proposed the fluidic Coanda (FC)-nozzle which could be used for the thrust vectoring control of supersonic jets. The characteristics of the flow and the deflection induced by the Coanda effect upon closing specific suction pipes present in the Coanda nozzle is visualized by a schlieren method present in (KATO KOKEN, ss150, Japan).

# CHAPTER THREE: RESEARCH METHODOLOGY

The objectives of the current work have been presented in the first chapter. To meet those objectives, it is necessary to have a systematic approach on how the research work is conducted, how the research progress is quantified or measured, and what constitutes a success. This chapter outlines the key details associated with the research work such as the nature of the research work, how and what type of data is collected, and how the results would be interpreted.

## 3.1 Research Nature

The research study, being experimental research, falls under the category of empirical research. It is based on observation and measurement of fluid-flow phenomena, as directly experienced by the researcher. The data generated for this research would be the schlieren images and it would be compared against an established fluid-flow theory. The data gathered would be primary data, although secondary data from literature review may be considered in few places. The research work follows a deductive approach, where a theoretical view-point of the fluid-flow phenomena is taken into consideration and is tested in the fabricated schlieren setup to validate the sensitivity and accuracy of the resulting schlieren images.

## 3.2 Theoretical framework

The research study, despite falling under empirical research, does not divorce itself from the theoretical considerations. It could be said that the current research work is an osmosis of multitude of theoretical works done on the field of optical flow visualization by many great scientists starting from Robert Hooke in the early 17th century, Christiaan Huygens in the 18th century, Leon Foucault and August Toepler in the 19th century, and most notably by Hubert Schardin in the 20th century. The link between the research work and theory is symbiotic and the results for different fluid-flow phenomena from the research work is compiled to test its validity against the existing theories on those flows.

## 3.3 Overview of Methodology

The proposed methodology for the research work is shown in Figure 3.1.



Figure 3.1: Flowchart for research process

## 3.4 Literature Review

The research study, as mentioned before, focuses on the experimental setup of z-type schlieren imaging system. To paraphrase a famous quotation about schlieren and shadowgraph techniques, "Between microskopie and telescopie come strioscopie and ombroscopie-schlieren and shadowgraphy techniques in English". In that regard, this research study includes the fundamentals of optics, principle of light propagation through an inhomogeneous media, and principle behind the schliere. Schlieren, shadowgraphy and other similar optical flow-visualization techniques were brought to the fore-front of 20th century experimental physics and engineering by the work of Hubert Schardin (Schardin H. , 1934), (Schardin H. , 1970). There have been many books and papers on schlieren techniques, but their complete and appreciable treatments are provided in book by G.S. Settles (Settles, 2001). The theoretical foundation on schlieren and shadowgraphy techniques and the practical guidance on setting up a z-type schlieren technique, provided on (Settles, 2001) were followed during this research work. Along with the works by Hubert Schardin and Gary Settles, the current research work also borrows from works from many scientists, research and graduate students, some notable ones being (Mitchell, Honnery, & Soria, 2007), (Schmidt, 2015), (Nordberg, 2015), (Ranabhat, 2022), and (Gautam, Budhathoki, & Sitoula, 2023).

## 3.5 Experimental setup of a z-type schlieren imaging technique

The formation of well-illuminated and uniform monochromatic image in the cutoff plane and thus on the camera depends on the careful experimental setup of the schlieren technique. This includes the overall procedure starting from the location where the schlieren setup would be placed to the details like choice of the mirrors, light source, cutoff-type, and camera. The setup of a z-type schlieren imaging system includes several steps to be carefully examined, some of which are mentioned below.

### 3.5.1 Nature of the schlieren setup

In this study, considering from the point of view of generality, economy, and performance, a z-type schlieren setup is preferred. With a mirror-based system, experience on the careful alignment of optical equipment and handling of off-axis aberrations would be gained. For a research student learning the art and craft of

schlieren technique, it provides an invaluable experience before using a larger 'professional' schlieren equipment. The z-type schlieren imaging system considered in this study consists of two parabolic telescope mirrors of diameter ($d$) 76 mm and focal length ($f$) 400 mm. The orientation and placement of remaining optical equipment is based upon those two parameters of the mirror.

### 3.5.2 Setup configuration

The setup base is usually a wooden ply or table or workbench big enough to accommodate the schlieren system (Settles, 2001). Taking this into consideration, a 90 cm × 90 cm metal frame with four supporting legs was fabricated, upon which a wooden ply is rested. The remaining optical equipment including mirrors, cut-off, and camera remains on the wooden ply. The minimum distance between the schlieren mirrors should be $2\,f = 2 \times 400$ mm $= 800$ mm. The region near the periphery of the midpoint of the two schlieren mirrors is the test area. The completion of setting up the base for the z-type schlieren system is then followed with finding the room to set it up. It is not mandatory but better if the room is dark and free from ventilations because it eliminates any stray light or air that might affect the experiment. The schlieren setup was placed in the dark-room dedicated for flow visualization purpose in the IIEC, Pulchowk Campus as it meets with the criteria mentioned for appropriate room for setting up a schlieren system.

### 3.5.3 Optical Equipment Alignment

After the completion of setup configuration of z-type schlieren system, a reliable height is considered above the table base. This is the imaginary plane where the center point of all the optical components of the schlieren setup, namely the mirrors and camera would be present. This height was chosen as 163 mm. The setup would be affected by vertical misalignments if this height is thwarted by any means. This would then be followed by alignment of the illuminator (coherent point-light source setup). A piece of white A4 paper with a 76 mm circle drawn on it (equal to the diameter of the schlieren mirror) is taken and it is placed in front of the first schlieren mirror. The illuminator source which in this study is a light source stand, is rotated and it is set to a position where the illumination obtained in the A4 paper is uniform and just fills the 76 mm diameter circle irrespective of its distance from the first schlieren mirror. The circular

35

illuminated beam from first schlieren mirror is then directed towards the second schlieren mirror which is kept at minimum of 800 mm for this setup, by adjusting the tilt and rotation control of the first mirror. The midpoint of the line (joined by a marker or a measuring tape) joining the two mirrors is marked and test-region is maintained near its periphery during the experimental flow visualization studies. The second mirror is now rotated (approximately as the first mirror) to form a focused image, which could be found with the aid of a white paper as screen. The resulting point source image formed by the second schlieren mirror should be sharp. The cutoff (knife-edge) is then set up at this point either vertically or horizontally, cutting off certain portion of the point source image, depending upon the phenomenon to visualize.

The camera is placed beyond the knife-edge and the knife-edge is then run slowly into the focused point of the source image. While bringing the knife-edge, if the image in the recording plane (white screen, camera) darkens from just one side, that side is noted down. If that side happens to be the same side as the knife-edge movement into the source image, the axial distance of the knife-edge from the second-schlieren mirror is increased and vice-versa. The knife-edge is deemed to be in correct position when the image in the recording plane darkens uniformly when sliding the knife-edge into the focused beam from the second schlieren mirror. These images corresponding to the position of the knife-edge is shown in Figure 3.2. Once the knife-edge position is set, the amount of cut-off is decided depending on the sensitivity required for the type of flow-phenomena one wishes to visualize.

`                    (a)                              (b)                              (c)

Figure 3.2: Effect on the schlieren image captured by camera due to knife-edge displacement [knife edge position: vertical, knife-edge movement into the focal-point: from left to right] (a) knife-edge is close to the mirror, (b) correct adjustment, (c) knife-edge is far from the mirror

### 3.5.4 Troubleshooting the schlieren setup

After the completing of setting up the z-type schlieren setup, troubleshooting is done in-case any off-axis aberrations or errors are present in the system. To check if the astigmatism is dominant in the fabricated schlieren system, its severity is checked using the Eq. 2.16 or Eq. 2.17, and it is minimized by choosing a parabolic mirror of greater $f$/number or reducing the tilt angle.

### 3.5.5 Testing the schlieren setup

Upon following the fore-mentioned procedures, the objective of setting up a portable and compact z-type schlieren imaging allowing for easier fluid-flow measurements and experimentation would have come into fruition. There are multitude of ways to test the setup at this point. The most notable ones include the visualization of thermal plumes from a burning candle and hot air rising from the soldering iron rod. The schlieren images are then analyzed to provide an insight on the setup's status quo. At this stage, some of the schlieren images captured are shown in Figure 3.3 and 3.4.

Figure 3.3: Uniform laminar cylindrical flow of a candle plume and its transition to disturbed flow



Figure 3.4: Heated air near the periphery of a soldering iron rod rising upwards

### 3.5.6 Visualization of different fluid-flow phenomena

Once the images from the z-type schlieren setup is considered sensitive enough based on the visualization of thermal plume from a burning candle or hot air rising from the soldering iron, it is used to visualize other fluid-flow phenomena. In this study, it would be used to visualize the Non-Buoyant Plumes emanating from an ice onto the lukewarm water, Under-expanded jet pattern produced by a CD-nozzle, and Flow-deflection of an under-expanded jet produced by a CD-nozzle.

## 3.6 Findings and Reporting

The findings of the research study will be documented systematically and will be submitted to the Department as the thesis report as per the requirements of the Department of Mechanical and Aerospace Engineering.

## 3.7 Conclusions and Recommendations

Upon the completion of the research work, conclusions on the visualized flow-phenomena would be documented and recommendations will be provided for the better utilization of the z-type schlieren setup. The recommendations would be drawn from the learning experiences the author had from the time of fabrication of the setup to the final test performed utilizing the setup. Amid the conclusions and recommendations drawn, the research work will also attempt in serving its purpose towards the continual development of optical flow visualization technique in IOE, Pulchowk Campus.

## CHAPTER FOUR: DESIGN PROCEDURES

### 4.1 Numerical Calculation

### 4.1.1 Distance between the mirrors

The mirror chosen for the z-type schlieren setup is a parabolic mirror of a reflecting type telescope with diameter of 76 mm and focal length of 400 mm. The minimum distance between the two mirrors should be at least $2f$ (Settles, 2001), i.e., 800 mm. Since there is no restriction in maintaining longer distances, the distance is kept 1000 mm for providing adequate space for the test area.

### 4.1.2 Mirror tilt angle

If one were to assume that the extreme illuminating ray from the coherent point light source happens to coincide with the foci of the schlieren mirrors, the angle between the incoming and outgoing beam is given by trigonometric relation:

$$\tan(2\theta) = \frac{d}{2f} \qquad\qquad \text{Eq. 4.1}$$
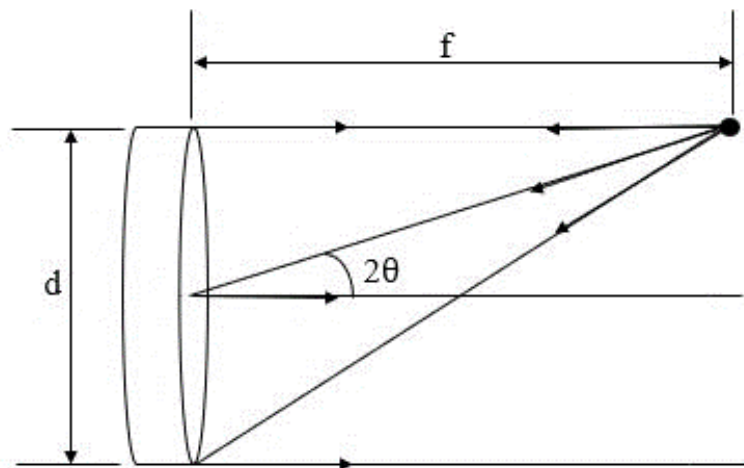


Figure 4.1: Condition where the extreme illuminating ray from point light source coincides with the foci of the schlieren mirror

Substituting the values of diameter ($d$) and focal length($f$) of the mirror in Eq. 4.1, the angle between the incoming and outgoing beam is obtained to be 5.42⁰. This is impractical situation and also unnecessary. As stated in (Settles, 2001), there should be enough space to work with while performing flow-visualization tests while at the same time maintaining the beam angles optimally small. The value was increased to 15⁰ allowing for a better working space without the interference of the point light source in the test area. This yields the mirror tilt angle (which is half of the angle between the incoming and outgoing beam) to be 7.5⁰.

### 4.1.3 Astigmatism severity

Since the mirror tilt angle is 7.5⁰, it is not plausible to use the small angle approximation formula of Eq. 2.17. Instead, using the formula stated in Eq. 2.16, the astigmatism severity is obtained to be:

$$\Delta f = 400 \text{ mm} \times \frac{\sin^2 7.5}{\cos 7.5}$$

$$\Delta f = 6.874 \text{ mm}$$

Since the distance between the sagittal and tangential focus represented here by $\Delta f$ is smaller than the focal length of the mirror by a factor of around 60, astigmatism would not be much of a problem for the fabricated schlieren system.

### 4.2 Experiment Setup and Equipment

The z-type schlieren setup fabricated in this study consists of different optical equipment and component, some of which are described in this section. Figure 4.2 shows the CAD design of the experimental setup configuration, while Figure 4.3 shows the fabricated z-type schlieren setup. The major components of the setup are two mirrors, a point light source, a cut-off, and a platform/ base upon which the fore-mentioned components rest on.
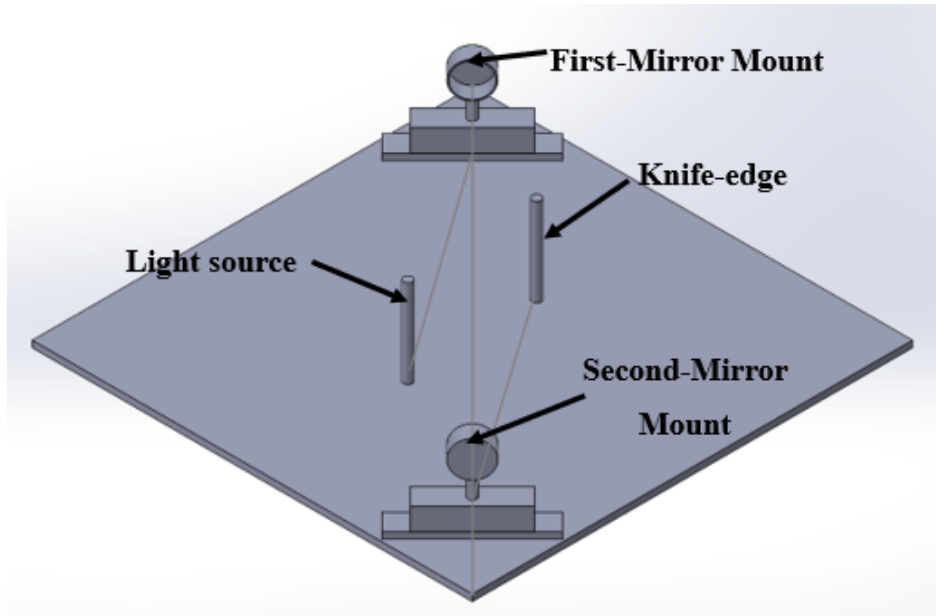
Figure 4.2: CAD model of the z-type schlieren setup
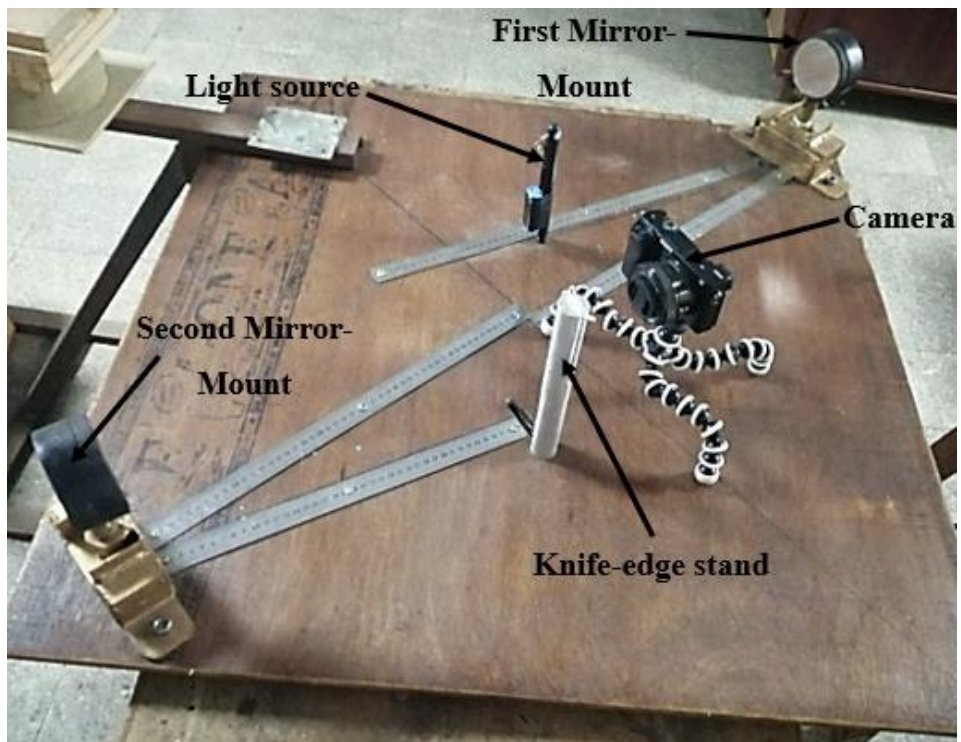


Figure 4.3: Fabricated z-type schlieren setup

### 4.2.1 Mirrors

Two parabolic mirrors of a reflecting type telescope are used in the setup. The diameter of the mirror is 76 mm and its focal length is 400 mm which gives a $f$-number of approximately $f/5$. The mirrors are placed inside adjustable heavy mirror holders/ mounts, which makes for easy adjustments in the angular position of the mirror. The mirror is coated with aluminum as a protective film. The mirrors used in this setup is shown in Figure 4.4.



Figure 4.4: Parabolic mirrors of a reflecting type telescope

### 4.2.2 Camera

The camera predominantly used in the experimental flow visualization is a Sony ZV-E10 Mirrorless Camera. It is a very small and light interchangeable lens mirrorless camera with an excellent 24 MP Exmor CMOS sensor. The picture of the camera along with a camera tripod stand used in the schlieren setup is shown in Figure 4.5.

Figure 4.5: Camera and tripod stand used in the schlieren setup

Besides the Sony ZV-E10 Mirrorless Camera, a high-speed camera 'Chronos 2.1-HD' was used to observe the development of under-expanded jet from the CD-nozzle and Non-Buoyant Plumes in water. The detailed specification of the camera could be found in (Chronos 2.1-HD Starter Bundle, 2023). The specifications like frame-rate, and resolution of images captured by the high-speed camera during the visualization of fluid-flow phenomena are specified in the corresponding result and discussions section. The picture of the high-speed camera and its associated devices are shown in Figure 4.6.



(a)

(b)

(c)

(d)

Figure 4.6: Chronos 2.1-HD High speed camera (a) Camera body, (b) Sigma 24-70mm lens, (c) Trigger switch cable, (d) Camera body-lens setup

### 4.2.3 Light Source

As a small bright light source for schlieren and shadowgraphy, a 5 mm LED is an excellent and inexpensive source (Settles & Hargather, 2017). For the experimental setup, a 5 mm white LED is used. The specifications of the LED light are mentioned below:

- Wavelength = 365-450 nanometer
- Maximum forward current = 30 milliamps
- Forward Voltage = 3.4 V type, 3.6 V maximum @ 20 milliamps

A 9V Hi-Watt battery is used to illuminate the LED light. To avoid damaging the LED light, a resistor is used. The resistance of the resistor is calculated as:

$$\text{Resisitor voltage} = \text{Input voltage} - \text{LED forward voltage}$$

$$= 9\,\text{V} - 3.4\,\text{V} = 5.6\,\text{V}$$

Following Ohm's law:

$$\text{Resistance} = \frac{\text{Voltage}}{\text{Current}}$$

$$= \frac{5.6\,\text{V}}{0.02\,\text{A}} = 280\,\text{Ohms}$$

The pictures of the light source setup are shown in Figure 4.7.



Figure 4.7: Light source setup components

### 4.2.4 Setup for visualizing Under-expanded Jet

The experimental setup designed and fabricated by (Gautam, Budhathoki, & Sitoula, 2023) present in the IIEC, Pulchowk Campus was combined with the fabricated z-type schlieren setup as shown in Figure 4.8. The under-expanded flow from the CD-nozzle was visualized and captured using this setup. The setup consists of a nozzle-stand, a reciprocating air compressor as a pressure source, a reservoir, polyurethane pipe connecting reservoir to the nozzle, a valve in between the air compressor and reservoir, and multiple lock valves. The detail description of the experimental setup is present in (Gautam, Budhathoki, & Sitoula, 2023).
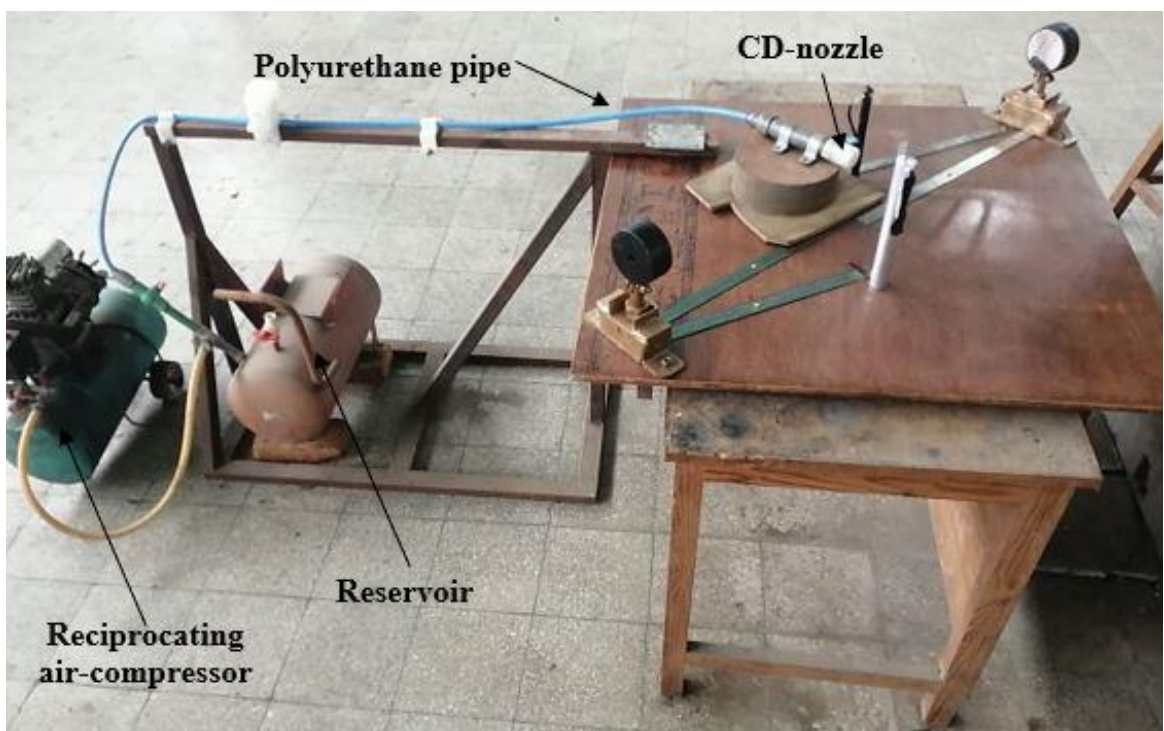


Figure 4.8: Experimental setup for visualizing Under-expanded jet from a CD-nozzle

### 4.2.5 Setup for visualizing Negatively-Buoyant Plumes

The cold dense water descending from an ice-cube into a lukewarm water ($\sim 60°C$) was chosen as the phenomena to study Negatively-Buoyant Plumes. A small glass tank was used to contain lukewarm water and a cube of ice was placed above the free surface of the water to produce the Negatively-Buoyant Plumes of cold dense water cascading into the lukewarm water. The visualization was captured by Chronos 2.1 HD High

Speed Camera. The entire setup including the z-type schlieren imaging is shown in Figure 4.9.
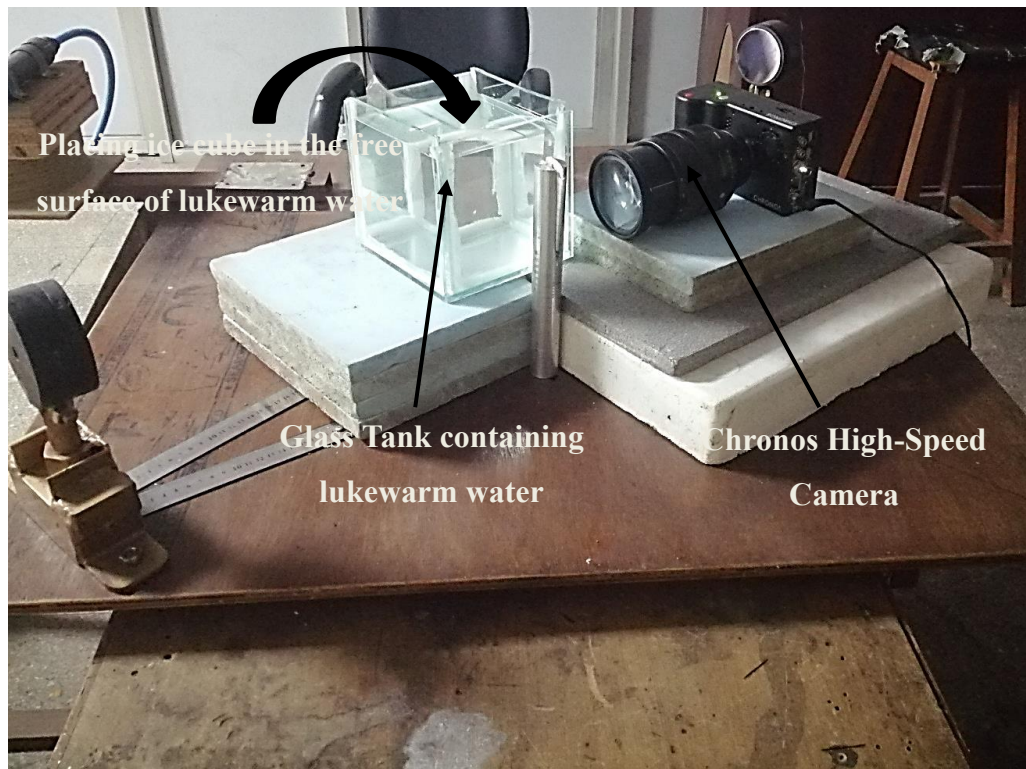


Figure 4.9: Experimental setup for visualizing Negatively Buoyant Plumes in Water

## 4.3 Experimental Alignment

As mentioned before in Experimental setup of a z-type schlieren imaging technique of Chapter Three, Methodology, in order to achieve a clear image in the recording plane, the schlieren system needs to be properly and carefully aligned. First of all, the reflecting telescope mirrors (parabolic mirrors) are placed on the opposite sides of the test section, maintaining a distance of 1000 mm between each other. During the placement, the mirrors are aligned carefully maintaining a tilt angle of around 7.5⁰ so that majority of the collimated light beam incident on the first mirror is reflected onto the second mirror. These procedures are shown in Figures 4.10.

Figure 4.10: Adjusting the set-up for light source

The test section is maintained at the mid-distance of the two schlieren mirrors. The point light source (LED light) is kept in an optical stand at a distance of focal length ($f$), i.e., 400 mm from the first schlieren mirror and height of 163 mm from the table-base. The LED light is turned on. A piece of white A4 paper is used as screen to then pin point the focal point of the second schlieren mirror, located approximately at 400 mm. In other words, it is the location where the diameter of the source image formed due to the convergence of the collimated beam by the second schlieren mirror nearly equals the diameter of the point light source (LED light). The knife-edge is carefully placed at this location to cut-off certain portion of the source image. The knife-edge was adjusted multiple times to be sure that it was at the exact focal point of the second schlieren mirror. These procedures are shown in Figure 4.11.

(a)                     (b)

Figure 4.11: (a) Locating the position where source-image diameter nearly equals the point-source diameter, (b) Positioning the knife-edge to cut-off certain portion of the source image

The knife-edge cut-off position was confirmed by placing a burning candle in the test section and observing its image in the camera with different amount of knife-edge cutoff. It is observed from Figure 4.12 that from the stand-point of experiments to be conducted in this research study, around 50 % cutoff is ideal because the image is uniformly illuminated and the thermal plume of the candle was also clearly visible.

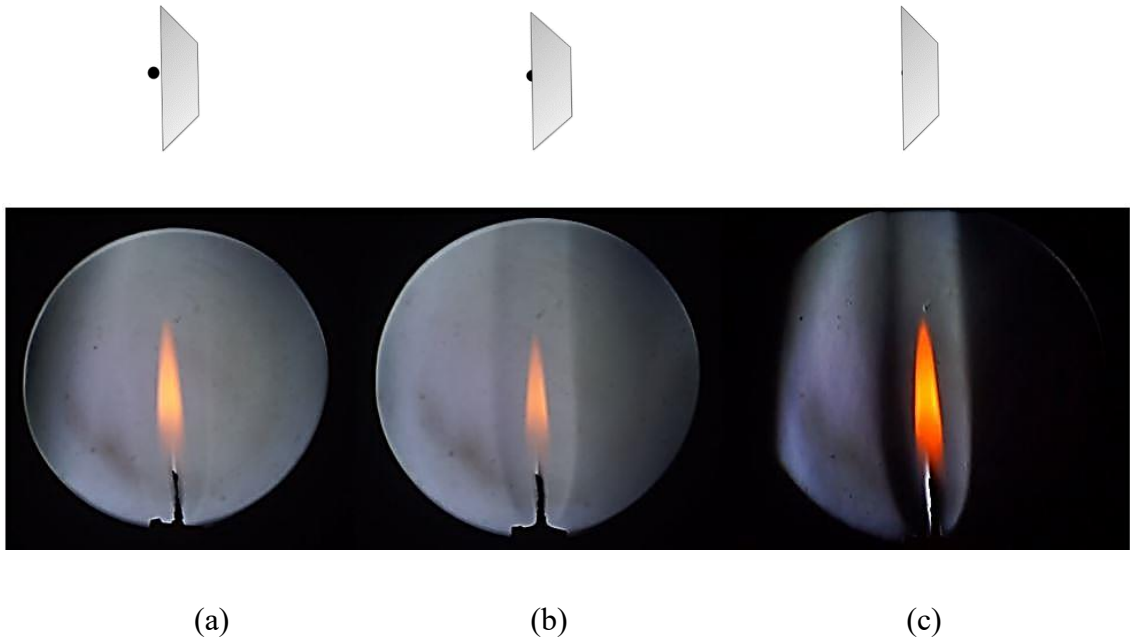(a)                  (b)                  (c)

Figure 4.12: Schlieren photographs of thermal plume of a burning candle. The amount of knife-edge cutoff of the LED source image is (a) 0%, (b) around 50 %, (c) almost 100 % cutoff. Placement of knife-edge: Vertical

**CHAPTER FIVE: NUMERICAL SIMULATION OF UNDER-EXPANDED JET**

This chapter sheds light on the numerical simulation of the under-expanded jet from the CD-nozzle. The purpose of performing numerical simulation is to have a simulated visual representation of the flow and to compare the results (both qualitatively and quantitatively) with the results obtained from experimental study.

**5.1 Geometry Creation**

The numerical simulation was carried out in ANSYS Fluent. The flow-domain used for the study with dimensions is shown in Figure 5.1. Only the upper half of the flow-domain was simulated owing to the symmetry of the problem.
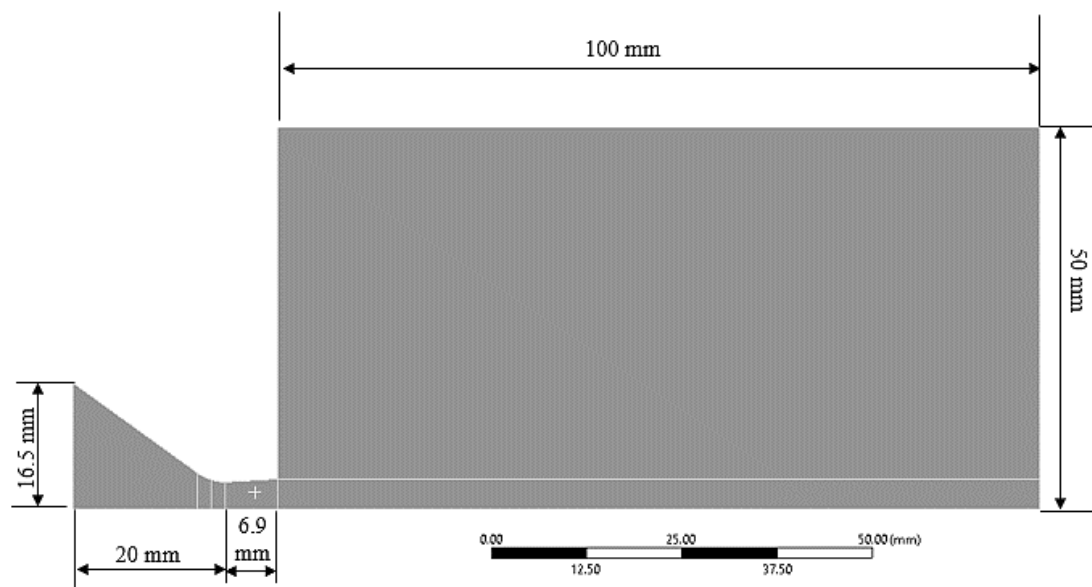


Figure 5.1: Geometry of the flow-domain used in the simulation study

**5.2 Mesh Creation**

The meshing was performed in ANSYS as well. Because of the simple geometry, the mesh used for the study was structured quadrilateral mesh. Structured meshes offer simplicity and efficiency, and at the same time consumes less memory than an unstructured mesh with the same number of elements. This is because in a structured mesh array storage can define neighbor connectivity implicitly (Sack & Urrutia, 2000). To aid in the process of meshing, the flow-domain was divided into multiple small sub-

domains. A grid/mesh-independence study was then carried out. The parameter chosen for the mesh independence study is the average Mach-number at the exit plane of the CD-nozzle. The details of the mesh independence study are shown in Table 5.1.

Table 5.1: Mesh Independence Study

| Meshes | Mesh details | Average Mach Number at the exit plane of the CD-Nozzle |
|---|---|---|
| I | Number of Nodes: 98082 | 1.385791 |
| | Number of Elements: 97210 | |
| II | Number of Nodes: 142791 | 1.402271 |
| | Number of Elements: 141860 | |
| III | Number of Nodes: 209662 | 1.402151 |
| | Number of Elements: 208377 | |

It was observed that the result for the average Mach number at the exit plane of the CD-nozzle was independent of the mesh/grid for the number of nodes higher than 142,791 and number of elements higher than 141,860. So, Mesh-II was chosen for the simulation study. The finalized mesh in the flow-domain that was used for the study is shown in Figure 5.2. The zoomed mesh for region-1, 2, and 3 are shown in Figure 5.3.

Region-3

Region-1

Region-2

0.00          30.00          60.00 (mm)
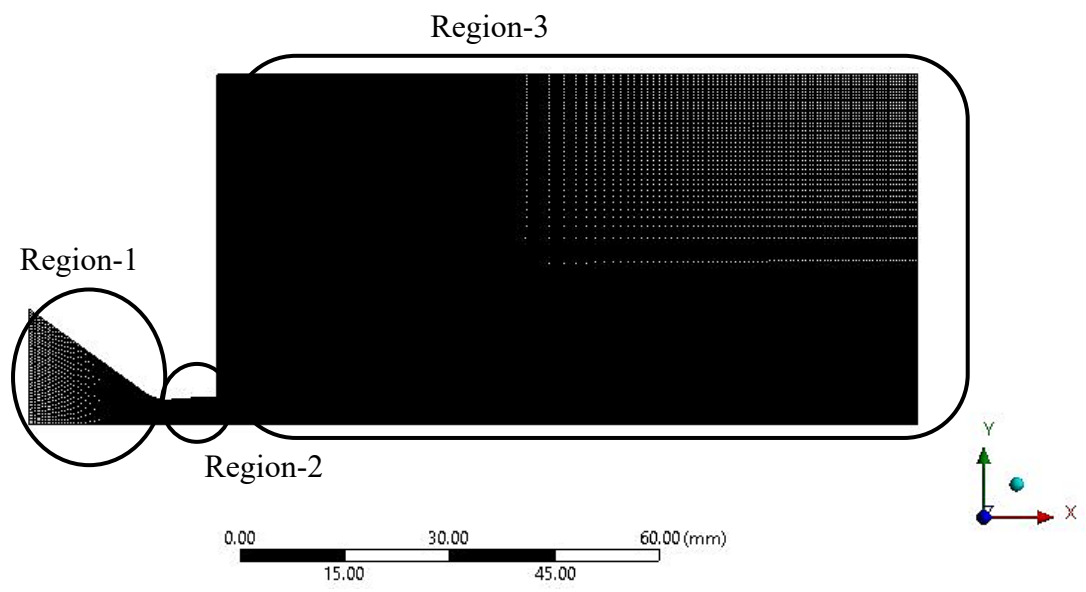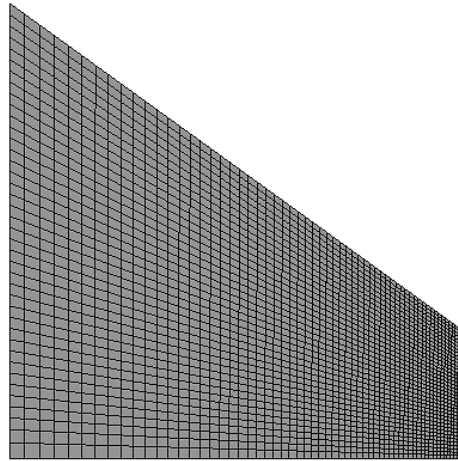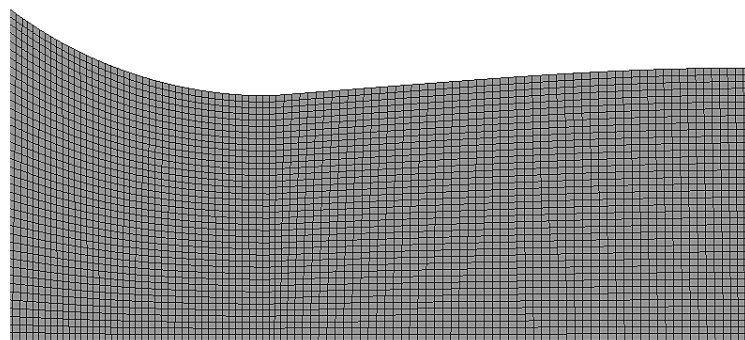      15.00          45.00

Figure 5.2: Final Mesh used for the simulation study



(a)



(b)
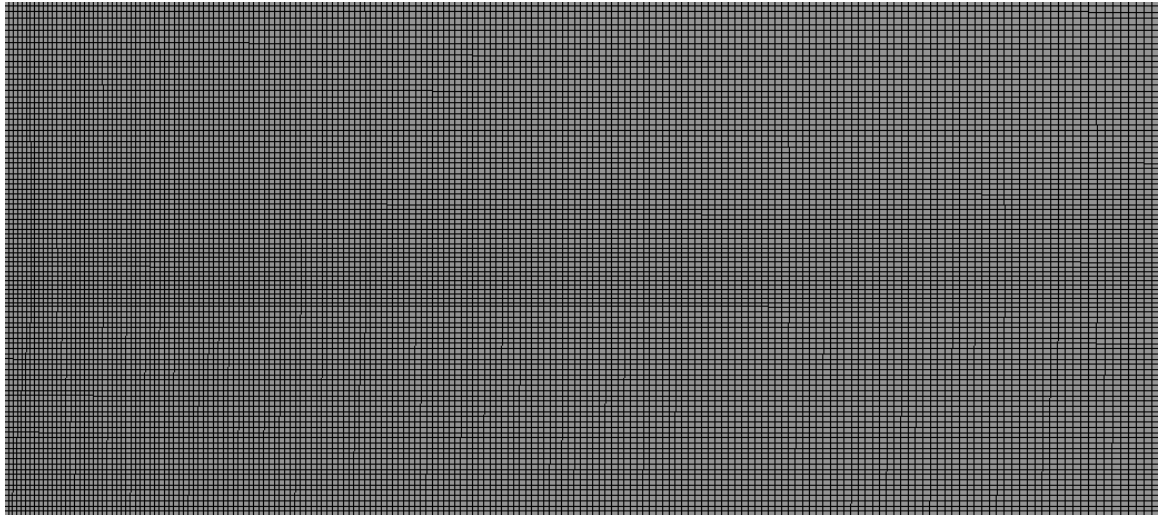
(c)

Figure 5.3: Zoomed mesh of (a) Region-1 (converging section), (b) Region-2 (curved converging section and diverging section), and (c) Region-3 (ambient environment)

## 5.3 Mesh Quality Evaluation

Meshing is one of the most important steps of any numerical simulation. Owing to its importance, it is necessary to ensure the mesh quality for fast and accurate analysis. The mesh metrics for the mesh shown in Figure 5.2 and 5.3 is shown in Table 5.2.

Table 5.2: Mesh Metrics

| Mesh Metrics | Minimum | Average | Maximum |
|---|---|---|---|
| Skewness | $1.2743 \times 10^{-6}$ | $5.4012 \times 10^{-3}$ | 0.3982 |
| Aspect ratio | 1 | 1.8561 | 5.0112 |
| Orthogonal Quality | 0.81418 | 0.99852 | 1 |

### 5.3.1 Skewness

Skewness gives an insight on how close to ideal (i.e., equilateral or equiangular) a face or cell is. Going by its definition, a skewness value near 0 would refer to an ideal mesh cell and a value near 1 would refer to a degenerate mesh cell. Degenerate cells, also called slivers, are characterized by nodes that are nearly coplanar (collinear in 2D) (ANSYS, Reporting Mesh Statistics, 2008). The element skewness values for all the mesh elements used in this study is shown in Figure 5.4.
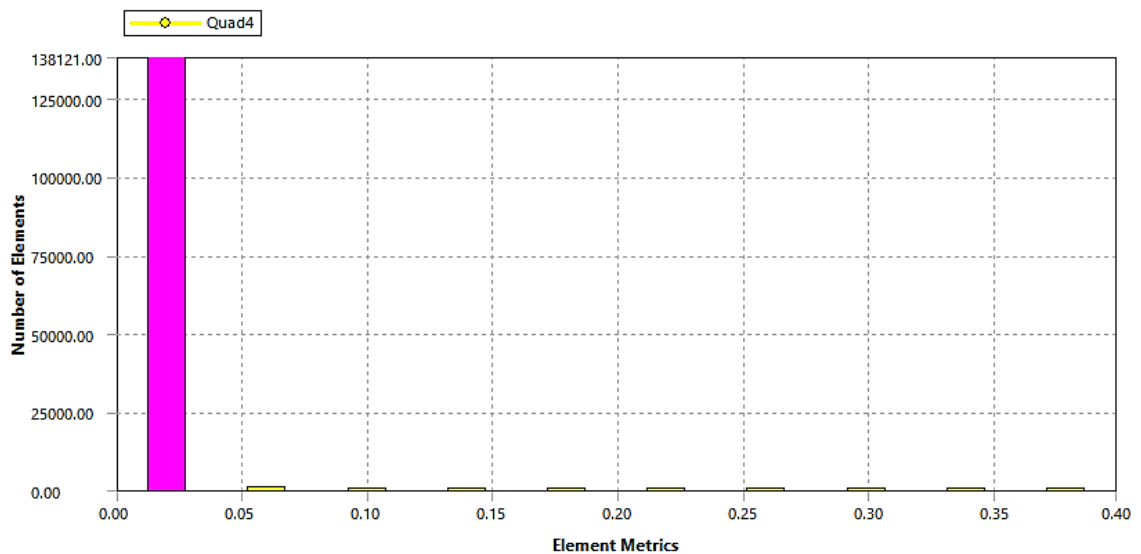


Figure 5.4: Mesh-element skewness

### 5.3.2 Aspect Ratio

The aspect ratio of a mesh is the ratio of its longest edge's length to its shortest edge's length. For an equilateral face or cell (e.g., an equilateral triangle or a square), the aspect ratio will be 1. For less regularly-shaped mesh-faces the value will be greater than 1 (ANSYS, Reporting Mesh Statistics, 2008). For 2D quadrilateral cells (like the ones used in this study), it is important to check the aspect ratio in addition to skewness because there could be large jump between two mesh faces maintaining the integrity in their equilateral or equiangular face. In such cases, skewness alone would not be a good mesh metric to judge the resulting mesh. The aspect ratio of mesh elements used for this study is shown in Figure 5.5.
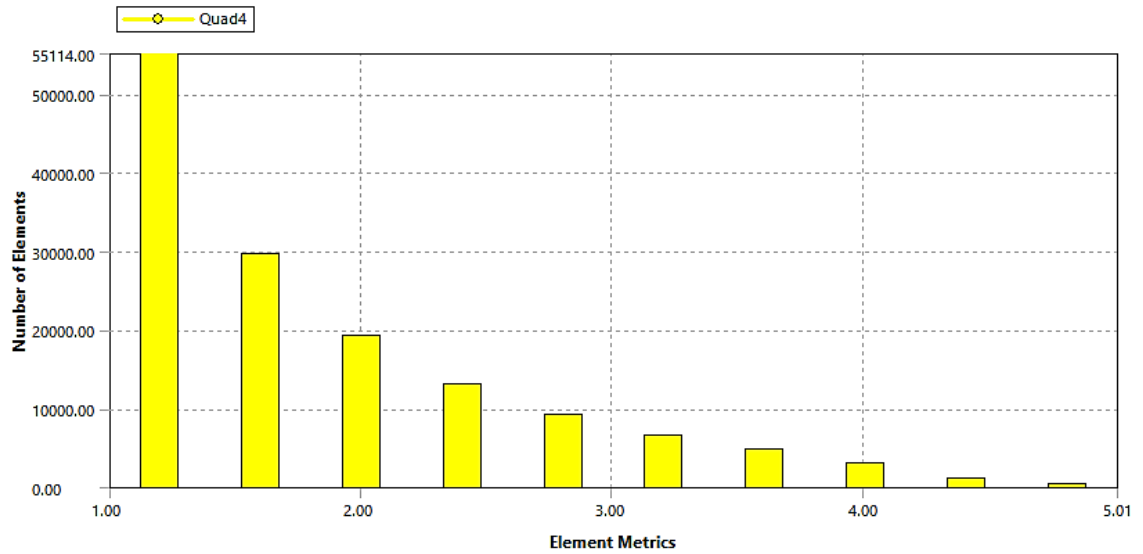
Figure 5.5: Mesh-element aspect ratio

### 5.3.3 Orthogonal Quality

It is another important indicator of mesh quality. It is computed using the vector from centroid of the cell to the centroid of each cell's faces, face area vector, and vector from centroid to the cell to the centroid of adjacent cells (ANSYS, ANSYS FLUENT User's Guide, 2010). The value of 0 indicates a mesh cell or face of low quality, whereas a value close to 1 indicates a mesh cell or face of high quality. The orthogonal quality of the mesh used in this study is shown in Figure 5.6.
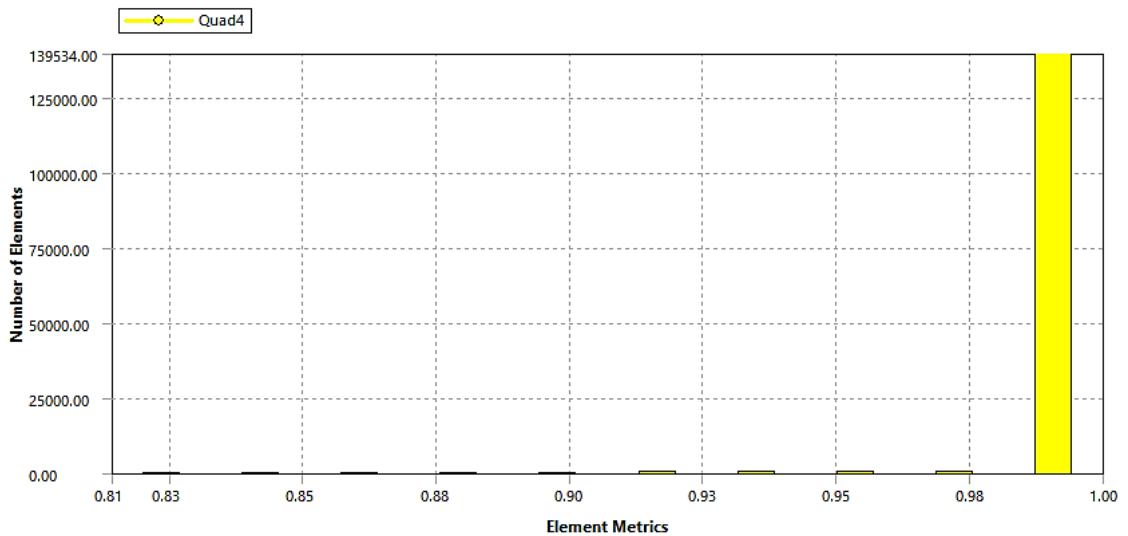


Figure 5.6: Mesh-element orthogonal quality

56

## 5.4 Fluid-Domain Setup

In ANSYS Fluent, two solver technologies, namely pressure-based and density-based solver are available. In retrospect, the density-based solver was designed for high-speed compressible flows, while pressure-based solver was designed for incompressible and mildly compressible flows. So, density-based solver was chosen in this study. Similarly, the simulation study did not consider the effect of gravity and was proceeded with double precision solution strategy. Some of the important setup parameters related to the simulation are shown in Table 5.3 and the flow-domain after the implementation of boundary conditions is shown in Figure 5.7. Finally, to aid the process of convergence of the solution, solution steering option was selected before running the calculation. The flow type was selected as supersonic.

Table 5.3: Setup conditions implemented in the flow-domain

| | Type | Density based |
|---|---|---|
| **General** | Time | Steady |
| | Velocity Formulation | Absolute |
| | 2D-space | Planar |
| **Models** | Energy | ON |
| | Viscous Model | k-epsilon (2-equation) realizable |
| **Material** | Fluid | Ideal gas |
| | Specific Heat | 1006.43 J/kg.k |
| | Thermal Conductivity | 0.0242 W/m.K |

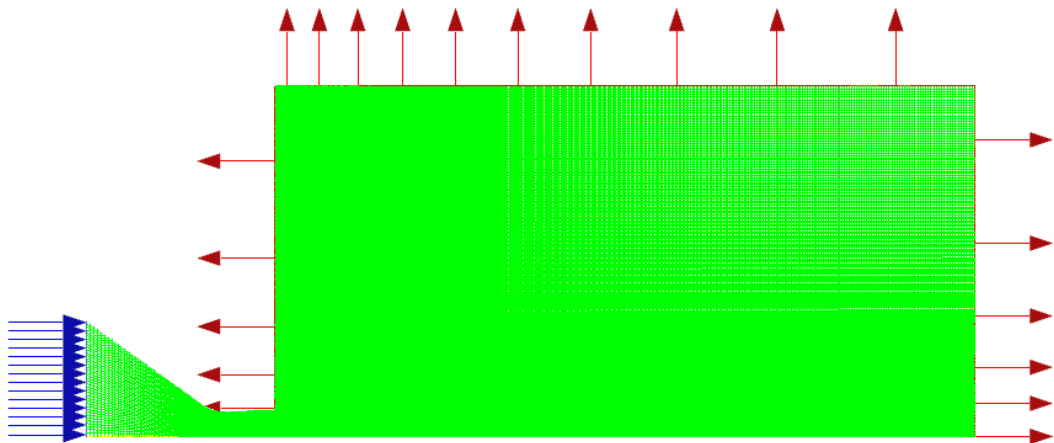| | | |
|---|---|---|
| | Viscosity | Sutherland (Three Coefficient Method) |
| **Boundary Conditions** | Pressure Inlet | Gauge Total Pressure: 506625-709275 Pascal<br><br>Total Temperature: 300K |
| | Pressure Outlet | Gauge Pressure: 101325 Pascal<br><br>Backflow Total Temperature: 215.517 K |
| | Center-line | symmetry |
| | Wall | Stationary wall<br><br>No slip condition |
| **Solution Controls** | Courant Number | 0.9 |



Figure 5.7: Boundary conditions implemented in the flow-domain

## 5.5 Results from simulation

The flow-domain considered in this study only represents the half-portion of the actual flow. The simulation was run for the half-portion and upon completion, the results for lower-half portion of the flow domain was just mirrored owing to the symmetry of the flow. The under-expanded jet emerging out of the exit plane of the CD-nozzle for NPR of 5, 5.5, 6, 6.5, and 7 are shown in Figure 5.8.



(a)

(b)



(c)

60
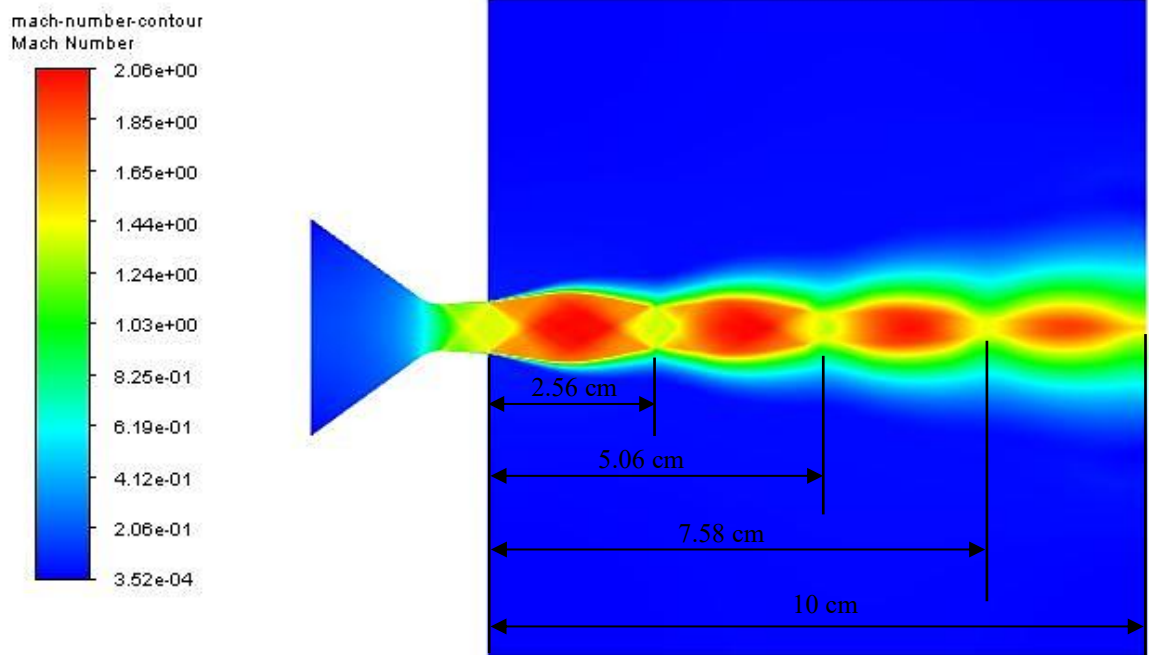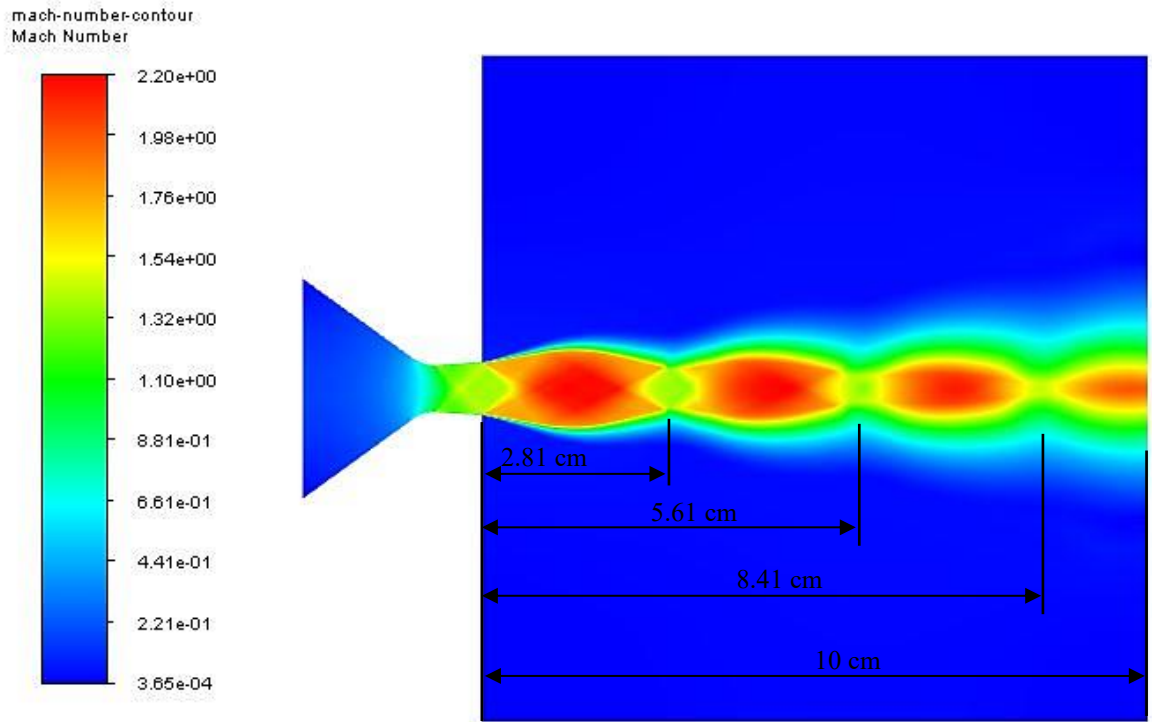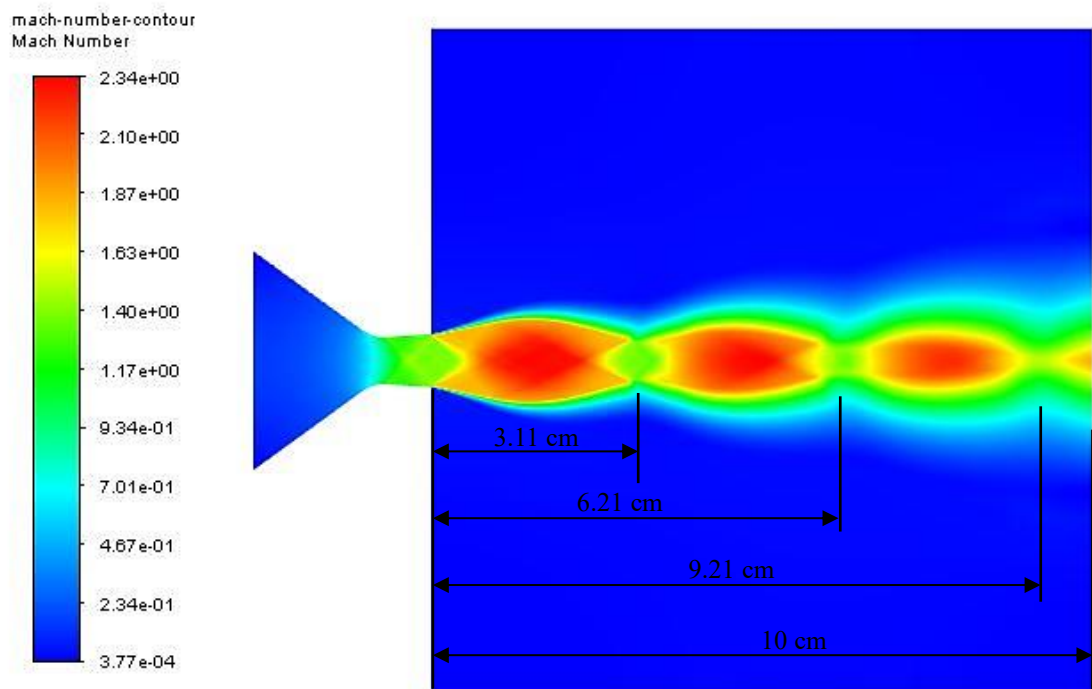
(d)



(e)

Figure 5.8: Under-expanded flow from a CD-nozzle simulated for NPR of (a) 5, (b) 5.5, (c) 6, (d) 6.5, and (e) 7

The under-expanded jet emerging out of the nozzle-exit plane initially billow outwards. The flow is then observed to turn 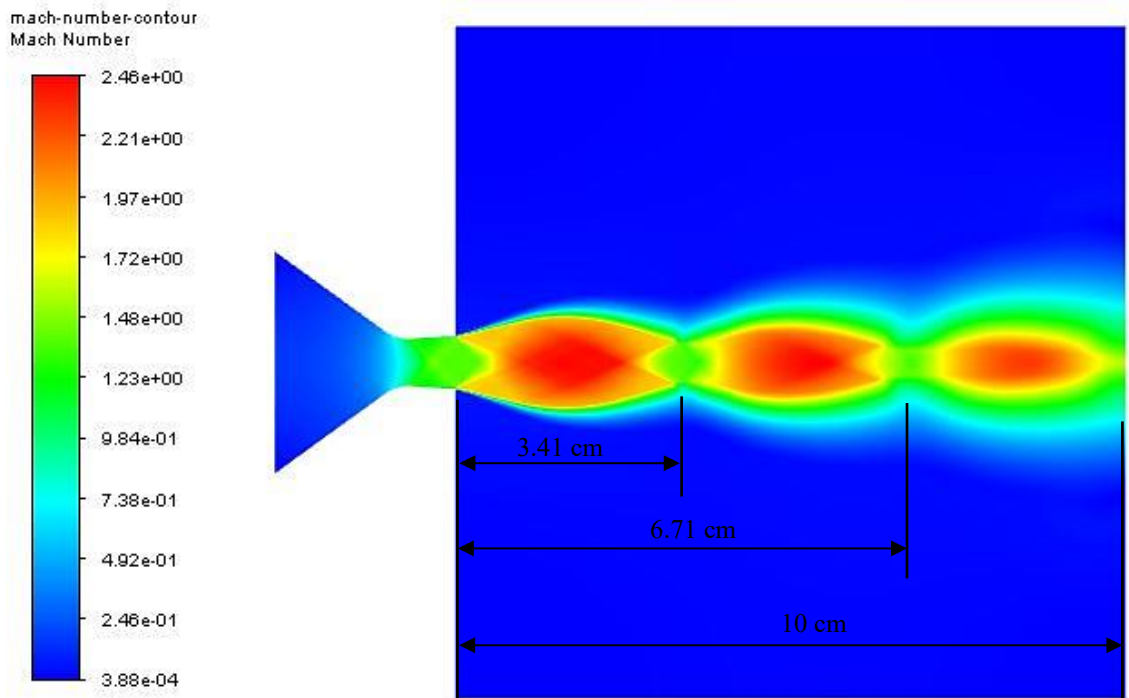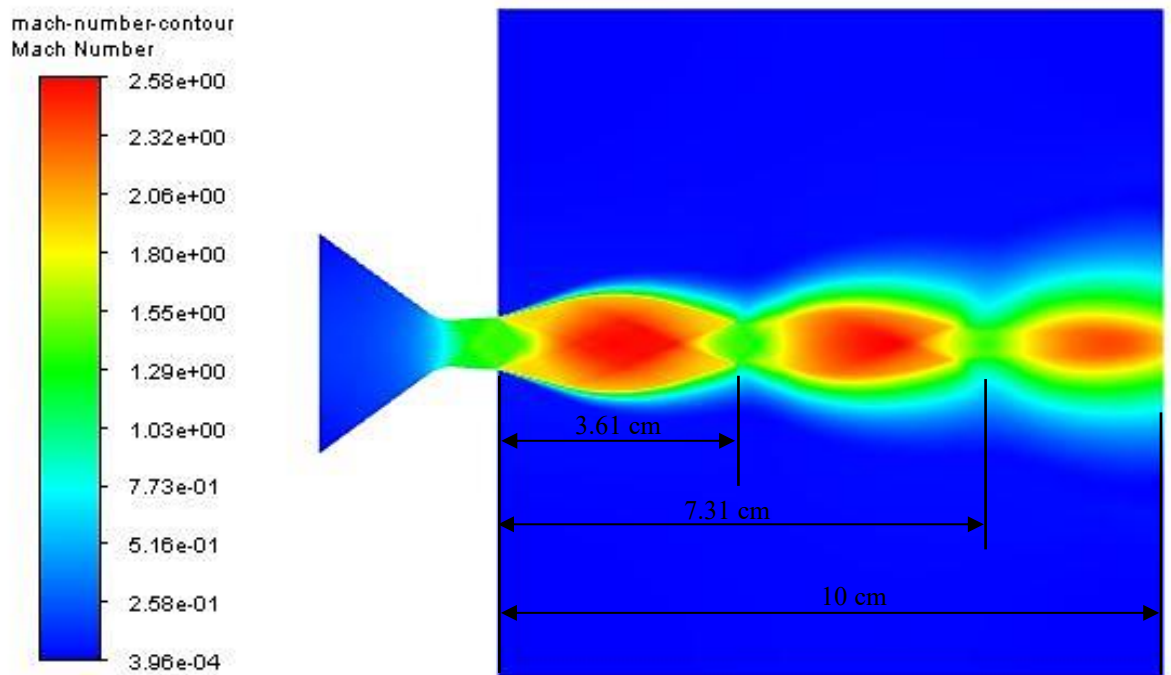inwards which is accomplished through a series of expansion waves which reflect off the free jet boundary. These expansion waves and the resulting formation of oblique shock waves were also observed in the simulation. The important distinction of the under-expanded flow is the formation of structures called 'shock-diamond' (also called Mach diamond). It is a complex flow field which is brought into sharp visual image due to abrupt changes in local density and pressure as the under-expanded jet passes through a series of standing shock waves and expansion fans (Norman & Winkler, 1985). These shock-diamond structures are also visible in the simulation results. An example showing the labelled simulation result for NPR 5.5 is shown in Figure 5.9.
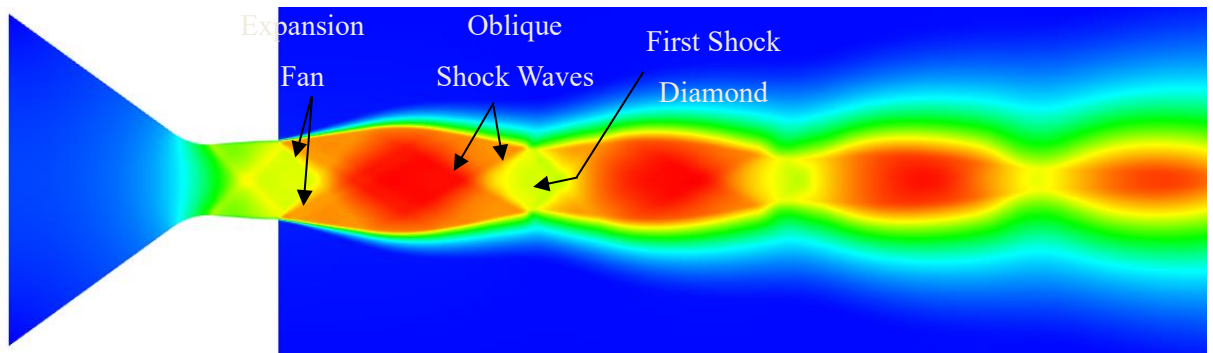


Figure 5.9: Shock diamond structure formation in an under-expanded jet for NPR 5.5

**CHAPTER SIX: RESULTS AND DISCUSSION**

This chapter includes the results obtained from the fabricated z-type schlieren imaging system. The schlieren images were captured using the Sony ZV-E10 Mirrorless Camera and Chronos 2.1-HD High Speed Camera. The phenomena of key interest were the Negatively-Buoyant Plumes in water, Under-Expanded Jet through a CD-nozzle, and Under-expanded flow deflection.

## 6.1 Negatively-Buoyant Plumes in Water

Using the setup (as detailed in Chapter Four, Section 4.2.5), the negatively buoyant plumes of dense cold-water cascading into the lukewarm water was observed. The images were captured by Chronos High-Speed Camera at 1000 fps and 1920×1080 pixels resolution. The temperature of the lukewarm water was measured with a mercury thermometer and found to be around 60°C. The ice once placed on the free surface of lukewarm water gets melted, forming a small layer of cold water on the underside of the ice cube. The cold water collects because of roughness present on the ice surface and perturbations present in the water. This cold layer of water which has formed is present above the less dense lukewarm water. The interface between these two layers is highly unstable and even the smallest of perturbations could result in the development of instability in the interface. The theoretical work on the development of such instability has been done, most prominently by the scientist Subrahmanyan Chandrasekhar in his famous book 'Hydrodynamic and Hydromagnetic Stability (Chandrasekhar, 1961)'. The instability first develops linearly wherein the development of instability is governed by the linearized dynamical equations. The instability then grows non-linearly which is influenced by the density ratio of the two-fluids (also called the Atwood Number). The Atwood Number ($A$) for this study is calculated to be:

$$A = \frac{\rho_H - \rho_L}{\rho_H + \rho_L} = 0.007893$$

where,

$\rho_H$: higher dense cold water from ice (0**⁰C**) = 999.82 kg/m$^3$

$\rho_L$: lighter dense lukewarm water (~60**⁰C**) = 984.16 kg/m$^3$

Density values taken from (Water Density Table, 2022).

Since, $A = 0.007893 < 1$, the lighter lukewarm water moves into the denser cold water which results in the formation of round topped bubbles with circular cross-section. This resulting structure of the flow is called the Rayleigh-Taylor Instability. Such instability occurs when an interface has formed between two layers of fluids of different densities when the lighter fluid beneath is pushing the denser fluid above it. This instability has a typical mushroom cap shaped spikes which is observed in the z-type schlieren imaging as shown in Figure 6.1.
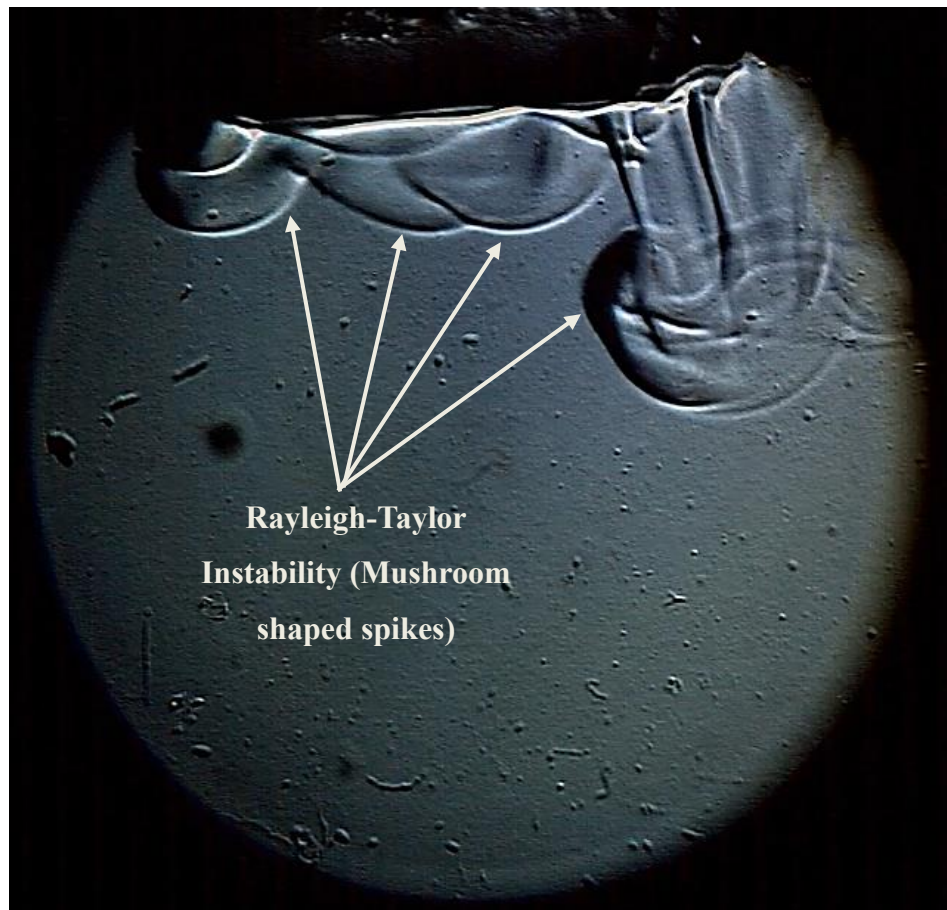


Figure 6.1: Rayleigh-Tayor Instability as observed in the Negatively Buoyant Plumes in water

As the Negative- Buoyant Plume cascade downwards, the mushroom shaped structure starts to curl back on itself. This is because of the velocity shear between the cold and the lukewarm water (i.e., fluids with varying densities). The plume has now encountered another instability called Kevin-Helmholtz Instability. These instabilities were also captured in the Negatively Buoyant Plumes from the z-type schlieren setup as shown in Figure 6.2. The time-lapse of the development of the Negatively Buoyant Plume is shown in Figure 6.3.
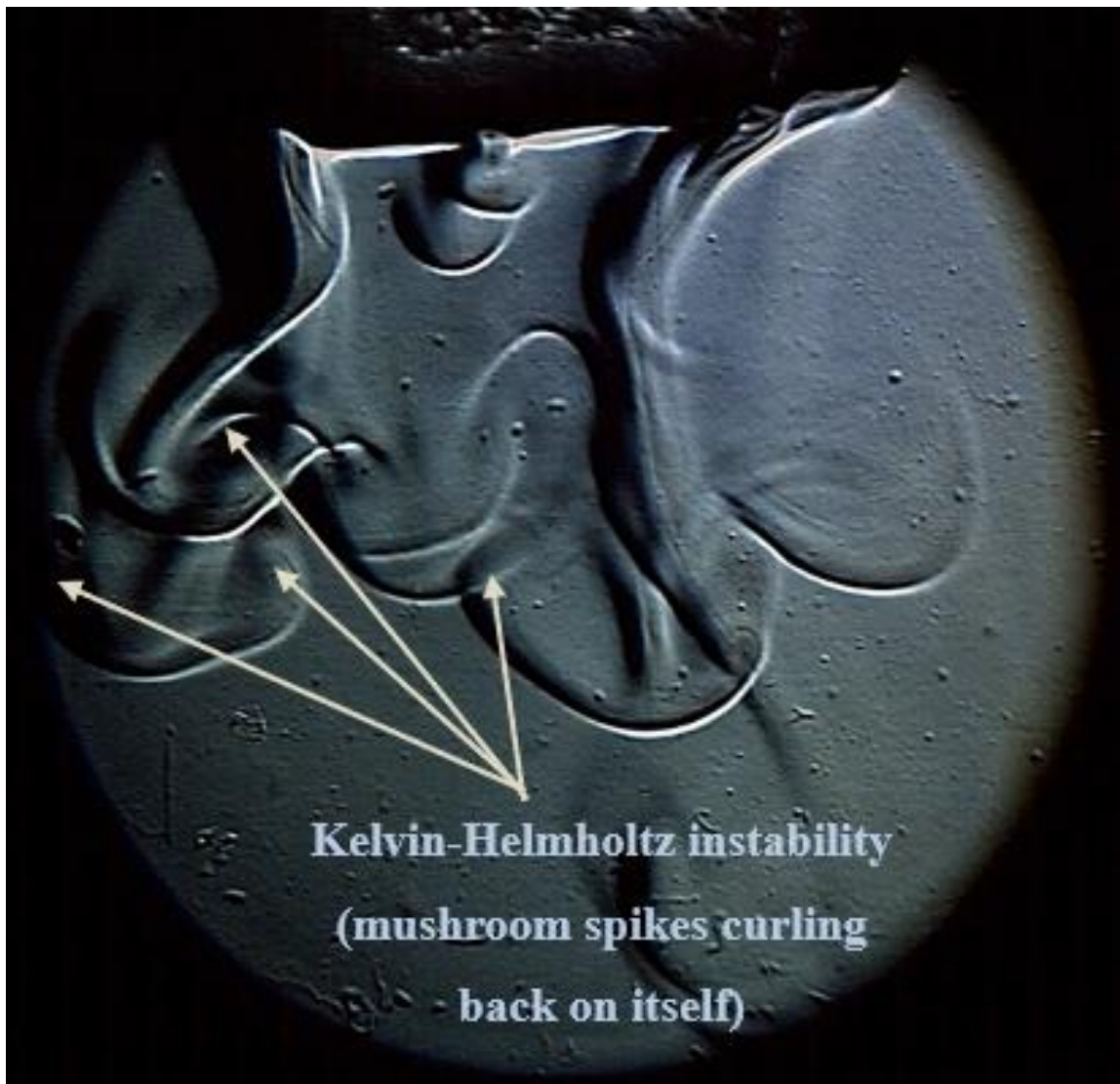
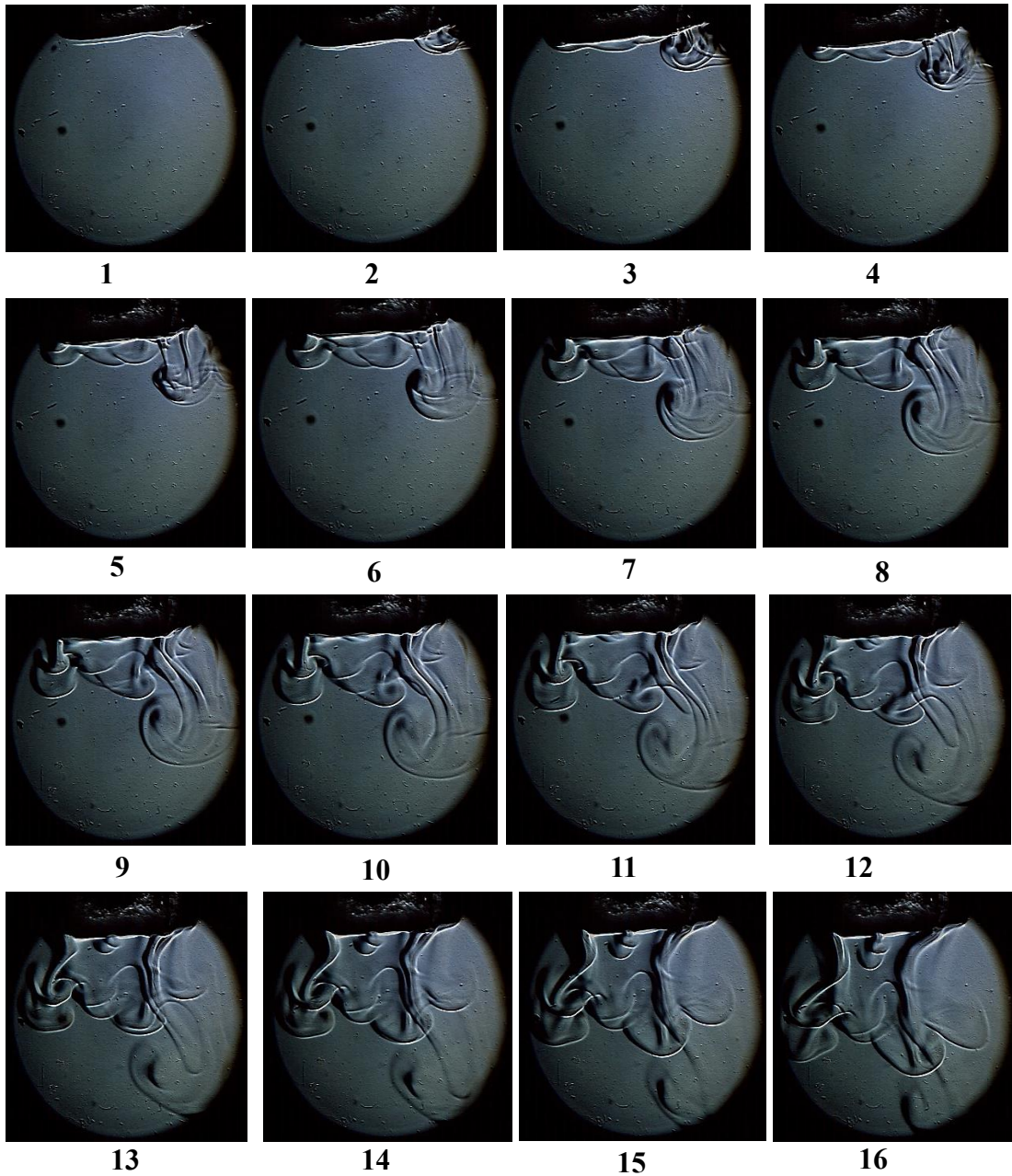Figure 6.2: Kelvin-Helmholtz instability as observed in the Negatively Buoyant Plumes in water

Figure 6.3: Time-lapse of development of Negatively Buoyant Plume of dense cold-water from ice cube cascading into lukewarm water

## 6.2 Under-expanded flow from a CD-nozzle

The under-expanded jet comprises of a series of expansion fans and oblique shock waves. These flow structures were visualized with the fabricated z-type schlieren setup and a single mirror schlieren setup. The single mirror schlieren was created from the existing z-type schlieren imaging system by removing one of its mirrors/ mirror mounts, and is presented in the appendix of this report. The mirror and optical equipment used in both setups were thus the same. This was done in order to compare the schlieren images and visually understand the sensitivity of images produced by z-type schlieren setup compared to the single-mirror schlieren setup. The CD-nozzle used for this study was designed for exit-Mach number of 1.4. The flow and system parameters considered during the design of the CD-nozzle are show in Table 6.1. The contour of the diverging section of the nozzle is generated following the Method of Characteristic (MOC) incorporated in a MATLAB code available in (Josh, 2023). With the generation of the contour of diverging section, a converging section is constructed and is connected to the diverging section with the throat of the nozzle in-between. The dimensions of the nozzle are shown in Table 6.2 and Figure 6.4. The CAD model of the nozzle is then constructed in a modeling software SolidWorks and finally a realistic prototype of the nozzle is printed in a 3D printer available in the Manufacturing Lab of The Department of Mechanical and Aerospace Engineering, Pulchowk Campus. The material used for 3D printing is Acrylonitrile Butadiene Styrene (ABS). It has high tensile strength and is resistant to physical impacts created by the supersonic flow. The 3D printed prototype of the CD-nozzle is shown in Figure 6.5. The nature of the flow through the CD-nozzle for NPR ranging from 5 to 7.5 as captured in z-type schlieren setup and single mirror schlieren setup are shown in Figure 6.6.

Table 6.1: Flow and system parameter values at different sections of the CD-nozzle

| Parameters | Inlet chamber | Throat | Exit |
|:---:|:---:|:---:|:---:|
| Pressure (Pascal) | 322443.73 (stagnation pressure) | 170341.15 (static pressure) | 101325.00 (static pressure) |

| | 300 | 250 | 215.517 |
|---|---|---|---|
| Temperature (Kelvin) | 300 | 250 | 215.517 |
| Density (kg/m$^3$) | 3.74 | 2.37 | 0.86 |
| Local velocity of sound (m/s) | $\approx 0$ | 316.938 | 294.269 |
| Velocity of flow | $\approx 0$ | 443.713 | 411.976 |

Table 6.2: Nozzle section dimensions

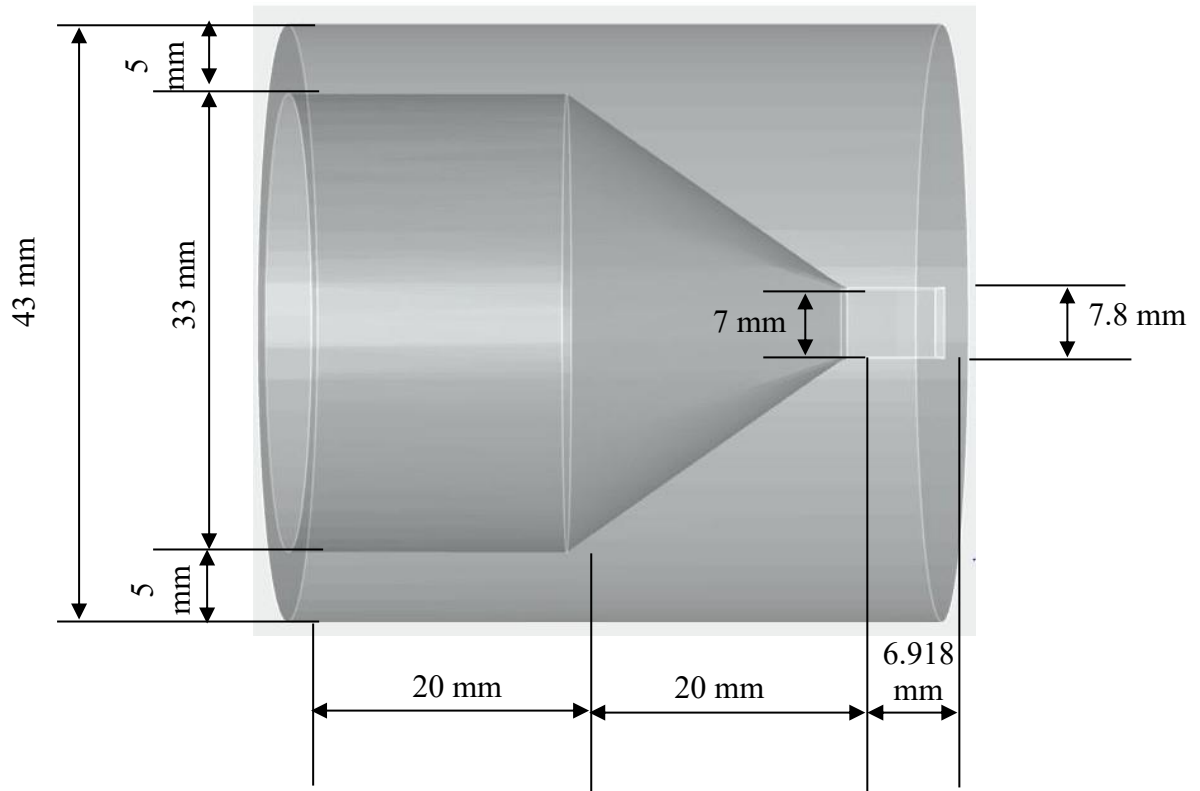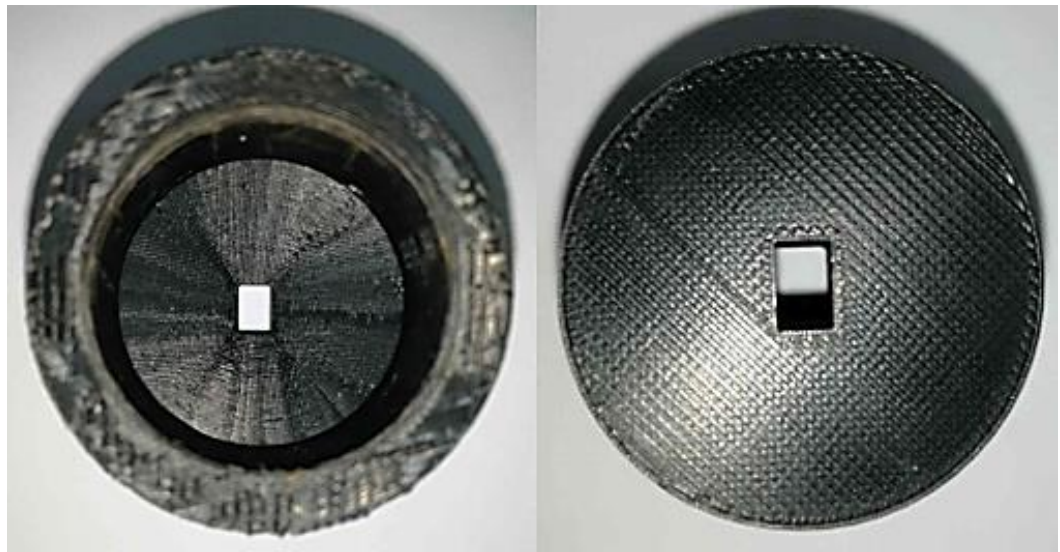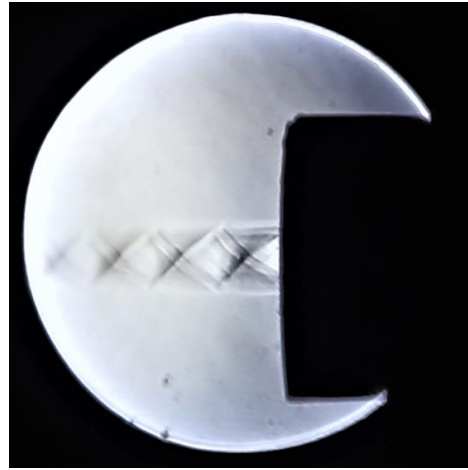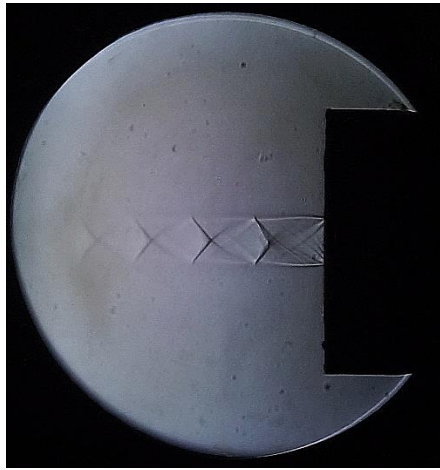| Nozzle sections | Dimension |
|---|---|
| Exit diameter | 7.8 mm |
| Throat diameter | 7 mm |
| Diverging section length | 6.918 mm |
| Converging section length | 20 mm |

Figure 6.4: Dimensions of the nozzle
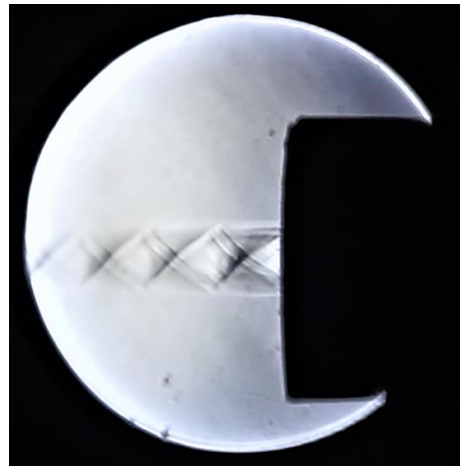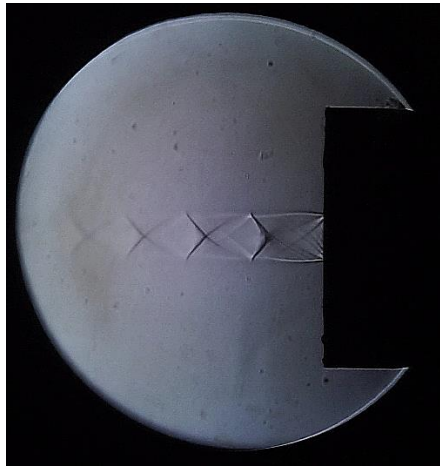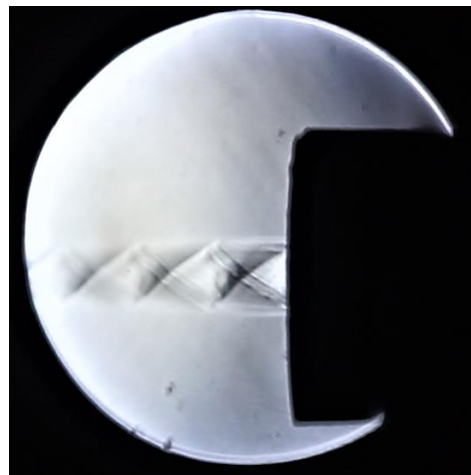


(a)                             (b)

Figure 6.5: (a) Converging section of the CD-nozzle, (b) Outlet section
of the CD-nozzle

(a)



(b)
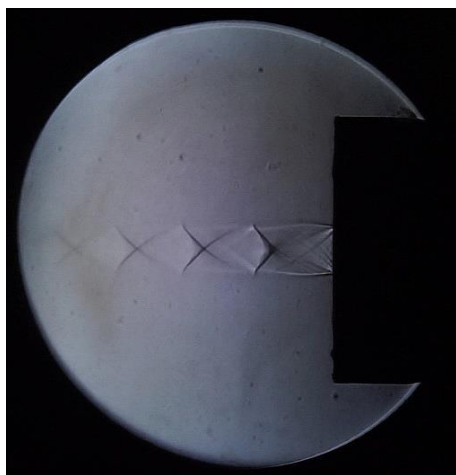


(c)
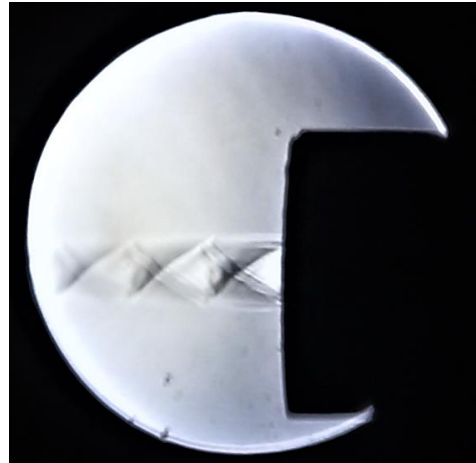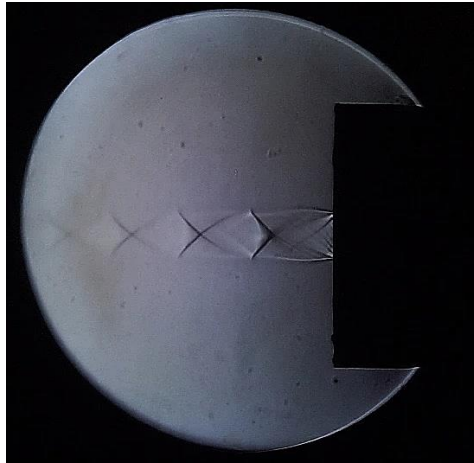
(d)
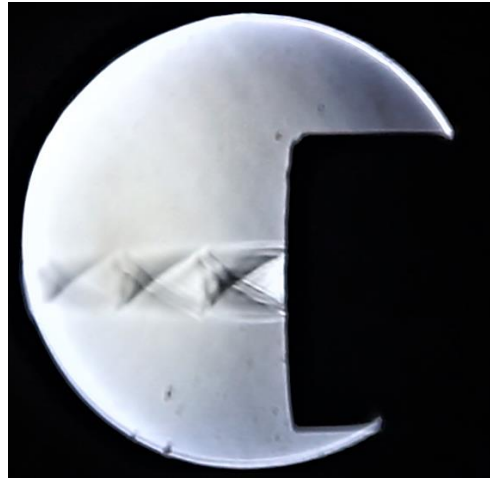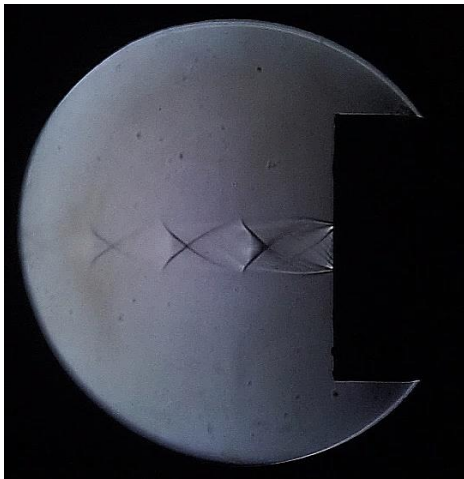


(e)

Figure 6.6: Under-expanded flow out of a CD-nozzle captured by the schlieren setup at NPR of (a) 5, (b) 5.5, (c) 6, (d) 6.5, and (e) 7 (Left: z-type schlieren images, Right: single mirror schlieren images)

It is evident that the schlieren images captured by z-type schlieren is better than the ones captured from single mirror schlieren. The intricate details of the flow including the oblique shock waves and regular shock-diamond patterns is better captured in the z-type schlieren setup. The single mirror schlieren setup in addition to its poor image quality is affected by the double-image phenomena which further degrades the quality of the schlieren image.

## 6.2.1 Regular shock-diamond location

The distance of the first shock-diamond from the nozzle exit plane is called the regular shock-diamond location. For this study, this parameter is considered as the key performance parameter in evaluating the accuracy of the images obtained from the z-type schlieren setup. The experimentally generated result is checked for accuracy against two well established empirical relations. During the study of the structure of a free-jet expansion in a partially evacuated vacuum, (Ashkenas & Sherman, 1966) found the empirical relation shown in Eq. 5.1, which relates regular shock-diamond location to the nozzle and system parameters.

$$\frac{x_M}{d^*} = 0.67 \times \sqrt{\frac{p_r}{p_b}} \qquad\qquad \text{Eq. 5.1}$$

where,

$x_M$: Shock-diamond location measured from nozzle-exit plane

$d^*$: effective sonic nozzle diameter

$p_r$: the compressor chamber pressure

$p_b$: background pressure (back pressure)

In the study performed by (Young, 1975), using entropy balance principle the author was able to obtain another empirical relation for Shock-diamond location given by,

$$\frac{x_M}{d^*} = C(\gamma) \times \sqrt{\frac{p_r}{p_b}} \qquad\qquad \text{Eq. 5.2}$$

where,

$$C(\gamma) \quad = 0.76 \text{ for } \gamma = \frac{5}{3}$$

$$= 0.72 \text{ for } \gamma = \frac{7}{5}$$

$$= 0.69 \text{ for } \gamma = \frac{9}{7}$$

The regular shock-diamond location as observed in the schlieren images for different NPR is compared with the forementioned empirical relations. The distance for regular shock-diamond location from schlieren images was obtained through image processing software called ImageJ. The comparison of the experimental result with the empirical relations are shown in Table 6.3 and 6.4. The calibration and calculation process in ImageJ software are shown in Figures 6.7, 6.8, 6.9, 6.10, and 6.11 respectively.

Table 6.3: Comparison of regular shock-diamond location from the nozzle exit plane

| Compressor Pressure $(p_r)$ atm | Background Pressure $(p_b)$ atm | Effective sonic nozzle diameter $(d^*)$ cm | Ashkenas & Sherman, 1966 $(x_M)$ cm | Young, 1975 $(x_M)$ cm | Schlieren flow visualization $(x_M)$ cm |
|---|---|---|---|---|---|
| 5 | 1 | 0.78 | 1.168 | 1.256 | 1.105 |
| 5.5 | 1 | 0.78 | 1.226 | 1.317 | 1.167 |
| 6 | 1 | 0.78 | 1.280 | 1.376 | 1.267 |
| 6.5 | 1 | 0.78 | 1.332 | 1.432 | 1.343 |
| 7 | 1 | 0.78 | 1.383 | 1.486 | 1.423 |

Table 6.4: Relative difference of the experimental result with the empirical relations

| NPR | Relative difference with Ashkenas & Sherman, 1966 (%) | Relative difference with Young, 1975 (%) |
|---|---|---|
| 5 | 5.394 | 12.022 |
| 5.5 | 4.812 | 11.389 |
| 6 | 1.015 | 7.921 |
| 6.5 | 0.826 | 6.215 |
| 7 | 2.892 | 4.239 |
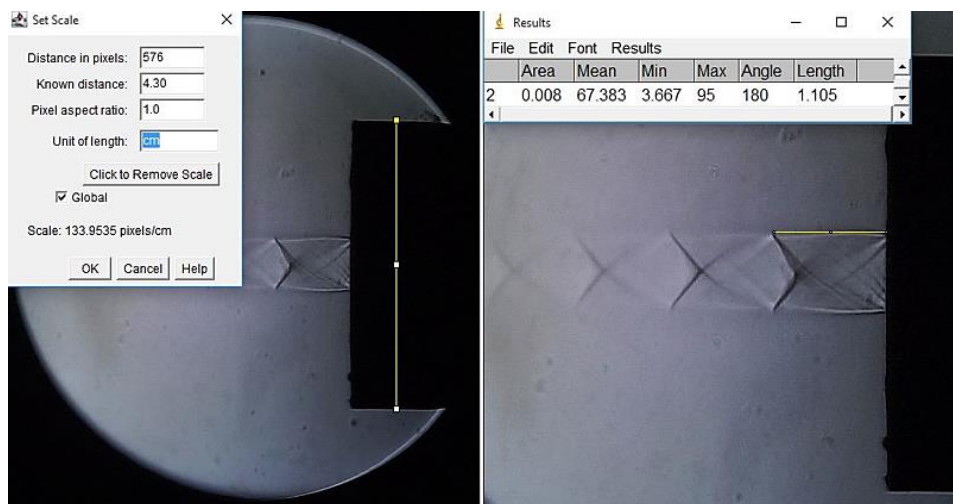


(a)           (b)

Figure 6.7: Regular shock-diamond location for NPR 5, (a) Calibration, (b) Measurement of distance
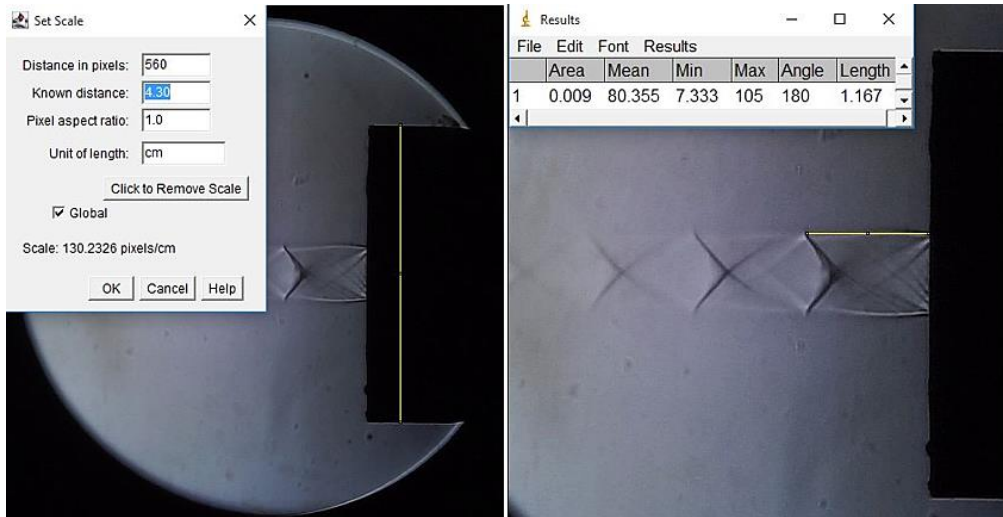
(a)                                                      (b)

Figure 6.8: Regular shock-diamond location for NPR 5.5, (a) Calibration, (b)
Measurement of distance



(a)                                                      (b)

Figure 6.9: Regular shock-diamond location for NPR 6, (a) Calibration, (b)
Measurement of distance

(a)                                                            (b)

Figure 6.10: Regular shock-diamond location for NPR 6.5, (a) Calibration, (b)
Measurement of distance



(a)                                                            (b)

Figure 6.11: Regular shock-diamond location for NPR 7, (a) Calibration, (b)
Measurement of distance

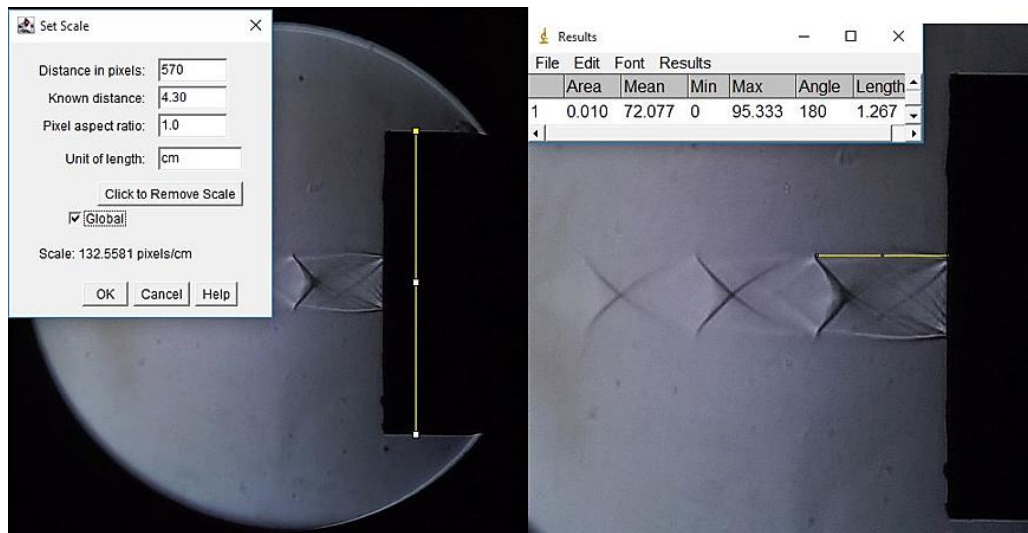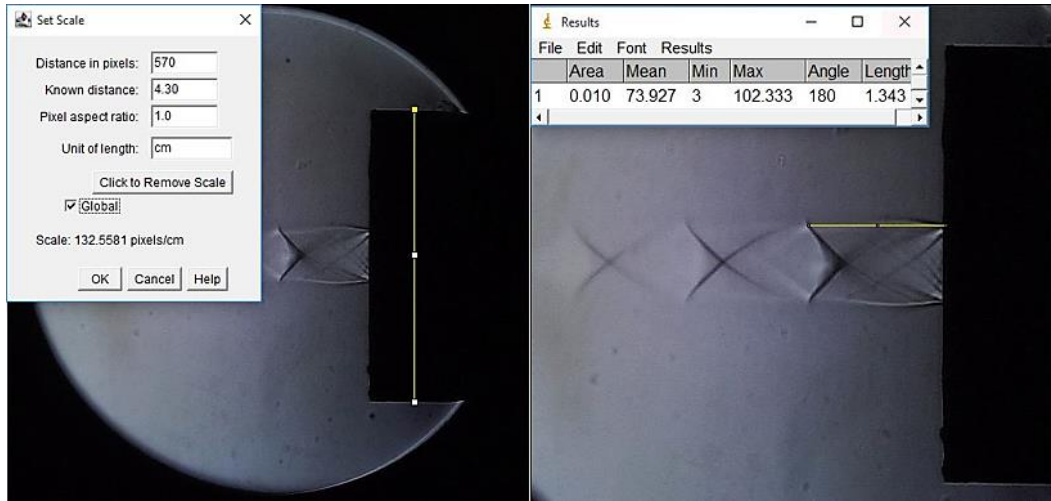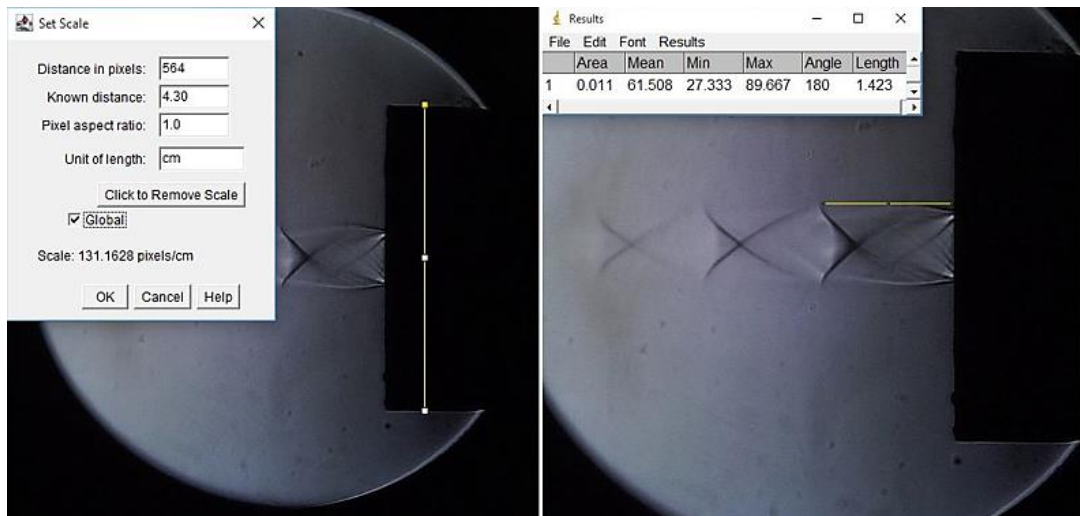The variation in results for the regular shock-diamond location as obtained from z-type schlieren setup with the empirical relations provided by (Ashkenas & Sherman, 1966) and (Young, 1975) as shown in Table 6.4 could be because of the inaccuracy during the measurement process while using ImageJ software, inaccuracy in the 3D-printed model of the nozzle like surface roughness, and inaccuracy present within the z-type schlieren setup itself. Despite all of these constraints, the comparison of the data generated for schlieren images with the empirical relations show that there are no significant variations (relative difference is confined within the range of 0.826 % to 12.022 %) in the regular shock-diamond location and the schlieren imaging is good enough to capture the shock patterns generated in the under-expanded flow from the CD-nozzle.

## 6.2.2 Mach-Number along the jet centerline

The schlieren images of the under-expanded jet emerging out of the exit plane of the nozzle captured from the z-type schlieren setup is used to plot the distribution of Mach-number along the jet centerline. The plot for each NPR was done on the basis of pixel intensity (pixel value) along the jet centerline for the corresponding schlieren images. The example of such pixel intensity variation along the jet centerline for NPR 7 is shown in Figure 6.12 and Figure 6.13. The plot was generated with the help of image processing software ImageJ.
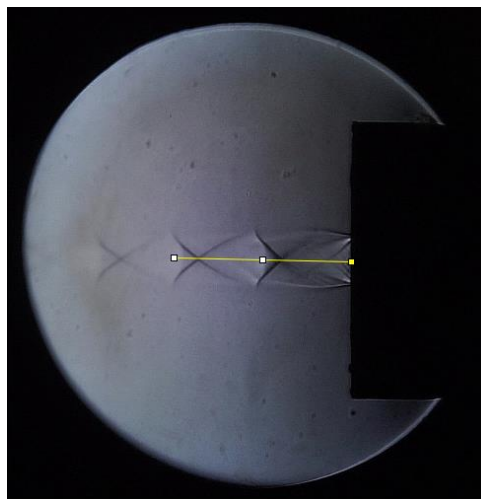


Figure 6.12: Setting up the region whose pixel plot is to be analyzed (the region is represented by the yellow line)
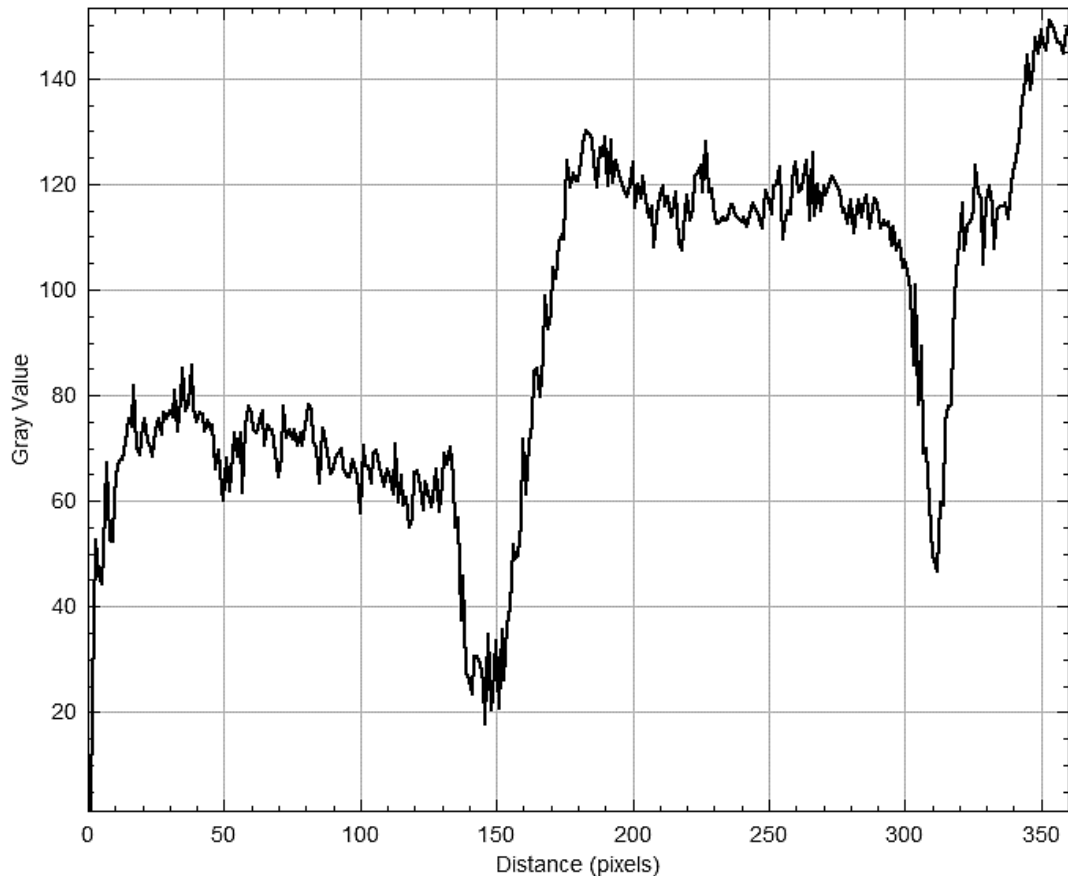
Figure 6.13: Pixel intensity (Gray value) variation along the axial distance of the jet centerline for NPR 7

It is observed from Figure 6.13 that the plot of gray values with the axial distance along the jet follow a rough sinusoidal pattern. Higher gray value corresponds to the expansion region where the flow is supersonic, and the lower gray values corresponds to the dark region representing the subsonic flow (Faheen, et al., 2021). In order to obtain the plot of Mach number along the jet centerline from the gray values, there needs to be a provision of calibrating the gray values to their corresponding Mach numbers. In this study, linear interpolation technique has been used for such calibration, where the minimum and maximum gray scale values were linked to the minimum and maximum values of Mach number that could occur in the flow and the subsequent gray values were linked to the Mach number given by the linear interpolation relation. It is to be noted that studies like the one done here has high probability of facing errors because the results greatly depend on the lower and higher values of Mach number that occurs in the flow-region. Both of those values are assumed in this study. The lower Mach number is assumed to be 1.4 at the exit plane of the CD-nozzle, and the maximum

Mach number is taken from the basis of simulation study. The results obtained from the pixel intensity (gray value) after calibration were compared with their corresponding simulation results. This gave an insight on whether the trend that the Mach number follows in the experimentally generated schlieren images and the ones generated from the simulation study are in good agreement or not. The comparison of the plots was done up until second shock-diamond location to present uniformity in all the studies. The comparison results are shown in Figure 6.14.



(a)

Mach Number along the jet centerline (NPR 5.5)

(b)



Mach Number along the jet centerline (NPR 6)
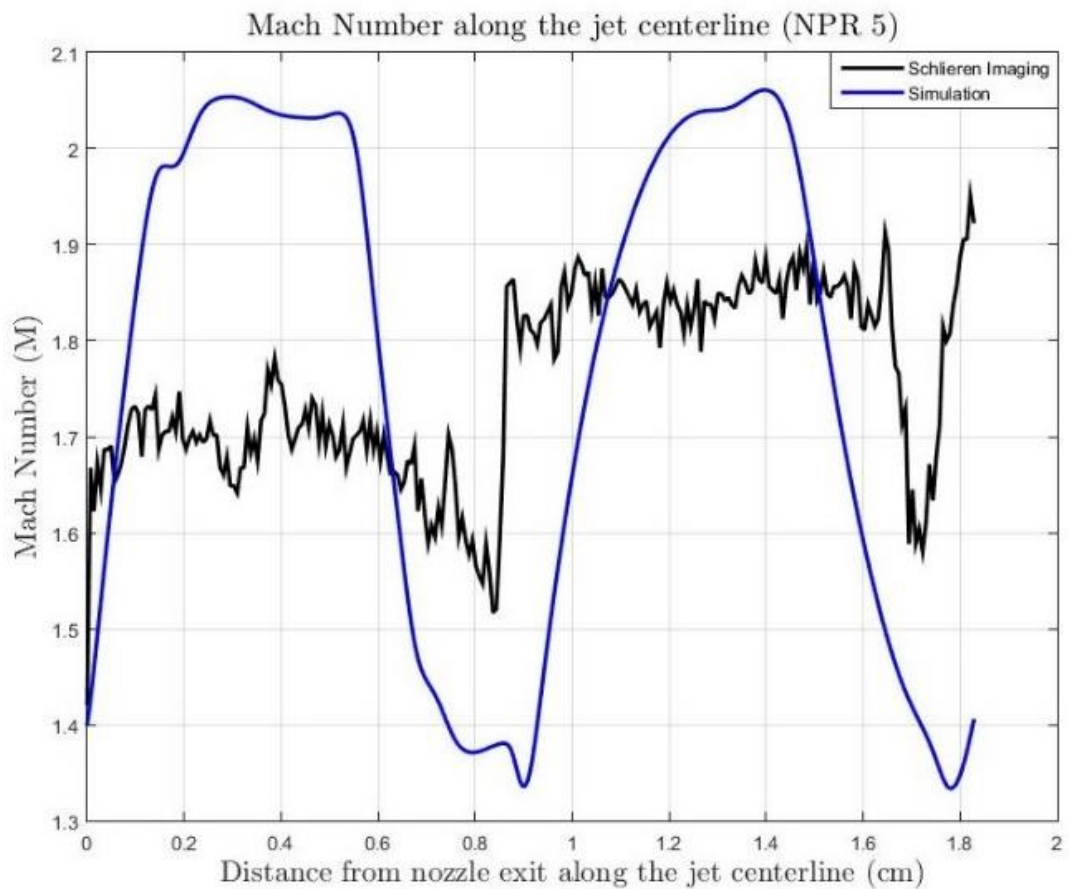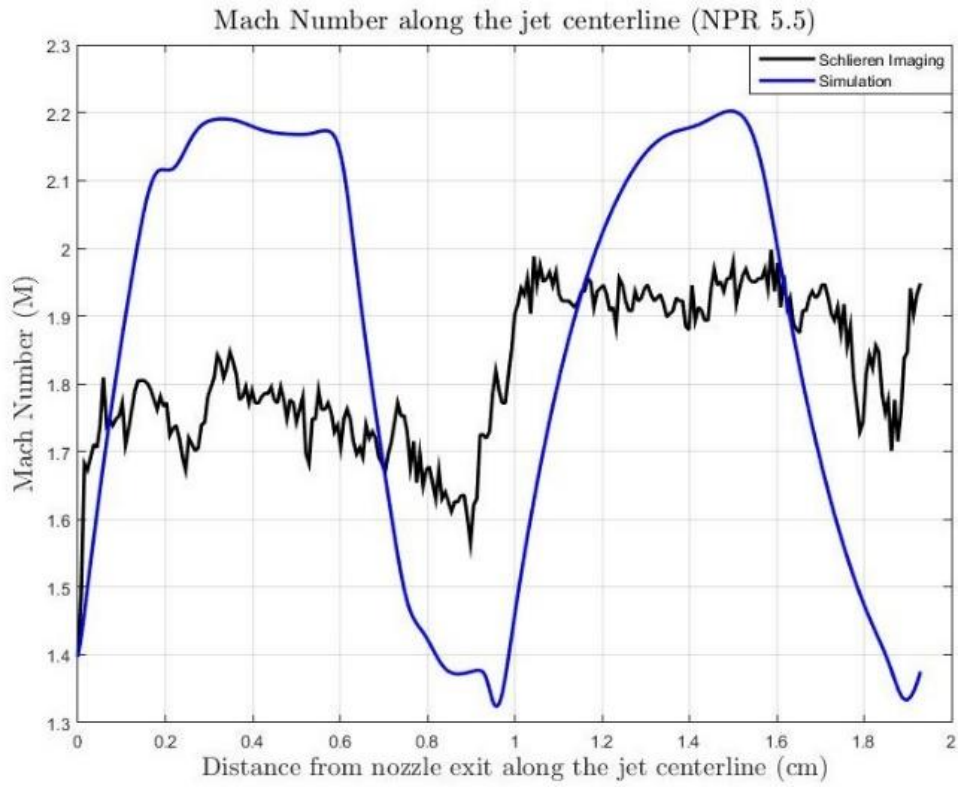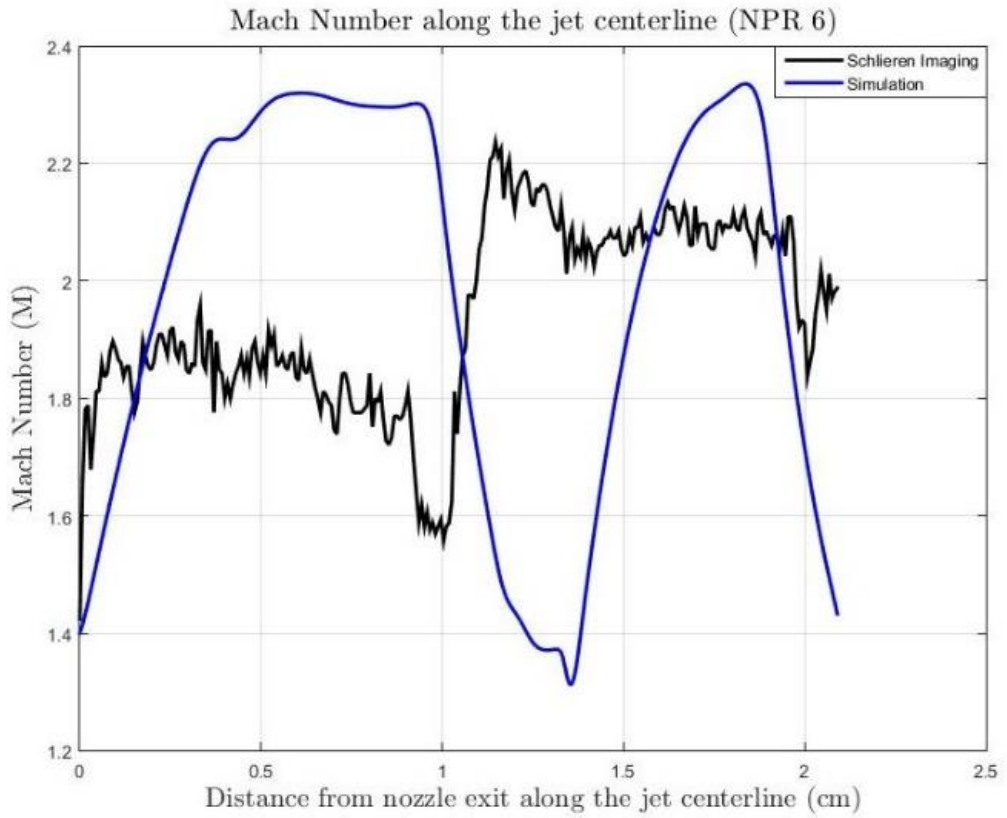
(c)

(d)



(e)

Figure 6.14: Comparison of Mach number along the jet centerline for NPR (a) 5, (b) 5.5, (c) 6, (d) 6.5, and (e) 7

The comparison plots show that there is no one-to-one match between the experimentally generated data and simulation generated data. However, in all of the comparison plots, the trend of the curves does match to some extent. The sinusoidal nature of variation in Mach number along the jet centerline is evident in both simulation and experiment. As mentioned before, this stud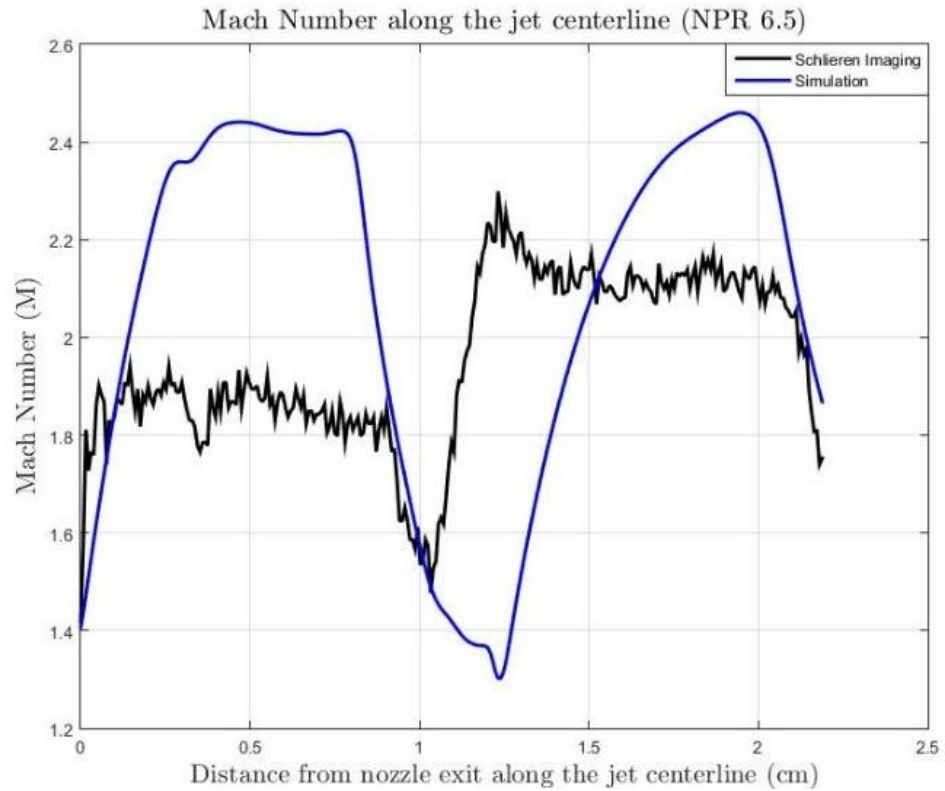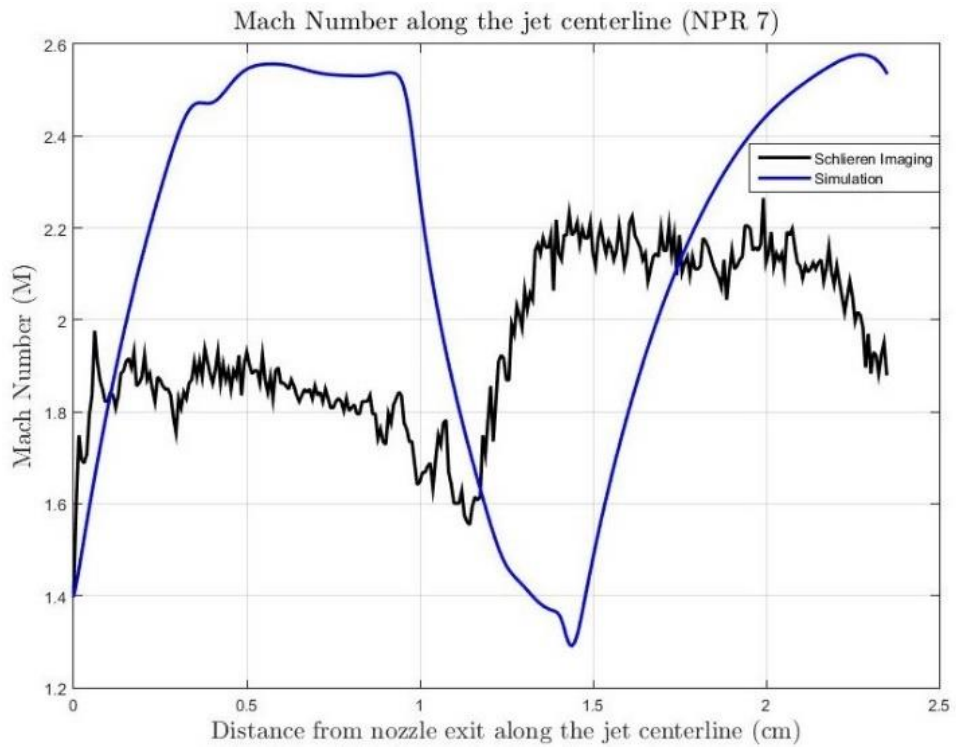y is proceeded with an assumption of linear variation of Mach number and gray values of the schlieren images. Thus, any non-linearities that may be present is not accounted for in this study. Use of a more rigorous image processing analysis, development of non-dimensional parameter along the jet centerline to reconcile the variations in shock-diamond distance in schlieren images and numerical results, and better correlations in the upper and lower limit of Mach number for the under-expanded jet in the captured schlieren images could yield a better comparison plot.

## 6.3 Fluidic-Thrust Vectoring

The controlled deviations in the exit plume from a high-speed aircraft for its better maneuverability falls under the domain of thrust, propulsion, vector control of supersonic jets. This technique has been widely used in the jet and rocket engines, ejectors, and many other devices. Fluidic thrust vector, is one such method of achieving such deflection/ deviation in the flow. The study focuses on a simple technique to achieve flow defections by creating small outlet sections at the diverging section of the nozzle. The nozzle used for this study is the CD-nozzle designed for the study of under-expanded jet having exit Mach number of 1.4. The CAD design of the nozzle with outlet section is shown in Figure 6.15. The study was performed for NPR of 7 and for outlet section having diameter of 3 mm and 5 mm respectively. The deviations created in the flow were visualized with the z-type schlieren setup, and the angle of deviation was found through the image processing software ImageJ. The results are shown in Figure 6.16.
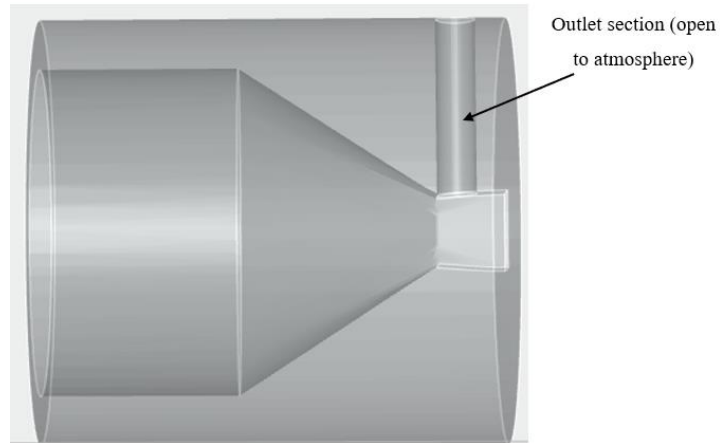
Figure 6.15: CAD model of the CD-nozzle with a small outlet section created in the diverging region
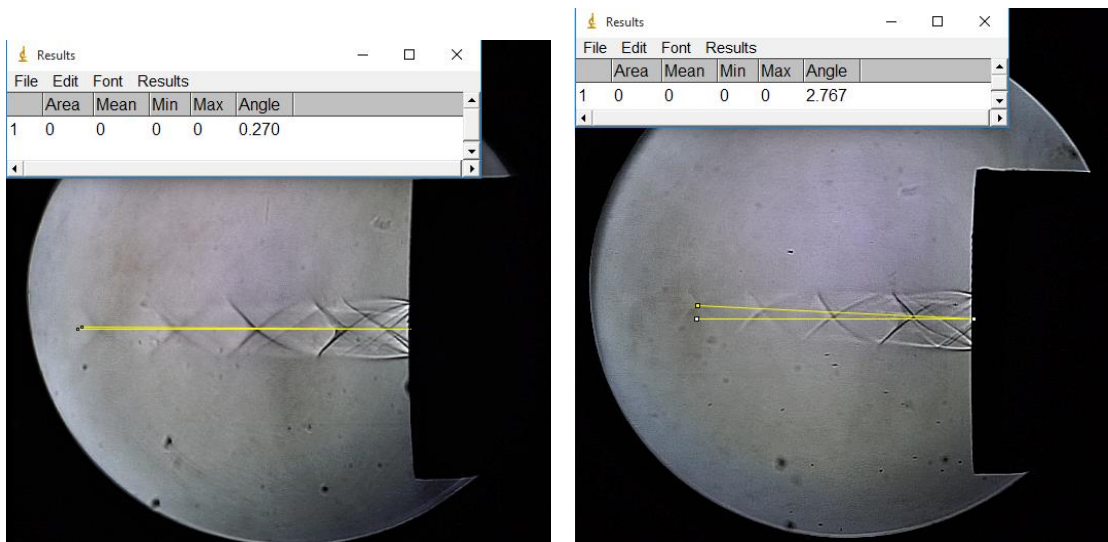


Figure 6.16: Deviation in the flow (a) 3mm outlet section, (b) 5mm outlet section

It is observed that the deviation in flow has increased with the increase in diameter of the outlet section. The study is only experimental and lacks the theoretical interpretation of the flow-deviation phenomena, and only attempts to address the capability of the fabricated z-type schlieren setup to capture the deviations in the flow which could then be analyzed in the image processing software.

# CHAPTER SEVEN: CONCLUSION AND RECOMMENDATIONS

## 7.1 Conclusion

The fabricated z-type schlieren imaging system have the capacity to capture the density-gradients caused by the schlieren object in the test section. This system has been proven to be sensitive enough for qualitative analysis of simple subsonic phenomena such as thermal plume from a human hand and burning candle, hot air rising from the top of a soldering iron, Negatively-Buoyant Plume in water as well as flow patterns of Under-Expanded jet from a CD nozzle. The sensitivity of the z-type schlieren setup was evaluated qualitatively by comparing the images of under expanded-jet for NPR 5 to 7 (in intervals of .5) with the corresponding images from single mirror schlieren. In its qualitative evaluation, the schlieren images from z-type setup were better in terms of picture quality and clarity, and were also free from the issues of double-image formation. Quantitative sensitivity analysis of the schlieren setup is still a work left to be done as it requires data on luminous intensity of the point light source, exact dimension of the point light source, etc. which was not under the scope of this research work. In accordance to the objective of performing experimental study on different fluid-flow phenomena, the fabricated z-type schlieren fulfills it with the study of Negatively-Buoyant Plumes where it was able to capture intricate flow structures during the flow's development, namely the Rayleigh-Taylor Instability and the Kelvin-Helmholtz Instability. Similarly, in the study of the Under-Expanded Jet from a CD-nozzle, the resulting schlieren images showed the regular shock-diamond patterns along with oblique shock waves and expansion waves with clarity. In addition to the qualitative study, the schlieren images of under-expanded jet served for the quantitative study of regular shock-diamond location and also for the plot of Mach-number along the jet-centerline. These quantitative results were not satisfactory but it does provide us with a glimpse on how powerful the schlieren setup could be. With mere utilization of the post-processing tools for image captured with the schlieren technique, the Mach number distribution along the jet centerline was able to be plotted. Additional work could yield a better result for Mach number distribution, as well as the study on myriad of different parameters like density, pressure, etc. along the jet centerline. The setup is present in the IIEC, Pulchowk Campus in fully functional form and could be used for

the study of different fluid-flow phenomena involving density-gradients by the undergraduate students.

## 7.2 Recommendations

Along with the conclusion, there are few recommendations that are drawn based on the available literature on the schlieren imaging system and the experience gained by the author while working with the z-type schlieren setup in performing the experimental test included in this research study. Some of the recommendations are mentioned below:

### 7.2.1 Z-type Schlieren Imaging Setup

- It is a good practice to use parabolic mirrors with $f$-number of 6 or greater and with a larger diameter of $\geq 15$ cm to have a greater field-of-view to study a wide range of fluid-flow phenomena.
- A better LED light module with variable width slit to adjust the amount of output light and user-specified LED wavelength output would allow for quantitative sensitivity analysis of the schlieren images.
- A better cut-off/ slit designed for the purpose of schlieren imaging would cancel off the diffraction effect leading to improvement in sensitivity of schlieren images.

### 7.2.2 Study of Negatively-Buoyant Plumes

- It would be better to use color-schlieren technique as it would give an insight on density variation as the plume of cold-water cascades down the lukewarm water.

### 7.2.3 Study of Under-expanded Jet

- The current study used a planar CD-nozzle for the study of under-expanded jets. Similar study with the use of an axisymmetric nozzle for same nozzle parameters and their comparison could be performed.
- Using high-pressure air compressor and a bigger reservoir to hold a greater quantity of compressed air would help in maintaining the under-expanded flow for a longer period of time.

- A resin printed CD-nozzle would have a better surface finishing compared to ABS printed leading to reduction in turbulent losses of the flow.
- Study of the under-expanded jet for a wider range of exit Mach numbers using color schlieren technique would provide a better insight on density variations within the flow structure.

# REFERENCES

1) ANL, K. P., Sundararaj, A. J., & Khan, M. A. (2022). Investigation of nozzle flow in high altitude test facility. *Sage Journals*.

2) ANSYS. (2008). *Reporting Mesh Statistics.* ANSYS Inc.

3) ANSYS. (2010). *ANSYS FLUENT User's Guide.* Canonsburg, PA, USA: ANSYS Inc.

4) Ashkenas, H., & Sherman, F. (1966). *Rarefied Gas Dynamics.* New York: Academic.

5) Chandrasekhar, S. (1961). *Hydrodynamic and Hydromagnetic Stability.* London: Oxford University Press.

6) *Chronos 2.1-HD Starter Bundle*. (2023, November 21). Retrieved from Kron Technologies: https://www.krontech.ca/product/chronos-2-1-hd-starter-bundle/

7) Dyke, M. V. (1982). *An album of fluid motion.* Stanford: Parabolic Press.

8) Faheen, M., Khan, A., Kumar, R., Khan, S. A., Asrar, W., & Sapardi, M. A. (2021). *Estimation of Mach numbers in supersonic jets using schlieren images.* Elsevier.

9) Gautam, B., Budhathoki, K., & Sitoula, M. (2023). *Supersonic nozzle test using high pressure compressor.* Lalitpur: Institute of Engineering, Pulchowk Campus, Tribhuvan University.

10) Josh. (2023, August 15). *GitHub*. Retrieved from Rocket nozzle design : https://github.com/jte0419/Rocket_Nozzle_Design

11) Kaessinger, J., & Kors, K. (2014). Utilizing Schlieren Imaging to Visualize Heat Transfer Studies. *ASME 2014 International Mechanical Engineering Congress and Exposition, IMECE2014.* Montreal, Quebec, Canada.

12) Kamalasekaran, A. (2020). *Numerical and experimental investigations of gas jet used in atomisation of metal powders.* Stockholm, Sweden: KTH Royal Institute of Technology.

13) Mach, E., & Salcher, P. (1887). Photographische Fixierung der durch Projektile in der Luft eingeleiteten Vorgänge sitzungsbe. *Sitzungsb Akad Wiss Wien*, 764-780.

14) Merzkirch, W. (2011, February 11). *Thermopedia* . Retrieved from Visualization of flow : https://www.thermopedia.com/content/1245/

15) Mitchell, D., Honnery, D., & Soria, J. (2007). Study of Underexpanded Supersonic Jets with Optical Techniques. *16th Australian Fluid Mechanics Conference* (pp. 217-224). Crown Plaza, Gold Coast, Australia: Laboratory for Turbulence Research in Aerospace and Combustion.

16) Nordberg, J. K. (2015). *An Assessment of Colour Schlieren Photography for Supersonic Flows.* Norrbotten County, Sweden: Luleå University of Technology.

17) Norman, M. L., & Winkler, K.-H. A. (1985). Supersonic Jets. *Los Alamos Science*, 38-71.

18) Pelt, H. v., Neely, A., & Young, J. (2015). Analytical Models for Side Force Prediction of Fluidic Thrust Vectoring on High-Speed Vehicles. *22nd International Symposium on Air Breathing Engines.* Ottwa, Ontario, Canada: School of Engineering and Information Technology, University of New South Wales.

19) Ranabhat, S. (2022). *Numerical and Experimental Investigation of Exhaust Flow from Convergent-Divergent Nozzle.* Kathmandu: Institute of Engineering, Thapathali Campus.

20) Robinson, C. (2016). *Flow Through a de Laval nozzle.* Boston University.

21) Sack, J., & Urrutia, J. (2000). *Handbook of Computational Geometry.* Elsevier.

22) Schardin, H. (1934). Das Toeplersche Schlierenverfahren: Grundlagen für seine Anwendung und quantitative Auswertung. *VDI-Forschungsheft*, 1-32.

23) Schardin, H. (1970). *Schlieren Methods And Their Applications.* Washington: National Aeronautics and Space Administration (NASA).

24) Schmidt, B. (2015). *Schlieren Visualization.* California: Caltech .

25) Settles. (2001). *Schlieren and Shadowgraph Techniques: Visualizing Phenomena in Transparent Media.* Berlin: Springer.

26) Settles, G. S., & Hargather, M. J. (2017). *A review of recent developments in schlieren and shadowgraph techniques.* Bristol: IOP Publishing Limited.

27) Shafer, H. (1949). Physical optic analysis of image quality in schlieren photography. *Journal of the SMPE*, 524-544.

28) Shakouchi, T., & Fukushima, S. (2022). Fluidic Thrust, Propulsion, Vector Control of Supersonic Jets by Flow Entrainment and the Coanda Effect. *energies*.

29) Speak, G., & Walters, D. (1950). *Optical considerations and limitations of the schlieren method.* London: British Aero. Research Council.

30) Strutevant, B. (1990). *Rayleigh-Taylor Instability in Compressible Fluids.* Pasadena, CA: Graduate Aeronautical Laboratories, California Institute of Technology.

31) Tkaczyk, T. (2010). *Field Guide to Microscopy.* Bellingham, Washington: SPIE Press.

32) Travers, N. (2012). *Schlieren Z-Type Flow Visualization System-Visualization of Negatively Buoyant Plumes in Water.* Boulder: University of Colorado.

33) Tropea, C., Yarin, A. L., & Foss, J. F. (2007). *Springer Handbook of Experimental Fluid Mechanics.* Berlin Heidelberg: Springer.

34) *Water Density Table.* (2022, October 06). Retrieved from Internetchemistry: https://www.internetchemistry.com/chemical-data/water-density-table.php

35) Weinberg, F. (1963). *Optics in flames: including methods for the study of refractive index fields in combustion and aerodynamics.* London: Buttersworth.

36) Young, W. S. (1975). Derivation of the free-jet Mach-disk location using the entropy-balance princple. *Physics of Fluids*, 1421-1425.
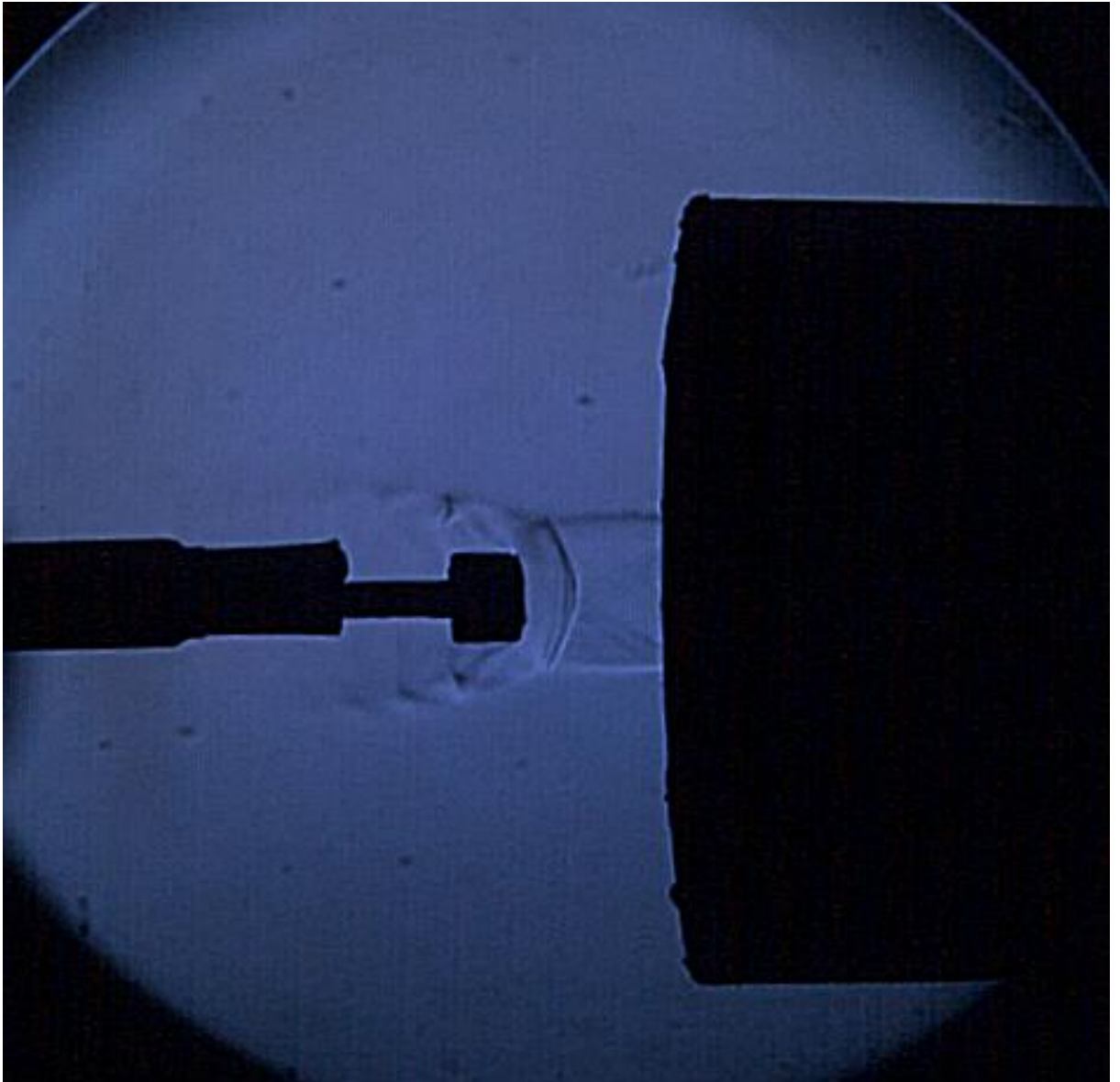
# APPENDIX

Further flow phenomena captured through the z-type schlieren setup:



Bow-shock formation in front of the nose of an aircraft model (captured by Sony ZV-E10 Mirrorless Camera)
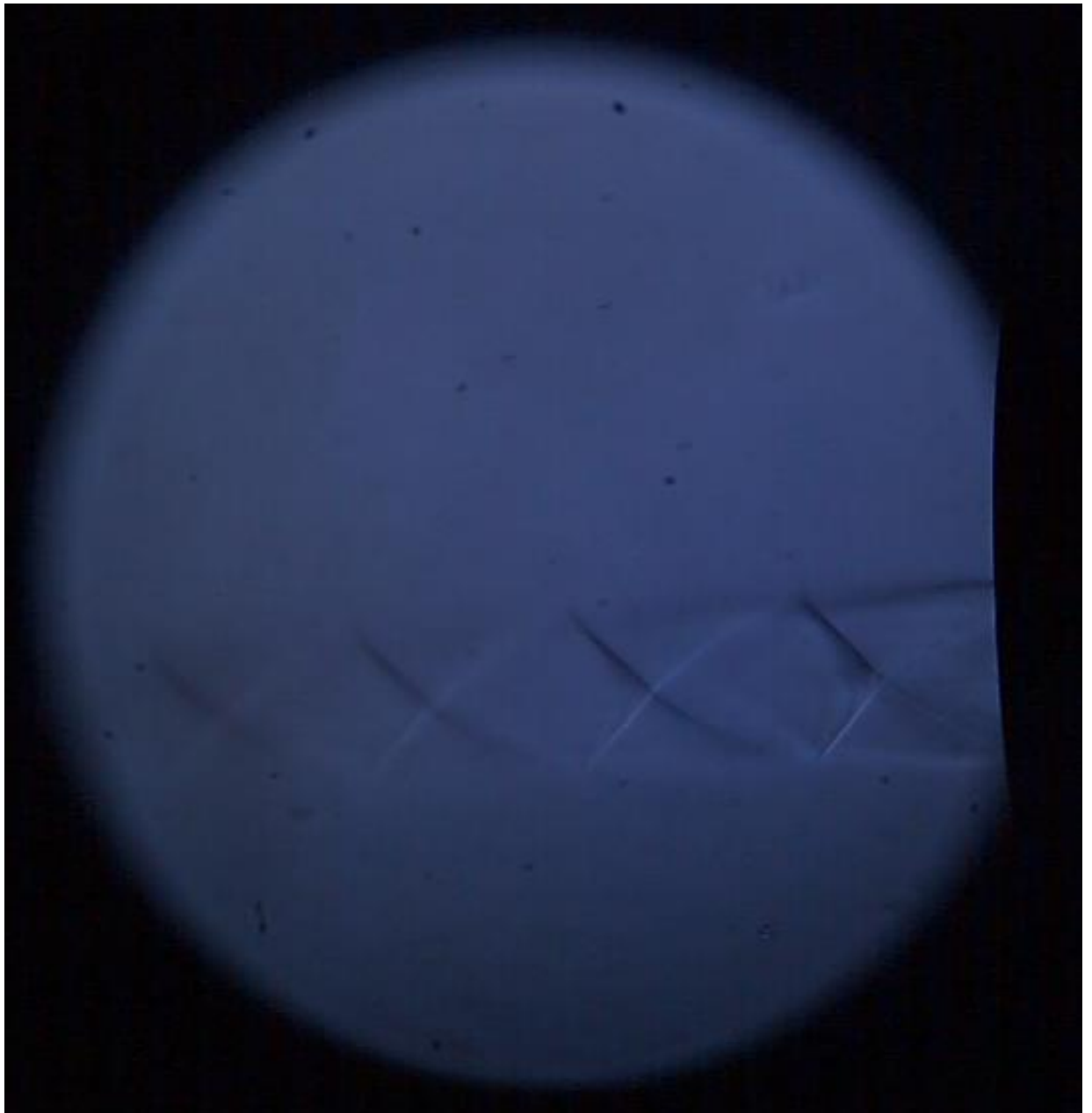
Bow-shock formation in front of the L-shaped blunt body (captured by Chronos
High Speed Camera, 1000 fps, 1920×1820-pixel intensity)

Bow-shock formation in front of the cube shaped blunt body (captured by
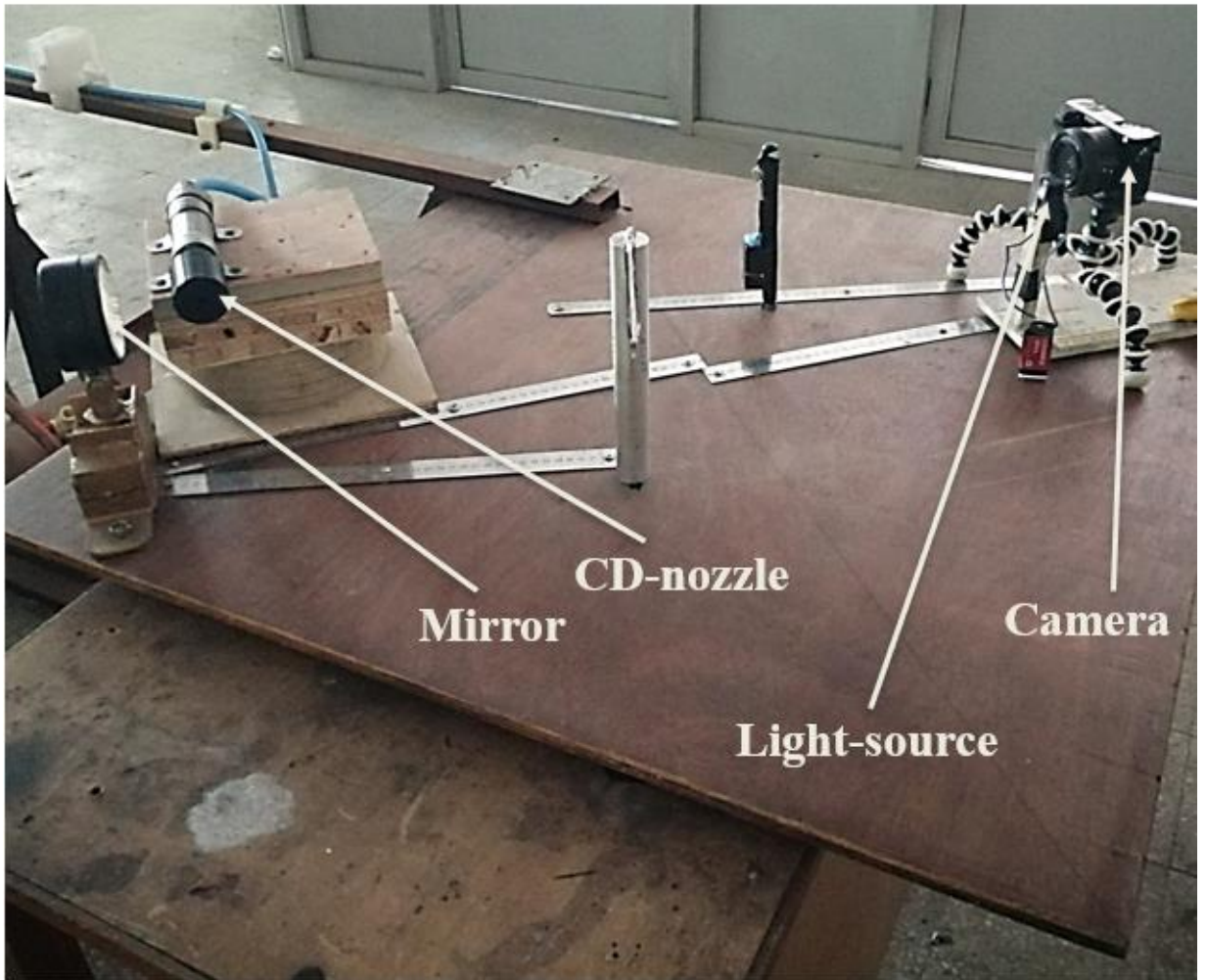Chronos High Speed Camera, 1000 fps, 1920×1080-pixel resolution)

Under-expanded jet from the CD-nozzle designed for exit Mach-number of 1.4
(captured by Chronos High Speed Camera, 1000 fps, 1920×1080-pixel resolution)

Time-lapse of a burning matchstick (captured by Chronos High Speed Camera, 1000 fps, 1920×1080-pixel resolution)
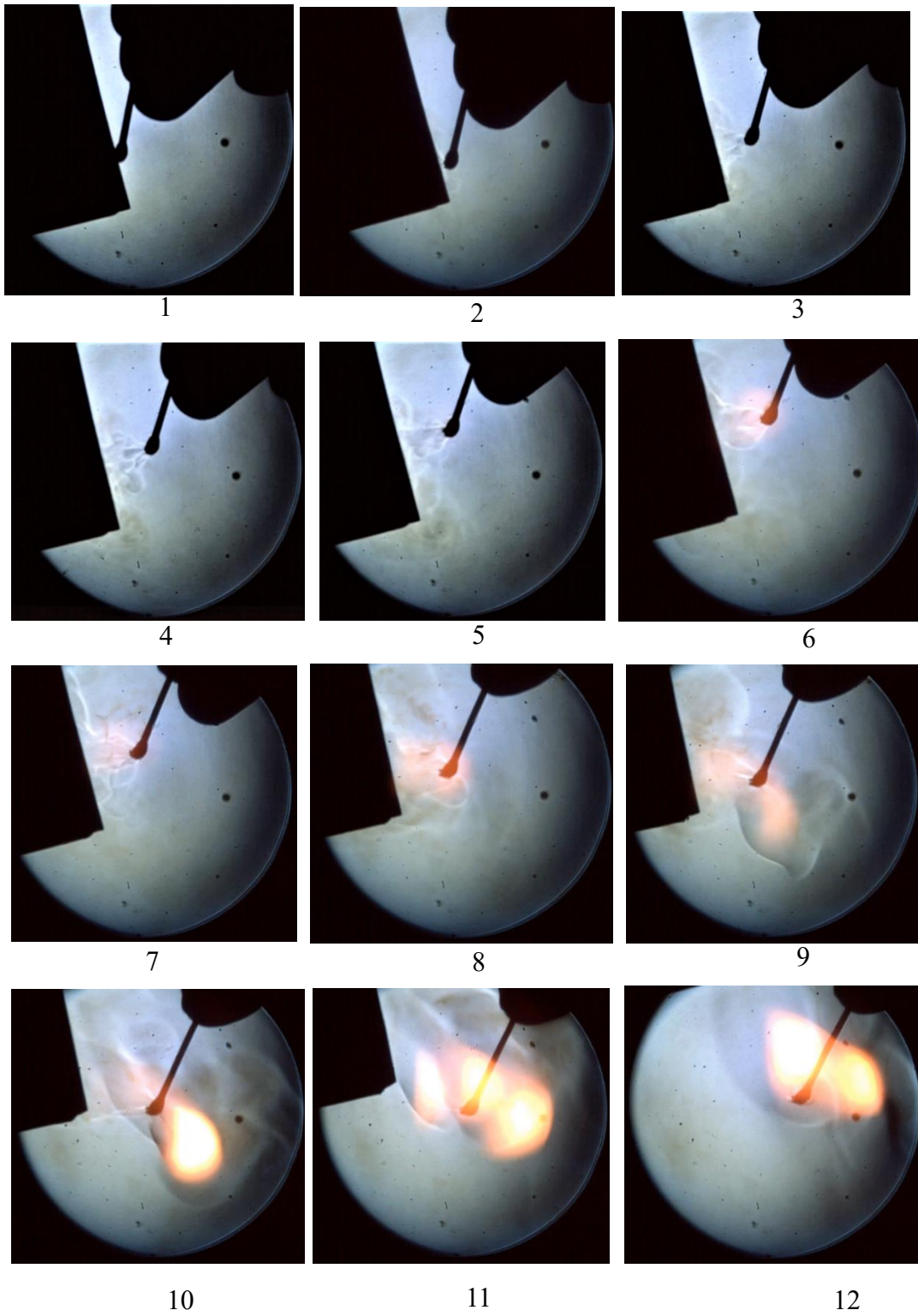
Single mirror schlieren system constructed out of the z-type schlieren system

**MATLAB Code (Pixel intensity plot)**

```matlab
clear;
clc;
close all;

%% Image read
RGB=imread('Place your image name');
imshow(RGB)
I = rgb2gray( RGB ); % conversion to gray-scale image
imshow(I)
impixelinfo() % to get pixel information from the figure
d_I=double(I); % converting image I into double format
imshow(d_I)
impixelinfo() % to get pixel information from the figure

%% Interpolation Procedure
d_I_update=zeros(size(d_I,1),size(d_I,2)); % pre-allocation
for ii=1:size(d_I,1)
    for jj=1:size(d_I,2)
        d_I_update(ii,jj)=1.40+(59/8800).*d_I(ii,jj); % depends on
the
    end      minimum and maximum Mach number for each flow condition
end          (example for NPR 7)

%% Plots
centerline=d_I_update(78,:); % pixel information for the flow
centerline (centerline lies on 78th row for the image)
distance=linspace(0,2.348,311); %distance along the flow centerline
plot(distance,centerline,'k','linewidth',2)
grid on
hold on
A=importdata('import the data from ANSYS in .txt format');
Mach_Number=A(:,2); % Mach Number obtained from simulation
distance_sim=linspace(0,2.348,744);
plot(distance_sim, Mach_Number,'b','linewidth',2)
grid on
legend('Schlieren Imaging', 'Simulation')
ylabel('Mach Number (M)','interpreter','latex','FontSize',15)
xlabel('Distance from nozzle exit along the jet centerline
(cm)','interpreter','latex','FontSize',15)
title('Mach Number along the jet centerline (NPR
…)','interpreter','latex','FontSize',16)
```

# Z-type Schlieren